



**LIBRA-LiTE: A Commercial Light Ion Fusion
Power Plant, Final Report for Calendar Year 1991**

**B. Badger, B. Choi, R.L. Engelstad, G.L. Kulcinski, E.G.
Lovell, J.J. MacFarlane, E.A. Mogahed, G.A. Moses,
R.R. Peterson, S. Rutledge, M.E. Sawan, G.
Sviatoslavsky, I.N. Sviatoslavsky, L.J. Wittenberg**

December 1991

UWFDM-880

***FUSION TECHNOLOGY INSTITUTE
UNIVERSITY OF WISCONSIN
MADISON WISCONSIN***

**LIBRA-LiTE: A Commercial Light
Ion Fusion Power Plant**

Final Report for Calendar Year 1991

B. Badger, B. Choi, R. L. Engelstad, G. L. Kulcinski, E. G. Lovell,
J. J. MacFarlane, E. A. Mogahed, G. A. Moses, R. R. Peterson, S. Rutledge,
M. E. Sawan, G. Sviatoslavsky, I. N. Sviatoslavsky, L. J. Wittenberg

Fusion Technology Institute
Department of Nuclear Engineering and Engineering Physics
University of Wisconsin-Madison
Madison, WI 53706

December 1991

UWFDM-880
FPA-91-4

Acknowledgement

Support for this work has been provided by Kernforschungszentrum Karlsruhe through Fusion Power Associates and by Sandia National Laboratories.

Table of Contents

1. Executive Summary	1.1
2. Introduction	2.1
3. Design Philosophy	3.1
3.1. Beam Transport Considerations	3.1
3.2. Choice of Reactor Coolant/Breeder	3.5
4. Overall Design	4.1
5. Targets	5.1
6. Driver	6.1
7. Diode	7.1
8. Focusing Lenses	8.1
8.1. Magnetic Field and Current Requirements	8.1
8.2. MHD and Thermal Hydraulics Aspects of Final Focus Magnet Lens	8.2
8.2.1. Introduction	8.2
8.2.2. Remarks on the thermal problem for laminar MHD channel flow of a liquid metal	8.4
8.3. Magnetic Pressure and MHD-Induced Pressure Drop	8.9
8.4. Mechanical Analysis	8.12
8.5. Conceptual Design of the Final Focus Magnetic Lens	8.13
9. Ion Propagation	9.1
10. Breeder and Coolant Choice	10.1
11. Reactor Chamber Layout	11.1
12. Chamber Gas Dynamics Analysis	12.1
12.1. Vaporization	12.1
12.2. Reactor Chamber Clearing	12.6
13. INPORT Performance	13.1

14. Neutronics Analysis	14.1
14.1. Calculational Method	14.1
14.2. INPORT Tube Region	14.1
14.3. Reactor Roof	14.5
14.4. Bottom Lithium Pool	14.6
14.5. Final Focusing Magnets	14.7
14.6. Biological Shield Design	14.8
14.7. Overall Reactor Neutronics Parameters	14.9
14.8. Neutronics Performance with Lithium Lead	14.12
15. Tritium Systems	15.1
15.1. Tritium Fuel Preparation	15.1
15.2. Tritium Breeding and Recovery	15.1
15.3. Evaluation of Tritium Inventories and Release Rates	15.2
16. Heat Transfer	16.1
16.1. Introduction	16.1
16.2. Geometry	16.1
16.3. Thermal Hydraulics Calculations	16.5
17. Power Cycle	17.1
17.1. Introduction	17.1
18. Maintenance	18.1
18.1. Final Focusing Magnets and Front INPORT Units	18.1
18.2. Rear INPORT Units	18.2
18.3. Driver Modules	18.4
19. Economics	19.1
20. Conclusions	20.1
21. Recommendations	21.1
Appendix	

1. Executive Summary

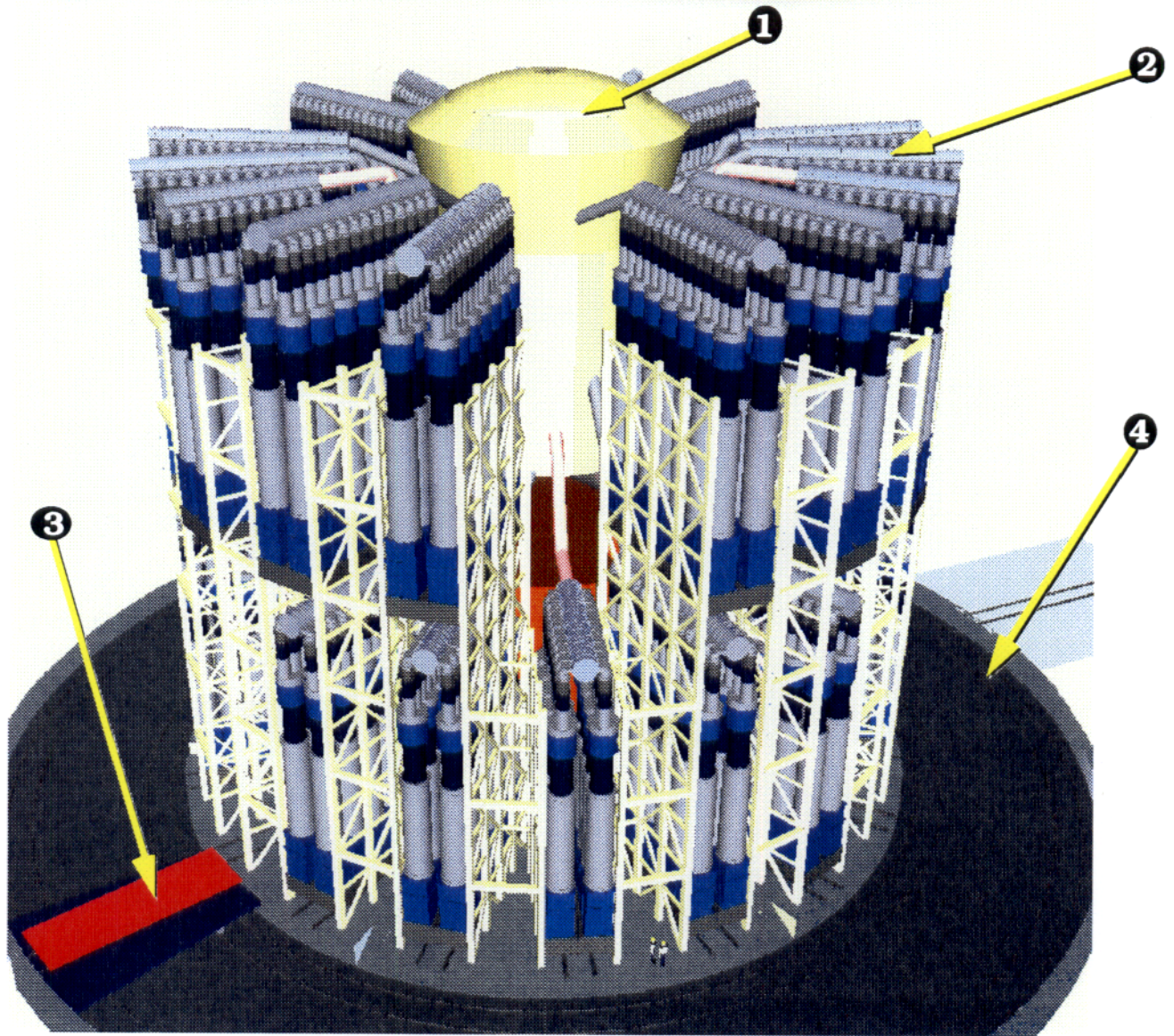
The use of light ions to implode DT filled targets in commercial fusion power plants has been studied for over 10 years. The first, in depth, self-consistent light ion driven power plant study was LIBRA (Light Ion Beam ReActor), begun in 1982 with the first open publication appearing in 1983 [1]. After 23 papers and reports (see Appendix), the LIBRA study culminated in the final design report published in 1989 [2]. Two main features of that power plant design were the relatively low net power level (331 MWe) and the reliance on channel transport of the lithium ions to the target through a 100 torr helium gas environment. Subsequent to that study, the subject of ballistic transport of ions and the benefits associated with the economy of scale were considered. In 1990 it was decided to investigate the characteristics of a 1000 MWe light ion driven fusion power plant based on the ballistic mode of particle transport. The first year of that study (labeled LIBRA-LiTE mainly because of the switch from a heavy PbLi alloy breeder/coolant to a much lighter Li breeder/coolant) was devoted to identifying the key issues that needed to be addressed. The current year (1991) was devoted to a more in-depth study of selected key issues and this report summarizes the results of the second year of the LIBRA-LiTE study. A separate video has been prepared to visually summarize the key features of this reactor design [3].

A summary of the major design parameters of LIBRA-LiTE is given in Table 1.1 and Fig. 1.1 is a schematic of the power plant.

There are four main design changes in the LIBRA-LiTE concept:

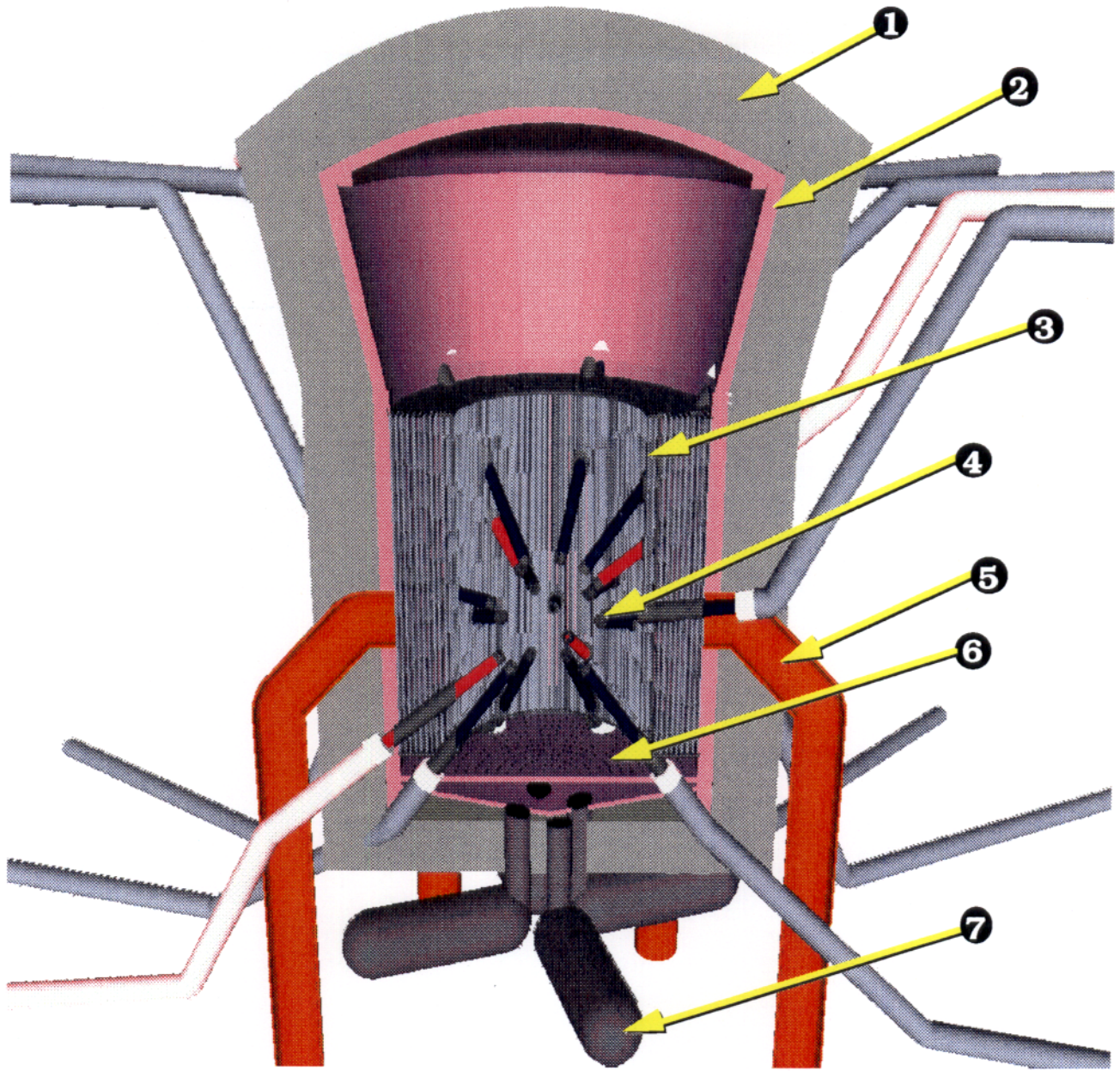
- the mode of ion transport,
- the power level of the reactor,
- the coolant/breeder material, and
- the material used to carry the current in the final focusing magnet.

Perhaps the biggest change in the LIBRA-LiTE design is the requirement the 30 MeV Li ions must be transported ballistically to the target. This choice has a profound influence on the chamber configuration (see Fig. 1.2) through the need to have a 2 tesla final focusing magnet placed as near as 2 meters from the target. The resulting neutron wall loading on the front face of the magnet then reaches $\approx 29 \text{ MW/m}^2$ which in turn limits the useful lifetime of the magnet to ≈ 1 calendar year. The ballistic transport of the Li ions to the target also requires a relatively low cavity pressure of low Z atoms to avoid excess beam losses. Such a low chamber particle density essentially dictated the use of liquid Li as a coolant/breeder and a



- (1) Reactor chamber
- (2) Driver
- (3) Transport carriage
- (4) Circumferential rails

Figure 1.1. View of LIBRA-LiTE reactor from inside containment building.



- (1) Shield
- (2) Reflector / vacuum chamber
- (3) INPORT units
- (4) Final focus magnet
- (5) Vacuum line
- (6) Perforated plate
- (7) IHX

Figure 1.2. Side view reactor chamber cutaway.

Table 1.1. Key Parameters for the LIBRA Class of Fusion Power Plants

Parameter	Units	LIBRA	LIBRA-LiTE
Net electrical power	MW _e	331	1000
Ion beam transport		Channel	Ballistic
Number of beams		18	30
Energy on target	MJ	4	6
Target gain		80	100
η_G		18.8	18
Rep rate	Hz	3	3.9
Coolant/Breeder		Li ₁₇ Pb ₈₃	Li
INPORT material		SiC	HT-9 Steel
Focus magnet material		TZM-Mo Alloy	Liquid Li/HT-9
Distance to magnet	m	3.3	2.05
Maximum n wall load-magnet	MW/m ²	4.8	29
T ₂ breeding ratio		1.36	1.41

blowdown chamber as depicted in Fig. 1.2. All of the above choices indicated the use of a liquid metal magnet to generate the final 2 T focusing fields. The choice of Li was logical following the selection of the Li coolant/breeder.

More specific information on the target/driver parameters used in this study is contained in Table 1.2.

The target of choice continues to be the ‘‘Bangerter target’’ [4] which is a combination of Pb and D-T fuel. A higher ion beam energy on target was used compared to LIBRA (6 vs. 4 MJ) which would allow a higher gain to be used (100 vs. 80). These two choices, along with a higher rep rate (3.9 vs. 3 Hz) allowed for a much higher net plant output (1000 vs. 331 MWe).

Helia technology was chosen for LIBRA-LiTE which is only a modest extrapolation from present day experience [5]. The kinetic energy of the Li ions was varied from 25 to 35 MeV and because of the need for more power (TW) on the larger target (at a constant 127 TW/cm²), more driver modules were needed (24 vs. 16 main pulse and 6 vs. 2 prepulse). To obtain the higher power level, the beam needed increased bunching. The LIBRA-LiTE peak pulse length on the target was 3.4 ns vs. 9 ns in LIBRA. All of these parameters result in the beam current

Table 1.2. Key Target/Driver Parameters for the LIBRA Class of Fusion Power Plants

Parameter	Units	LIBRA	LIBRA-LiTE
Target material		Pb/D/T	Pb/D/T
Energy on target	MJ	4	6
Rep rate	Hz	3	3.9
Target gain		80	100
Target yield	MJ	320	600
Driver technology		Helia	Helia
Ion energy	MeV	25-35	25-35
Pulse length-target	ns	9	3.4
Beam current at diode	MA	0.3	0.313
Beam current on target/channel	MA	1.1	3.69
Peak power	TW	400	1588
Peak power - target	TW/cm ²	127	127

at the target per channel being more than 3 times higher in LIBRA-LiTE (3.69 MA) when compared to LIBRA (1.1 MA).

The conversion of the thermonuclear energy into electricity is accomplished by banks of porous vertical tubes containing flowing Li. The tubes, called INPORT units [6], are made of wires of HT-9, a particularly radiation damage resistant ferritic steel (see Figs. 1.2 and 1.3). The INPORT units are arranged in layers around the target and serve to:

Table 1.3. Key Blanket Parameters for the LIBRA Class of Fusion Power Plants

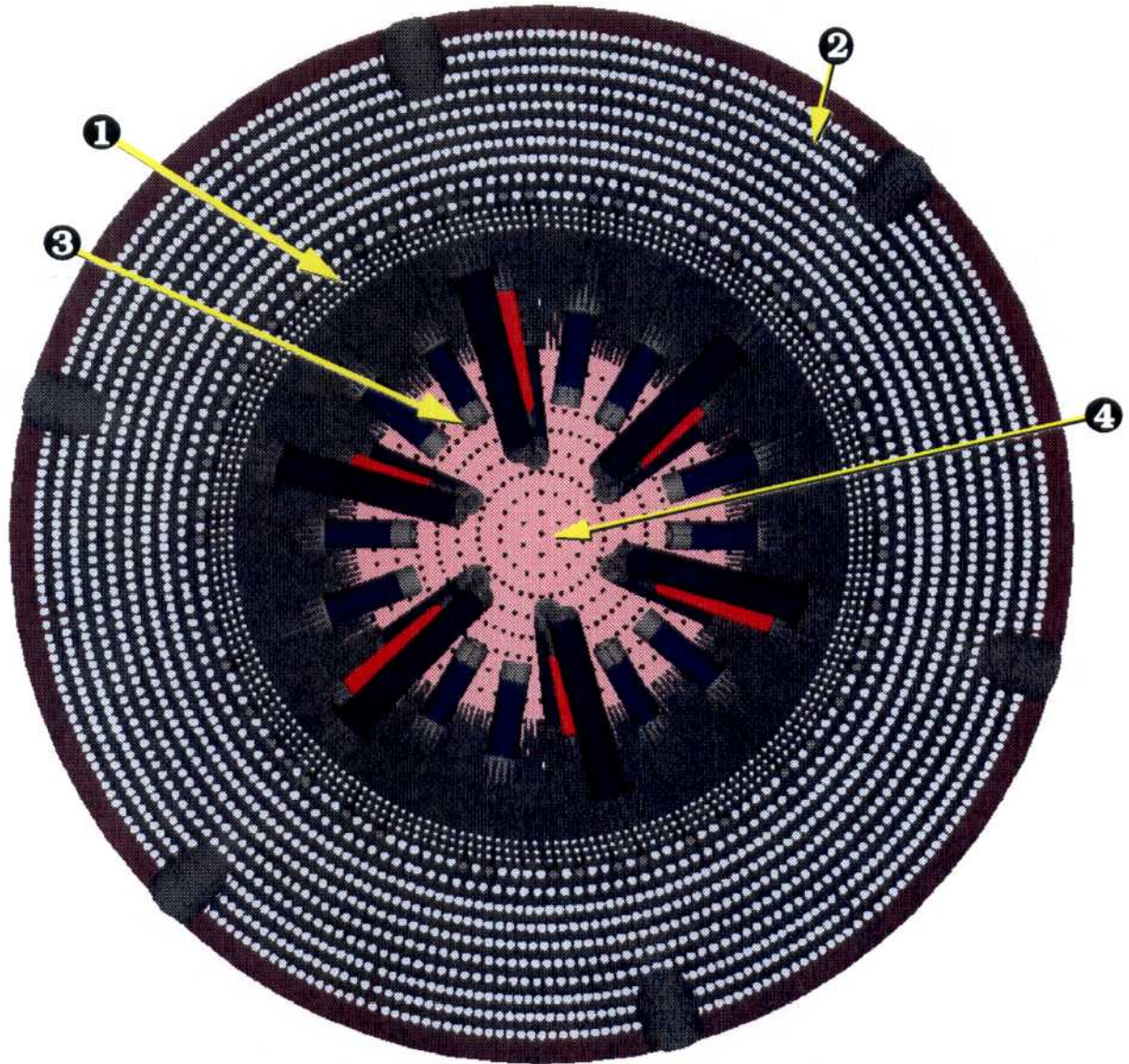
Parameter	Units	LIBRA	LIBRA-LiTE
Coolant/Breeder		Li ₁₇ Pb ₈₃	Li
Chamber pressure	torr	100	1
INPORT material		SiC	HT-9
Coolant inlet/outlet	°C	340/500	350/525
Maximum impulse INPORT	Pa-s	125	103
Mass vaporized/shot	kg	8	5.2
Energy multiplication		1.22	1.21
TBR		1.36	1.41
Maximum damage-magnet	dpa/FPY	18	200
Maximum dpa-roof/vessel	dpa/FPY	6.7	5
Maximum dpa INPORT	dpa/FPY	60	68
Magnet lifetime	CY	3	1

- Carry away the energy released by the target,
- Contain the breeding material,
- Help cool and suppress the blast wave,
- Facilitate maintenance of the material close to the target which is subjected to the high neutron fluxes.

Key parameters of the reactor chamber are given in Table 1.3.

The overall power flow for the LIBRA-LiTE reactor is shown in Fig. 1.4 and a few key parameters are included in Table 1.4.

The energy in the 525°C Li exiting the reactor chamber is transferred to a liquid lead alloy intermediate loop and ultimately to the steam generator. The gross efficiency of conversion is 44% resulting in a gross electrical output of 1192 MWe. Subtracting the 103.5 MWe in driver power, 75 MWe to drive the magnets, and 13.5 MWe in auxiliary power, one obtains a net electrical output of 1000 MWe. This represents a net overall efficiency of 38%.



- (1) Front INPORT units
- (2) Rear INPORT units
- (3) Single turn liquid Li lens magnet
- (4) Perforated bottom plate

Figure 1.3. Top view of reactor chamber inside with lithium removed.

POWER FLOW DIAGRAM FOR LIBRA-LiTE

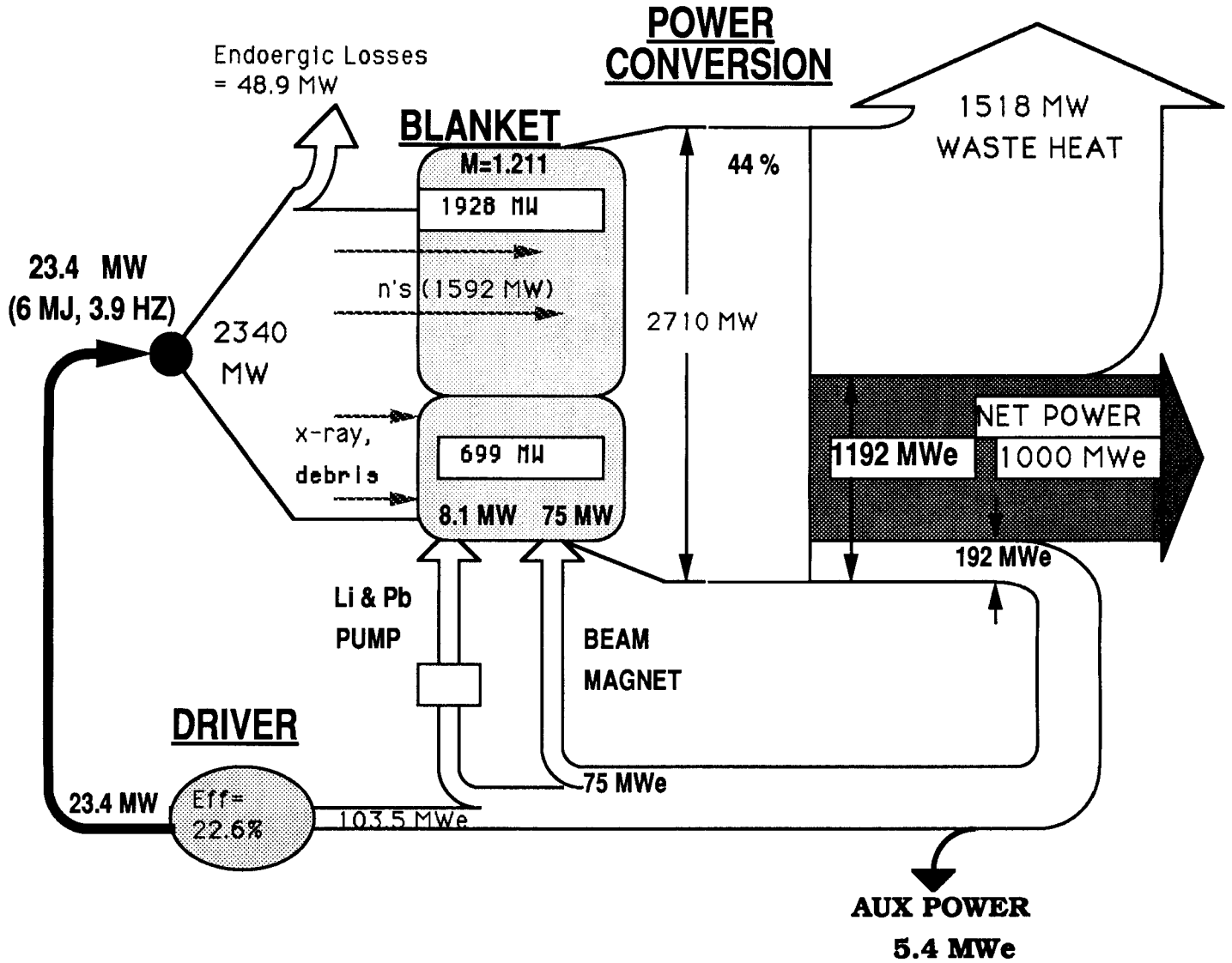


Figure 1.4. Power flow diagram for LIBRA-LiTE.

Table 1.4. Key Power Flow Parameters for the LIBRA Class of Fusion Reactors

Parameter	Units	LIBRA	LIBRA-LiTE
Fusion power	MWt	960	2400
Total nuclear power	MWt	1123	2627
Total thermal power	MWt	1161	2710
Gross electrical efficiency	%	38	44
Gross electric power	MWe	441	1192
Driver power	MWe	51	103.5
Magnet power	MWe	27	75
Auxiliary power	MWe	32	13.5
Net electric power	MWe	331	1000
Overall net efficiency	%	29.5	38.1
Direct capital cost	1991\$ per kWe	3109	1669
Cost of electricity	1991 mills/kWh	97.0	43

The cost analysis of LIBRA-LiTE was not a part of this year's activity, but preliminary estimates point to a direct capital cost of 1669 \$/kWe in 1991\$ and the levelized cost of electricity is 43 mills/kWh.

Critical areas of work to be completed in the future include the economic analysis, environmental analysis, safety analysis, and the definition of R&D necessary before a reactor like LIBRA-LiTE could be built. Nevertheless, the present design is encouraging and a fuller understanding of the benefits and penalties associated with the ballistic transport of ions to ICF targets has been made.

References

- [1] R. Engelstad and E. Lovell, "Mechanical Analysis of First Wall Tubes for the LIBRA Conceptual Reactor," Proc. 10th Symposium on Fusion Engineering, 5-9 December 1983, Philadelphia, PA, IEEE Cat. No. 83CH1916-6NPS, C. C. Hopkins et al., editors, pp. 216-219.
- [2] B. Badger, G. A. Moses, R. L. Engelstad, G. L. Kulcinski, E. Lovell, J. MacFarlane, R. R. Peterson, M. E. Sawan, I. N. Sviatoslavsky, L. J. Wittenberg, I. Smith, R. Altes,

P. Corcoran, R. Kuenning, D. Pellow, D. Wake, J. Ehrhardt, G. Kessler, E. Stein, D. L. Cook, R. E. Olson, R. W. Stinnett, "LIBRA – A Light Ion Beam Fusion Conceptual Reactor Design," University of Wisconsin Fusion Technology Institute Report UWFD-800 (revised February 1990).

- [3] "LIBRA-LiTE (Mod 2), A Commercial Light Ion Fusion Power Plant," December 1991.
- [4] R. O. Bangerter and D. Meeker, "Ion Beam Inertial Fusion Target Designs," Lawrence Livermore National Laboratory Report UCRL-78474 (1976).
- [5] D. L. Cook, to be published, *J. Fusion Energy*.
- [6] G. L. Kulcinski, G. A. Moses, J. Sapp, M. Sawan, I. N. Sviatoslavsky, D. K. Sze, and W. F. Vogelsang, "The INPORT Concept – An Improved Method to Protect ICF Reactor First Walls," *J. Nucl. Matls.*, 102 & 104, 103-108 (1981).

2. Introduction

Ever since the concept of inertial confinement fusion (ICF) was first proposed by Nuckolls [1] in 1961, scientists and engineers have been designing reactors to harness that energy. The first ICF reactors were based on lasers [2, 3] and in 1973, Yonas et al., [3] proposed using intense beams of electrons to implode targets. Shortly thereafter, in 1975, the use of high energy heavy ions was proposed [4]. In 1975, scientists first started to investigate the use of protons [5] because of difficulties associated with handling and coupling the energy in high energy electron beams to ICF targets. Scientists at the Sandia National Laboratories in the U.S. proposed using light ions heavier than protons in 1982 [6] to overcome some of the space charge problems and to facilitate the development of rep ratable diodes.

The commercial potential of using Li ions to implode ICF targets seemed so attractive in 1982 that the Kernforschungszentrum Karlsruhe (KfK), in Germany, decided to mount a small effort aimed at documenting the promises and problems of this approach. A joint effort by KfK, Fusion Power Associates, Pulse Sciences Inc., and the University of Wisconsin was initiated in 1982. The design effort, called the LIBRA (Light Ion Beam ReActor) project, was later joined by Sandia National Laboratory. The LIBRA project continued until 1989 and is documented in 23 papers and reports (listed in the Appendix). The final design document on LIBRA was issued in 1989 [7].

The LIBRA concept relied on channel transport of sixteen 1.1 MA beams over a distance of 5.4 meters. The beams were transported 3 times a second to targets injected at high velocities. In addition, a low power level of nominally 300 MWe was selected to explore the contention that light ion beam reactors could be economically competitive at much lower power levels than magnetic or even other ICF approaches (i.e., lasers, heavy ion beams). While the final design was indeed attractive, questions still remain about the ability to handle a mega-amp of Li ions in the channel transport mode.

In late 1989, it was decided that the implications of ballistic transport should be explored in the context of a larger power plant (≈ 1000 MWe). A small effort between KfK, FPA, UW, and SNL was initiated in 1990. The first year was spent in exploring the broad implications of the change in transport mode [8]. In 1991, some preliminary designs were presented [9, 10], and more in depth analysis of a few critical problems was conducted. The rest of this report summarizes the work performed in calendar year 1991.

References

- [1] The early reports at ICF were classified and the historical record was reviewed publically by L. Wood and J. Nuckolls at the 1971 AAAS meeting in Philadelphia.
- [2] A. P. Fraas, Oak Ridge National Laboratory Report, ORNL-TM-3231, July 1971.
- [3] L. A. Booth (ed.), Los Alamos National Laboratory Report, LA-4858-MS, February 1972.
- [4] G. Yonas, et al., *Nuclear Fusion*, **14**, 731 (1979).
- [5] M. J. Clauser, "Ion Beam Implosion of Fusion Targets," *Phys. Rev. Letters*, **35**, **3**, 848 (1975).
- [6] D. L. Johnson, W. L. Nean and B. N. Turman, "PBFA-II Conceptual Design," Proc. 4th IEEE Pulsed Power Conf., Albuquerque, NM, p. 54 (1983).
- [7] B. Badger, G. A. Moses, R. L. Engelstad, G. L. Kulcinski, E. Lovell, J. MacFarlane, R. R. Peterson, M. E. Sawan, I. N. Sviatoslavsky, L. J. Wittenberg, I. Smith, R. Altes, P. Corcoran, R. Kuenning, D. Pellow, D. Wake, J. Ehrhardt, G. Kessler, E. Stein, D. L. Cook, R. E. Olson, R. W. Stinnett, "LIBRA – A Light Ion Beam Fusion Conceptual Reactor Design," University of Wisconsin Fusion Technology Institute Report UWFD-800 (revised February 1990).
- [8] D. Bruggink, R. L. Engelstad, G. L. Kulcinski, E. G. Lovell, J. J. MacFarlane, E. A. Mogahed, G. A. Moses, R. R. Peterson, M. E. Sawan, G. Sviatoslavsky, I. N. Sviatoslavsky, L. J. Wittenberg, "Annual Review of LIBRA-LiTE Project: Research Performed During Calendar Year 1990," FPA-90-3, December 1990.
- [9] G. L. Kulcinski, "LIBRA-LiTE: A 1000 MWe Reactor," University of Wisconsin Fusion Technology Institute Report UWFD-857, June 1991; to be published in *J. Fusion Energy*.
- [10] R. R. Peterson, R. L. Engelstad, G. L. Kulcinski, E. G. Lovell, J. J. MacFarlane, E. A. Mogahed, G. A. Moses, S. Rutledge, M. E. Sawan, I. N. Sviatoslavsky, G. Sviatoslavsky, L. J. Wittenberg, "LIBRA-LiTE, A Light Ion Inertial Confinement Fusion Reactor With Ballistic Ion Propagation," University of Wisconsin Fusion Technology Institute Report UWFD-864, September 1991.

3. Design Philosophy

The major driving force behind the LIBRA-LiTE reactor design is the need to find a more credible and reliable way to transport a total of several MA's of Li ions from the diodes to a 2 cm diameter target which may be as much as 5 meters away. The “traditional” way of accomplishing this is by the method of channel transport. However, there is some uncertainty that such beams can be focused and transported in that mode.

The transport of ions ballistically has been accomplished for decades and would be a less controversial technique than the channel transport scheme. However, even this approach has major drawbacks. The largest concern stems from the need to have a diode with an extremely low microdivergence in order that the final focusing magnets can be removed to a reasonable standoff distance from the target.

Another significant driving force in LIBRA-LiTE is the desire to explore the economy of scale in light ion fusion power plants. The LIBRA design showed that a 331 MWe power plant could be competitive with magnetic fusion designs. It was expected that if the power level was raised to ≈ 1000 MWe, the economics would improve considerably.

It will be shown below that in order to accomplish the first two goals, namely to achieve ballistic focus of the ions and higher power levels, some major changes in the LIBRA reactor design were necessary. The proposed changes also required some innovation in the design of magnets that could successfully operate under extreme neutron environments. The thrust of this chapter is to outline the logic path that was followed in coming to the final design point.

3.1. Beam Transport Considerations

In order to use a ballistically focused beam, one must place a final focusing magnet between the diode and the target. Because of the high radiation levels released from the target, it would be advantageous to keep the final focusing magnet (FFM) as far from the target as possible. Unfortunately, the laws of physics reveal a fundamental relationship between the final spot size, the focal length, the scattering of the ion beam by the background gas, and the initial microdivergence of the diode,

$$\Delta r \approx \Theta_{\mu} f F(\sigma_s)$$

where

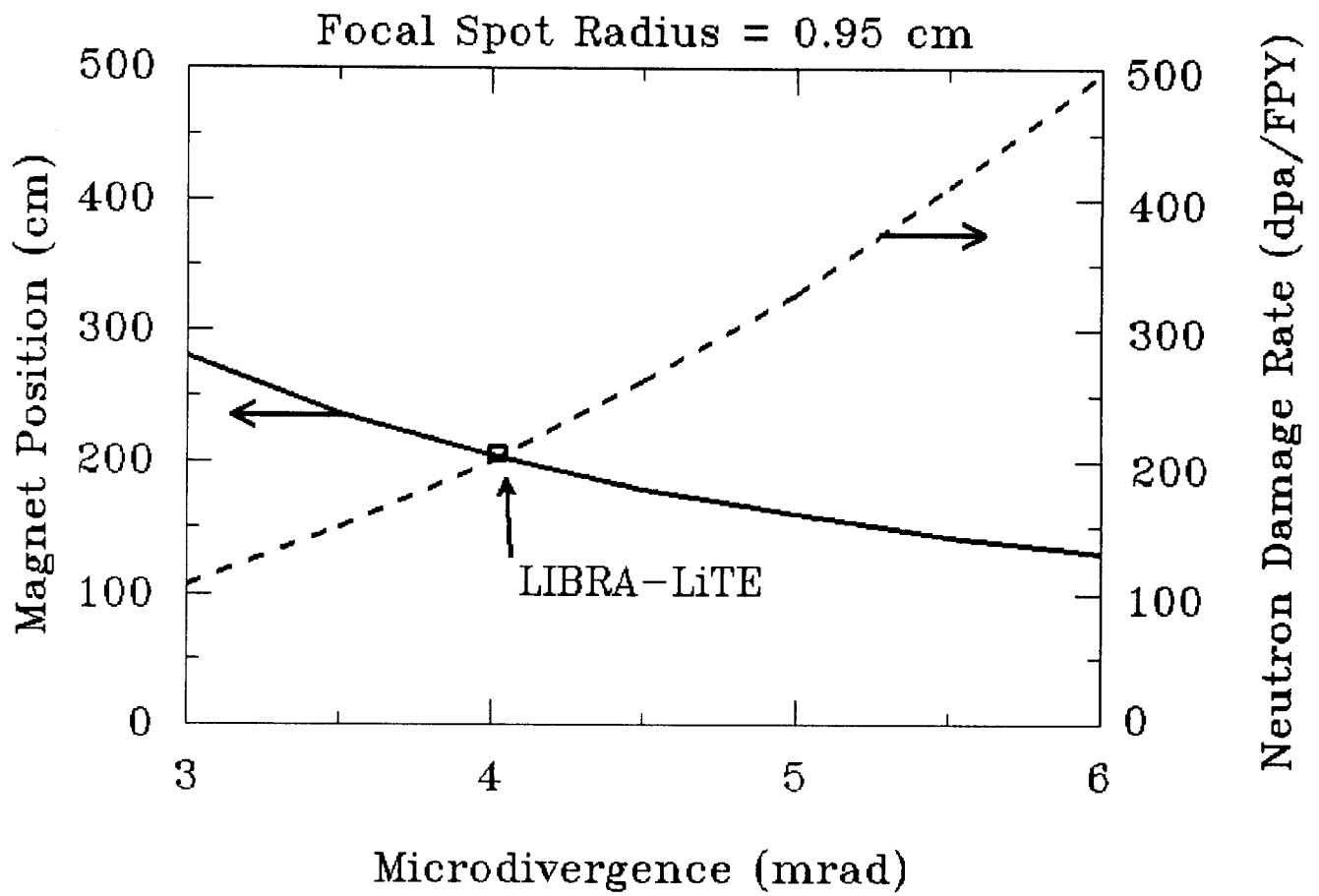


Figure 3.1. Magnet position and neutron damage rate as a function of microdivergence.

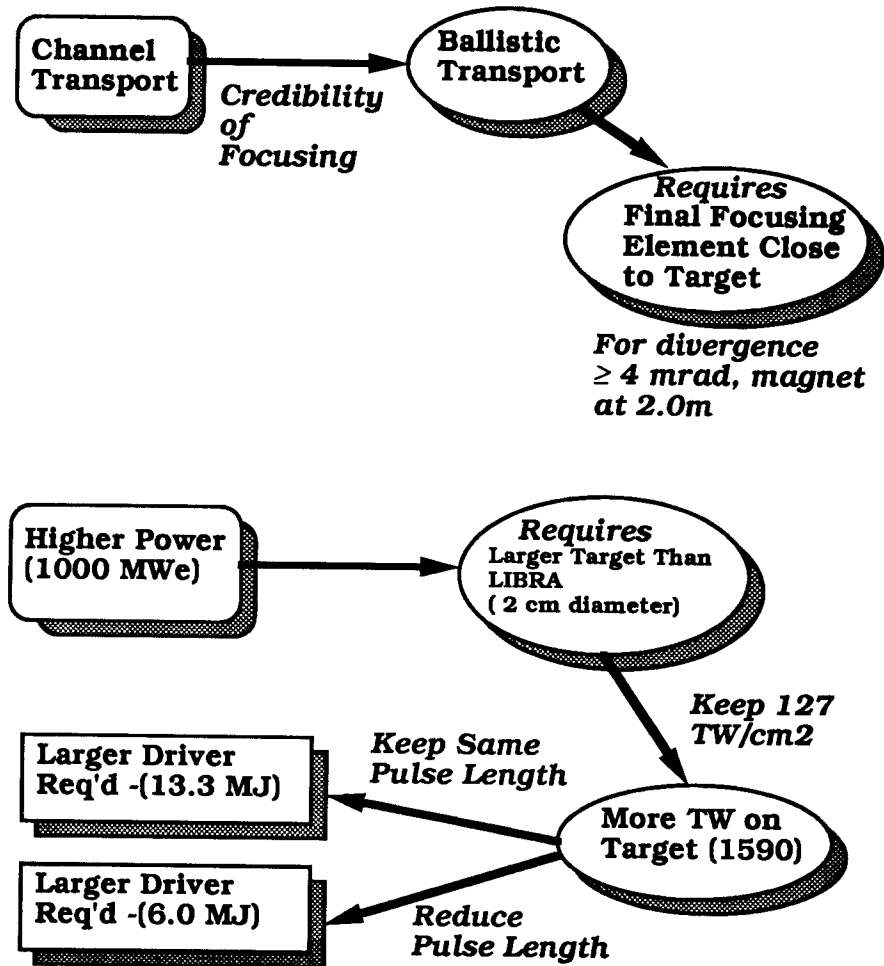


Figure 3.2. Logic behind choice of present LIBRA-LiTE design point.

achieve a gain of 80 at 4 MJ, then it is entirely conceivable that the LIBRA-LiTE target could reach a gain of 100 at 6 MJ.

The yield of 600 MJ per shot was then tested to see if the blast wave could be withstood by the FFM's and by the Li coated steel INPORT tubes. Once that determination was made, then the rate of cavity clearing had to be calculated. An analysis of the power loop conversion efficiency and recirculating power fraction was then coupled to the cavity clearing rate by an iterative process to arrive at a ≈ 4 Hz rep rate for an approximate 1000 MWe net plant output.

Further refinement of the calculations revealed that the ultimate repetition rate needed was 3.9 Hz with a 550°C Li coolant outlet temperature. The final analysis also revealed the the damage rate to a FFM at 2.05 meters from the target was 200 dpa/FPY, consistent with at least a one calendar year lifetime. However, the high neutron flux did mandate a nonconventional magnet design. A liquid magnet design was chosen, which is described in more detail in Chapter 8.

3.2. Choice of Reactor Coolant/Breeder

The search for an appropriate coolant/breeder was quickly narrowed down to the $\text{Li}_{17}\text{Pb}_{83}$ alloy and liquid Li. A detailed comparison of the neutronic and safety attributes of both systems was then made (see Chapter 10). A summary of the conclusions is given in Table 3.1.

It should be clear from Table 3.1 that the use of Pb in the LIBRA-LiTE chamber causes more degradation of the LIBRA-LiTE parameters than improvement. The higher atomic number Pb atoms interfere with the transport of the ion beam and are more difficult to clear from the cavity in the ≈ 250 ms available than is Li. The increased (n,2n) reactions mean that the radiation damage rates are higher, resulting in shorter lifetimes for the FFM's and the INPORT units. The higher electrical resistance results in more I^2R losses in the magnets (which already require ≈ 75 MWe in Li). The PbLi alloy requires higher ^6Li enrichment, and coupled with its thermal properties, is more expensive than Li. The higher density makes structural support more of a problem, and a higher impulse pressure coupled with larger isochoric heating produces a larger dynamical response in the INPORT units. Finally, the low solubility of tritium in the PbLi alloy results in a larger T_2 leakage through the heat exchanger.

There are two areas where PbLi and Li are essentially the same and that is with respect to overall tritium breeding ratios and energy multiplication. On the positive side, the low tritium inventory is a distinct safety advantage in the event of an off-normal accident. Similarly, the lack of an explosive reaction with water or concrete is also a definite safety advantage.

Table 3.1. Impact of Using $\text{Li}_{17}\text{Pb}_{83}$ Instead of Li on the Performance Of LIBRA-LiTE

Parameter	Degradation	No Effect	Improvement
Maximum rep rate	Lowered		
Ion beam transport	Worse		
Li enrichment	Require higher level		
Overall TBR		Same	
Overall energy multiplication		Same	
INPORT unit lifetime	Shorter		
Magnet lifetime	Shorter		
Magnet power	Higher		
Structural support	More required		
Isochoric heating	Higher		
Impulse pressure	Higher		
INPORT dynamic response	Greater		
Tritium inventory			Lower
Tritium leakage to secondary loop	Higher		
Safety concerns			Lower
Cost	Higher		

In the final analysis it was determined that liquid Li was the best choice for LIBRA-LiTE and the Pb-Li eutectic alloy was considered as a backup.

References

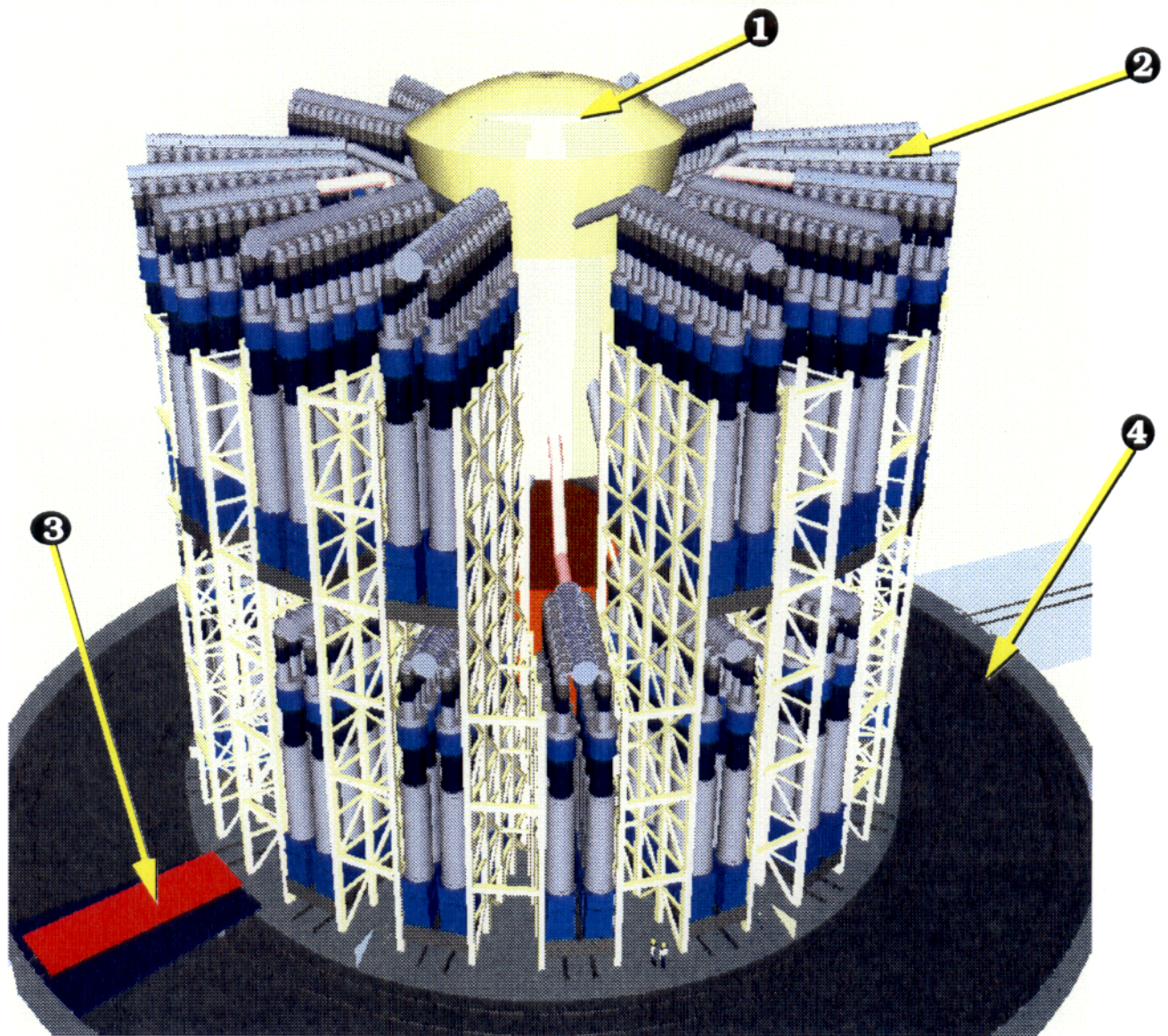
- [1] C. L. Olson, "Achromatic Magnetic Ion Systems for High Current Ion Beams," Proc. 1988 Linear Accelerator Conf., Williamsburg, VA, Oct. 3-7, 1988.
- [2] R. O. Bangerter, "Targets for Heavy Ion Fusion," *Fusion Technology*, **13**, 348 (1988).

4. Overall Design

LIBRA-LiTE is a conceptual design study of an inertially confined 1000 MWe fusion power reactor utilizing light ion beams. The target is illuminated with 6 MJ of 30 MeV Li ions with a surface flux on target of 127 TW/cm^2 . There are thirty ion beams altogether, six of which are prepulse beams. The ions are transported ballistically and are focused onto the target with magnets located 2.05 m from the point of implosion. The six prepulse beams are oriented as though they were incident in the middle of each side of a cube located with two corners coincident with the chamber axis and with the cube center at the target. The remaining 24 main pulse beams are divided into four groups of six beams each, in which the beams in a group lie on the surface of a cone with its vertex at the target and its axis coincident with the chamber axis. There are two inverted cones with angles of 74 degrees and 160 degrees, and two upright cones with the same angles.

The drivers for the 30 beams are situated around the chamber at two levels, with 15 drivers at each level. Figure 4.1 is a side view of the reactor showing the driver modules surrounding the chamber with the containment building wall removed for clarity, and Fig. 4.2 is a top view. It can be seen from Fig. 4.2 that although the driver modules are uniformly distributed around the chamber, the beam lines in some cases have to make several bends in order to reach their proper location at the chamber. Also note that the driver modules are divided into 18 sectors, 20 degrees apart. Both upper and lower level driver modules are grouped into three groups of five modules, with the three intervening sectors empty. Driver modules which line up vertically are mounted on overlapping frames, while those which occupy a sector by themselves are mounted on individual frames. There is a set of circumferential rails which surround the reactor on the outer periphery. These rails are used to transport driver modules to hot cells for maintenance.

Figure 4.3 is a cross sectional view of the reaction chamber which is an upright cylinder with an inverted conical roof resembling a mushroom, and a pool floor. The vertical sides of the cylinder are covered with a blanket zone consisting of many porous flexible ferritic steel tubes with a packing fraction of 33% through which the breeding/cooling material, liquid lithium, flows. This blanket zone, besides breeding T_2 and converting neutron energy to thermal energy, also provides protection to the reflector/vacuum chamber so as to make it a lifetime component. The radius to the first row of tubes is 3.45 m, the thickness of the blanket zone is 2.25 m and the length of the tubes is 11.8 m. The porous flexible tubes called INPORT (Inhibited flow Porous Tubes) units are made of tightly woven HT-9 ferritic steel wires resembling a fire hose. The idea behind the concept is to make the tubes flexible, so they can absorb shock, to make them porous so they can maintain a wetted surface and to surround the liquid with a fabric



- (1) Reactor chamber
- (2) Driver
- (3) Transport carriage
- (4) Circumferential rails

Figure 4.1. Side view of the reactor with containment building wall removed.

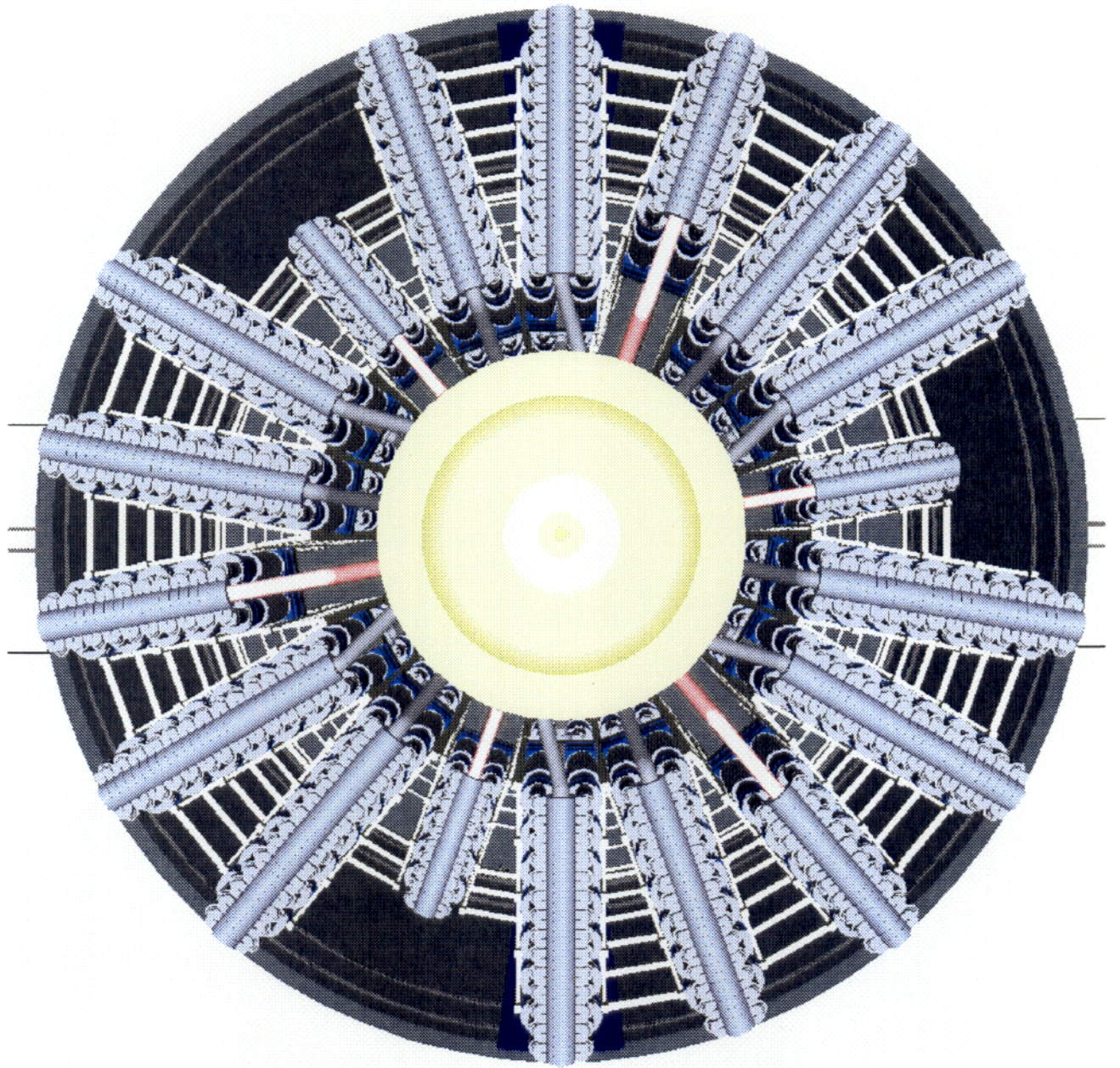
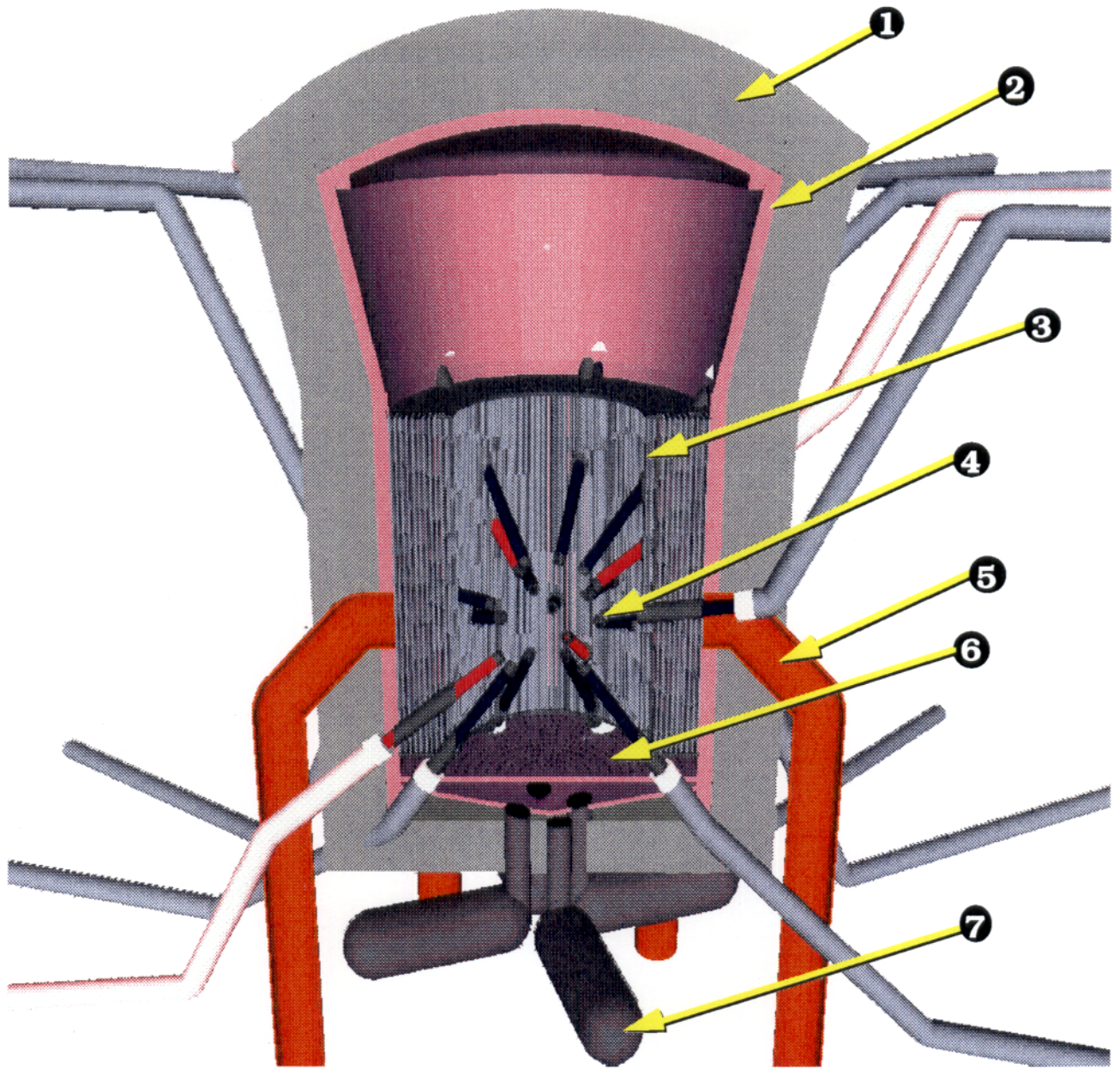


Figure 4.2. Top view of reactor with roof of containment building removed.



- (1) Shield
- (2) Reflector / vacuum chamber
- (3) INPORT units
- (4) Final focus magnet
- (5) Vacuum line
- (6) Perforated plate
- (7) IHX

Figure 4.3. Cross-sectional view of the reactor chamber.

to prevent the disassembly of the liquid Li stream due to isochoric heating from the neutrons after each shot. There are three rows of 5 cm diameter INPORT units arranged at 10 cm between centerlines in the circumferential direction as well as between rows. These front tubes are configured to totally shadow the rear zone, and the spaces between the rows are determined from dynamic motion considerations. The rear tubes are 12 cm in diameter and there are 14 rows of them. Their sole function is to transport the Li which moderates neutrons and breeds T_2 . Behind the blanket is a 50 cm thick HT-9 ferritic steel reflector which is also the vacuum boundary. Finally, the whole chamber is surrounded by a steel reinforced concrete shield which varies in thickness from place to place but is nominally 2.7 m. Figure 4.3 also shows vacuum tubes located behind the blanket zone at the chamber midplane. There are six such tubes leading to an expansion tank situated below the reaction chamber. The function of this tank is to provide volume for the vapor to expand into, following a shot. As the vapor flows into the expansion tank it exchanges heat with the INPORT units, and cools itself by virtue of an isentropic expansion. Vacuum pumps which are attached to the expansion tank then evacuate the noncondensable species in preparation for the next shot.

The chamber roof is not protected with INPORT units and for this reason is removed to a distance of 16 m from the target, making it also a lifetime component. The roof with its integral shield is designed to be removed to provide access during internal reactor chamber component maintenance. Since the roof will be cooled, it also will condense vapor and have a wetted surface which will be vaporized after each shot. Another function of the mushroom shape is to protect the side walls which are shadowed by the INPORT units and to provide additional volume in the chamber for the vapor to expand into.

Figure 4.3 shows a view of the inside of the chamber with only 18 of the 30 beam lines and final focusing magnets visible. These magnets are steady state and consist of five turns of liquid Li conductor. The magnets are 50 cm long and have an inner bore of 18 cm, an outer diameter of 43.6 cm and provide an average field of 1.2 tesla. The front surface of the magnet facing the target experiences a very high heat flux and for this reason is made of a Mo alloy TZM. This side is designed to maintain a wetted surface to absorb heat by evaporation. The rest of the magnet body is made of ferritic steel HT-9. The final focusing magnets as well as the front INPORT units are supported on a frame which can be summarily removed from the chamber during maintenance. The estimated life of these components is one calendar year.

The Li coolant enters the reactor at 350°C and exits at 525°C. After flowing through the blanket the Li collects into the bottom pool from which it drains through a perforated plate into a sump leading to the intermediate heat exchangers (IHX) located in the base of the chamber. In the IHX the Li exchanges heat with liquid lead, which in turn is pumped to a

5. Targets

The exact dimensions and materials for the target used in the LIBRA-LiTE reactor concept will not be clearly defined in this report. A set of assumptions as to its general geometry, materials, driver requirements, and output is made. It is assumed that the target has the same general geometry as the generic ion beam target design proposed several years ago by scientists at Lawrence Livermore National Laboratory (LLNL) [1]. All ion targets require ions that deposit in approximately the same range, so the target designs for light ion fusion may be similar to this LLNL design. This design is depicted in Fig. 5.1. The target is made of cryogenic DT fuel frozen in a hollow spherical shell, surrounded by a plastic shell and outer shell of lead. It is assumed that the driver illumination symmetry required and the size of the target are the same as in the recent Laboratory Microfusion Facility (LMF) [2] considerations. Therefore, a target radius of approximately 1 cm is used. It is also assumed that the driver ions are divided into 30 beams; 24 main pulse beams and 6 prepulse beams. The main beams, containing 90% of the ion energy in 30 MeV lithium ions, are arranged in 4 cones at 53° and 10° above and below the target equator, with 6 beams in each cone. The prepulse beams contain 10% of the ion energy in 20 MeV lithium ions in 6 beams positioned on the faces of a cube. The approximate temporal shape of the beam is shown in Fig. 5.2, where one can clearly see the main and prepulse.

It is assumed that the size of the driver is set by the requirement that the power intensity on the target in the main pulse is 127 TW/cm^2 . Since it is assumed that the target is 1 cm in radius, a plot can be made of the required energy on target from the main pulse versus pulse width, which is shown in Fig. 5.3. In doing this, it is assumed that one can continuously change the design of the target to ignite and burn for these varying parameters. A main pulse width of 3.4 ns will require 5.4 MJ of energy in the main pulse. Therefore, the prepulse will contain 0.6 MJ in a 40 ns wide pulse, which will provide 1.2 TW/cm^2 . The gain curve for the LLNL target design is shown in Fig. 5.4, which shows that a gain of 100 is credible for 6 MJ driver energy. The yield is therefore 600 MJ. The target parameters are summarized in Table 5.1.

Target injection and heating have been considered in the LIBRA study [3] and no additional calculations have been done for LIBRA-LiTE. The target design is essentially the same for both reactor designs. The target chamber gas density is lower in LIBRA-LiTE so frictional heating of the target will be lower. The wall temperatures are comparable. Since it was found that the plastic in the LIBRA target had a low enough thermal diffusivity to prevent unacceptable heating of the cryogenic fuel, it is believed that the LIBRA-LiTE target will survive. No reason is seen why the pneumatic target injector used in HIBALL [4] and LIBRA would not work in LIBRA-LiTE.

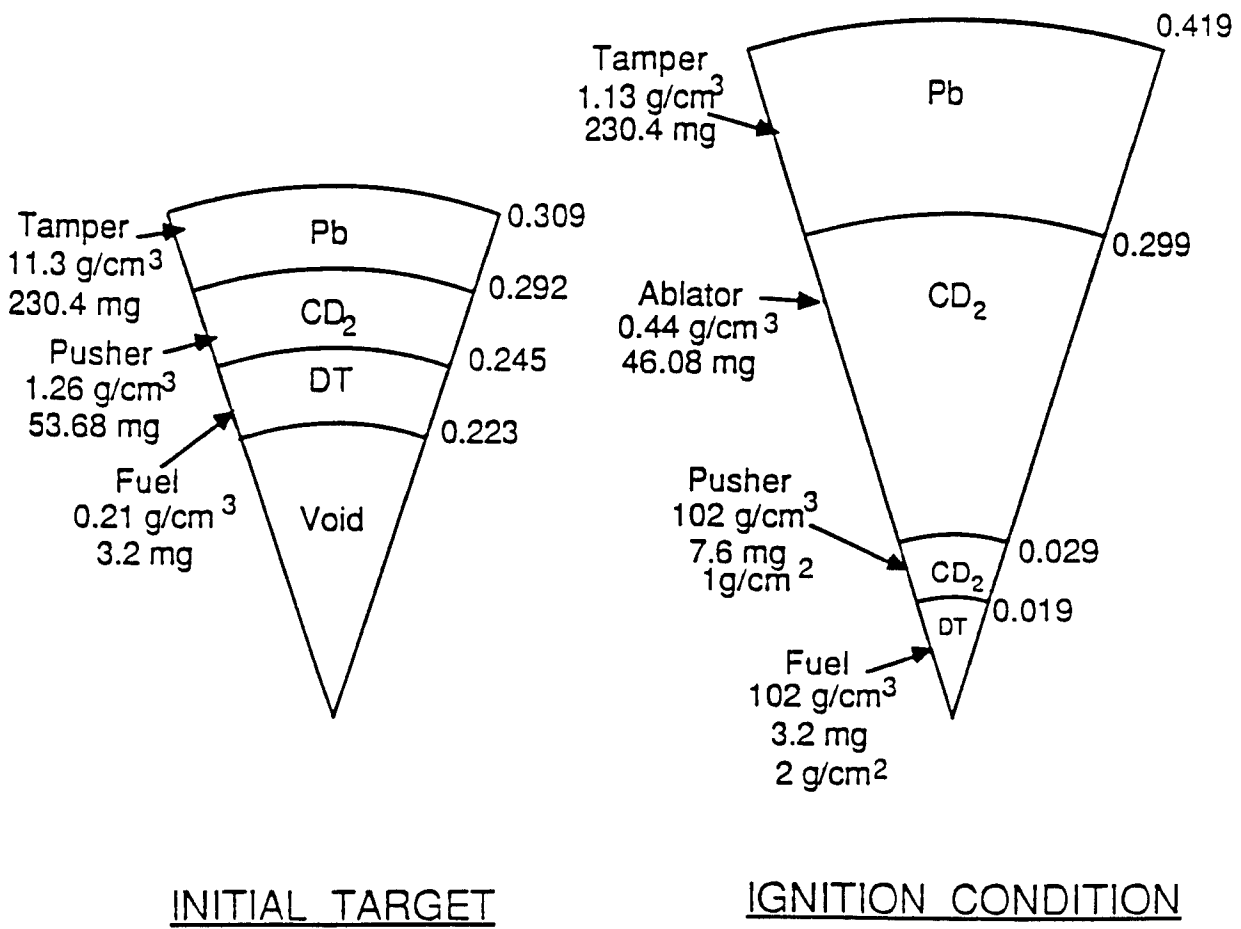


Figure 5.1. Proposed LIBRA-LiTe target design.

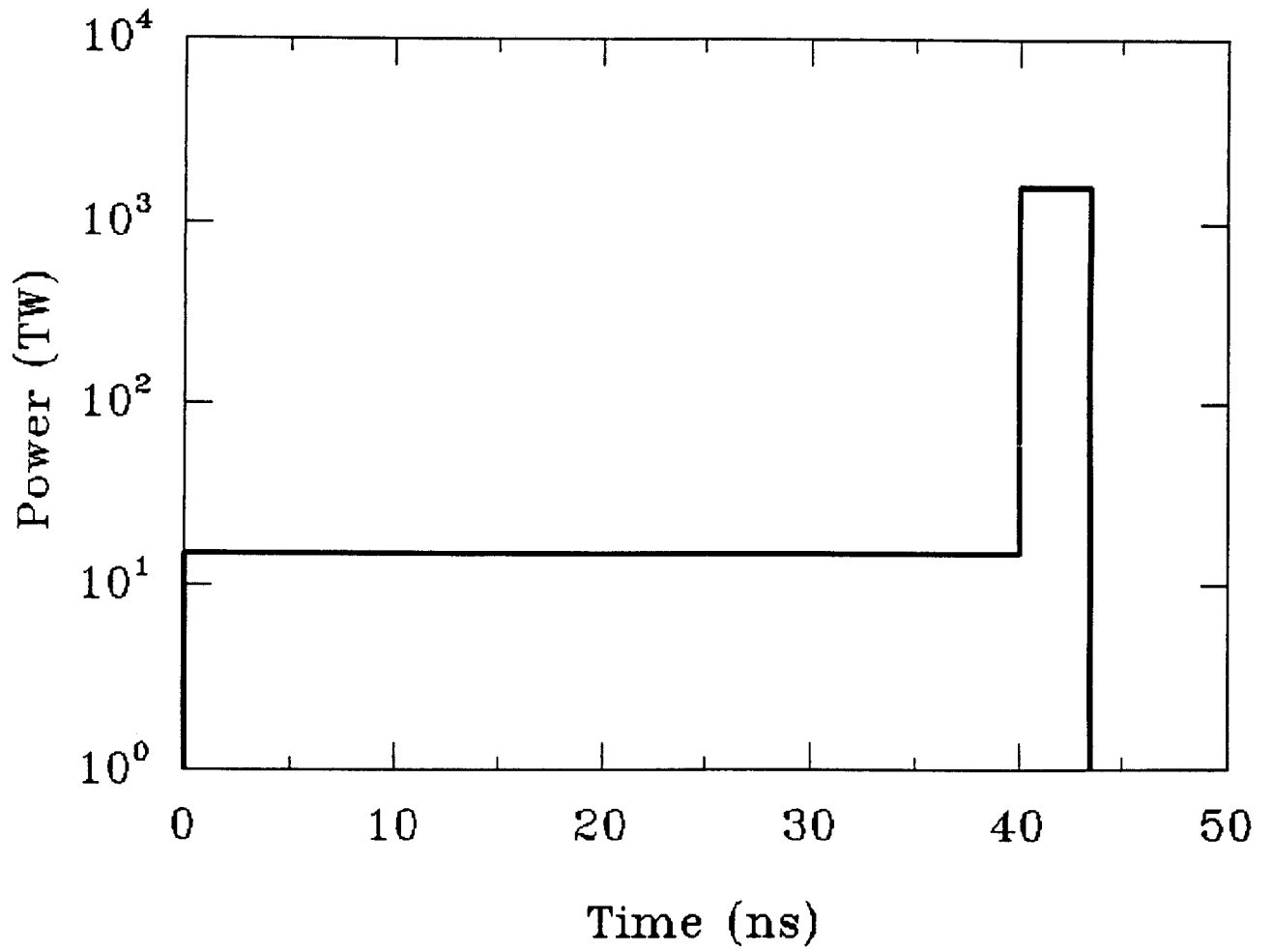


Figure 5.2. Approximate pulse shape.

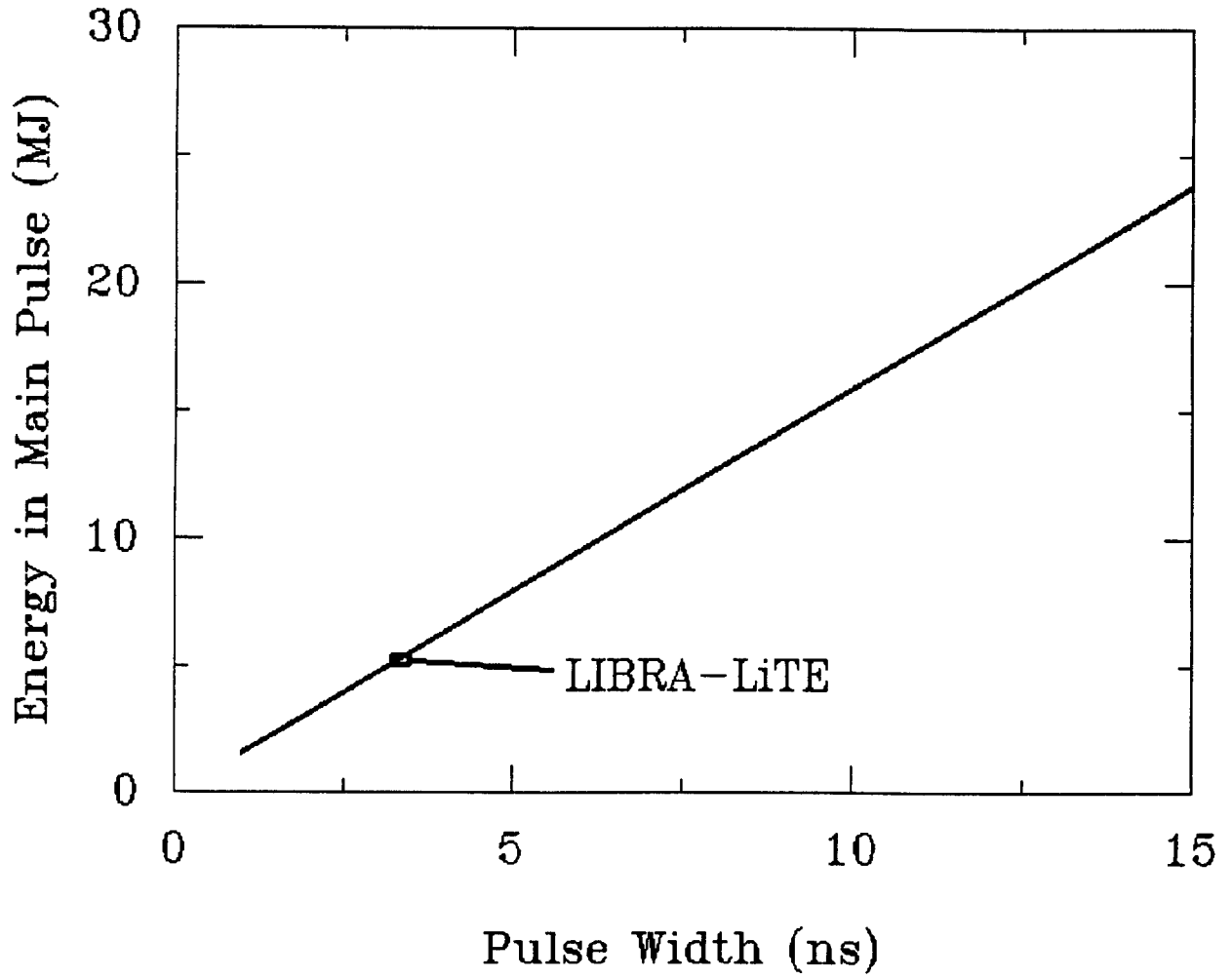


Figure 5.3. Main pulse energy on target versus pulse width. The target radius is 1 cm.

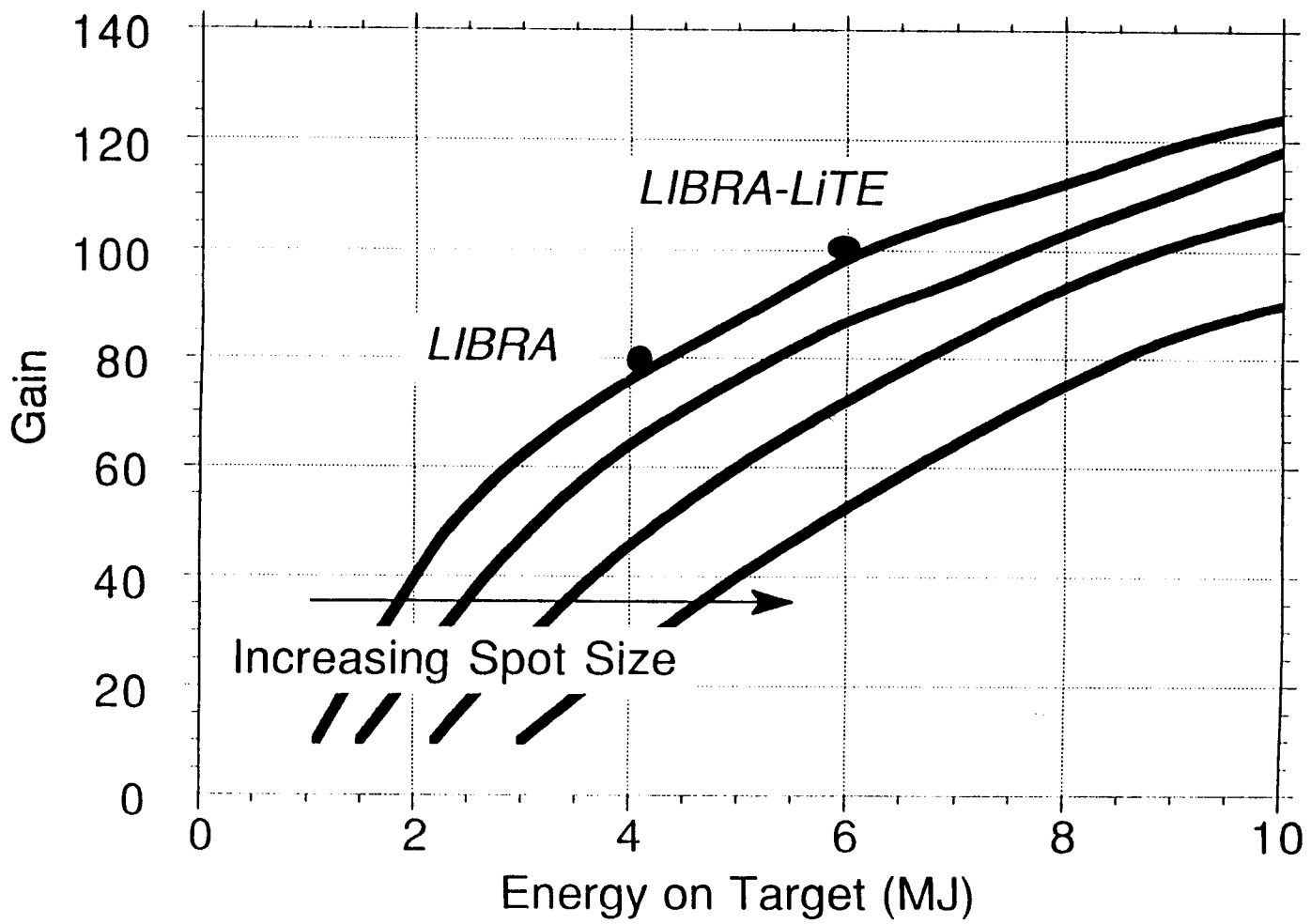


Figure 5.4. Gain curve for LLNL heavy ion target.

Table 5.1. Target Parameters

Target type	Indirect drive	
Total energy on target (MJ)	6.0	
Target gain	100	
Target yield (MJ)	600	
Target radius (cm)	1.0	
Number of beams	30	
<hr/>		
	Main Pulse	Prepulse
<hr/>		
Energy on target (MJ)	5.4	0.6
Pulse width (ns)	3.4	40
Ion energy (MeV)	30	20
Power on target (TW)	1588	15
Power intensity on target (TW/cm ²)	127	1.2
Number of beams	24	6
<hr/>		

References

- [1] R. O. Bangerter, "Targets for Heavy Ion Fusion," *Fusion Technology*, **13**, 348 (1988).
- [2] J. J. Ramirez, et al., "Design Issues for a Light Ion Beam LMF Driver," *Fusion Technology*, **15** 2A, 350 (1989).
- [3] G. A. Moses, et al., "LIBRA - A Light Ion Beam Fusion Conceptual Reactor Design," Proc. 7th Int. Conf. High-Power Particle Beams, Karlsruhe, Germany, July 4-9, 1988, 148.
- [4] D. Boehne, et al., "HIBALL - A Conceptual Design Study of a Heavy-Ion Driven Inertial Confinement Fusion Power Plant," *Nucl. Engr. and Design*, **73**, 195 (1982).

6. Driver

The driver for LIBRA-LiTE is 30 pulsed-power modules that provide high voltage electrical energy to ion diodes. The main pulse is powered by 24 modules applying 30 MV to the diodes; the prepulse from 6, 20 MV modules. All 30 modules are of the same technology used in the Hermes-III [1] electron accelerator at Sandia National Laboratories. This technology uses rotating machinery and step-up transformers in a charging pulseline (CPL) to convert wall plug electrical power into $0.75 \mu\text{s}$ pulses of 2.7 MV. The CPL's feed pulse forming lines (PFL) that drive Metglas induction cells in 1.15 MV, 39 ns pulses. In fact, the voltage provided by the PFL's is ramped to provide time-of-flight bunching in the ion beams. Two PFL's drive each cell. Each main module is made of 26 induction cells. Each prepulse module is constructed with 18 modules.

The driver parameters are set by the target requirements and the performance of the diodes and transport system. The target is to receive 5.4 MJ in the main pulse and 0.6 MJ in the prepulse. It is assumed that the transport efficiency is 60%, so each of the 24 main diodes must generate 0.375 MJ of 30 MeV lithium ions. It is assumed that the ion diodes are 80% efficient, so 0.469 MJ of pulsed power is supplied to each main pulse diode. Similarly, each of the 6 prepulse diodes must provide 0.167 MJ of 20 MeV lithium ions from 0.208 MJ of pulsed power energy. The LIBRA [2] reactor design requires 0.45 MJ of 30 MV pulsed-power on the main pulse diodes, so the LIBRA pulsed power design can be easily scaled to 0.469 MJ. The prepulse pulsed-power modules are not easily scaled from any existing designs. Hermes-III provides 0.350 MJ of 20 MV pulsed power but in negative polarity (positive polarity is required for LIBRA-LiTE). The main pulse modules scaled down to 18 induction cells would provide 0.324 MJ, which means that Hermes-III is a better demonstration of the main pulse modules than the prepulse modules. Therefore, a detailed design of the prepulse modules does not exist. The main modules are scaled up 3% in current from the LIBRA modules.

The essential parameters for LIBRA-LiTE are shown in Table 6.1. The overall driver requirements and the parameters chosen for the main and prepulse driver modules are listed. Also listed are the parameters for main pulse modules in the LIBRA design and the parameters for Hermes-III. The only existing module on this list is Hermes-III. Hermes-III normally operates in negative polarity, meaning the inner conductor is charged negatively. To couple properly to an extraction ion diode, the inner conductor should be positively charged. Pulsed power in positive polarity is believed to be possible, but more experimental verification is needed. The same holds true for ramped voltages, which are required for time-of-flight bunching. It is not a feature of Hermes-III, but is believed to be possible.

Table 6.1. Driver Parameters

Total LIBRA-LiTE on target				
Total energy (MJ)	6.0			
Prepulse energy (MJ)	0.6			
Prepulse width (ns)	40			
Prepulse power (TW)	15			
Prepulse intensity (TW/cm ²)	1.19			
Number of prepulse beams	6			
Main pulse energy (MJ)	5.4			
Main pulse width (ns)	3.4			
Main pulse power (TW)	1588			
Main pulse intensity (TW/cm ²)	127			
Number of main beams	24			
Modules	Main	Prepulse	LIBRA	Hermes-III
Energy to diode (MJ)	0.469	0.208	0.450	0.350
Current to diode (MA)	0.391	0.260	0.375	0.673
Pulse width to diode (ns)	40	40	40	26
Voltage to diode (MV)	30	20	30	20
Ramped?	Yes	No	Yes	No
Polarity	+	+	+	-
Overall Driver	Main	Prepulse		
Driver efficiency (%)	37.6	37.6		
Diode efficiency (%)	80	80		
Transport (%)	60	60		
Energy into beams (MJ)	9	1.0		
Energy into diodes (MJ)	11.25	1.25		
Prime stored energy (MJ)	30	3.3		

References

- [1] J. J. Ramirez, "Hermes-III - A 16 TW Short Pulse Gamma Ray Simulator," Proc. 7th Int. Conf. High-Power Particle Beams, Karlsruhe, Germany, July 4-9, 1988, 148.
- [2] G. A. Moses, et al., "LIBRA - A Light Ion Beam Fusion Conceptual Reactor Design," Proc. 7th Int. Conf. High-Power Particle Beams, Karlsruhe, Germany, July 4-9, 1988, 148.

7. Diode

Applied magnet field extraction diodes are proposed to generate the ions. The same methodology suggested in the LIBRA [1] study is used to design these diodes. A schematic picture of an extraction applied magnetic field diode is shown in Fig. 7.1. In recent years, significant progress has been made in the understanding of the physical processes. A theoretical model for applied magnetic field diodes has been developed [2]. Theoretical and numerical analysis [3] into the sources of microdivergence in ion diodes has identified the competition between two plasma instabilities as a major issue. One instability, the diocotron, leads to rapidly changing electron densities in the virtual cathode, while the other, an ion mode, causes slow fluctuations. The slow fluctuations are thought to be a dominant cause of microdivergence, while the effects of diocotron on a beam ion are lower because they are averaged on many fluctuation periods. Experiments are in progress to test this hypothesis in barrel diode geometry on PBFA-II at Sandia National Laboratories. Experiments will be performed on the SABRE accelerator at Sandia in the extraction diode geometry. As shown in other sections of this report, the microdivergence of the beam leaving the diode is an extremely important parameter in the overall design of LIBRA-LiTE. With no basis in fact, it has been assumed that the microdivergence in LIBRA-LiTE is 4.0 mrad.

Setting aside the issue of microdivergence for the time being, some simple “rules of thumb” are used to design diodes for LIBRA-LiTE. These rules are discussed in detail in the LIBRA [1] report. The following procedure has been used:

- **Choose Anode Current Density.** The anode ion current density should be between 2000 and 5000 A/cm². When the diode power is small, it is often helpful to choose a low current density.
- **Calculate Physical and Dynamic A-K Gap.** The current density is related to the space-charge-limited current density,

$$J_{scl} = 20.6(V^{3/2}/d^2) \text{ A/cm}^2$$

where V is the voltage drop in MV and d is the physical gap in cm. This is the proper expression for a thin electron sheath near the cathode. This is increased by a factor of 5.55 for a uniform electron cloud that fills the A-K gap. Movement of the virtual cathode closer to the anode further increases this enhancement. For a diode operating at 50% of the critical voltage the current density is

$$J_i = 8.5J_{scl}.$$

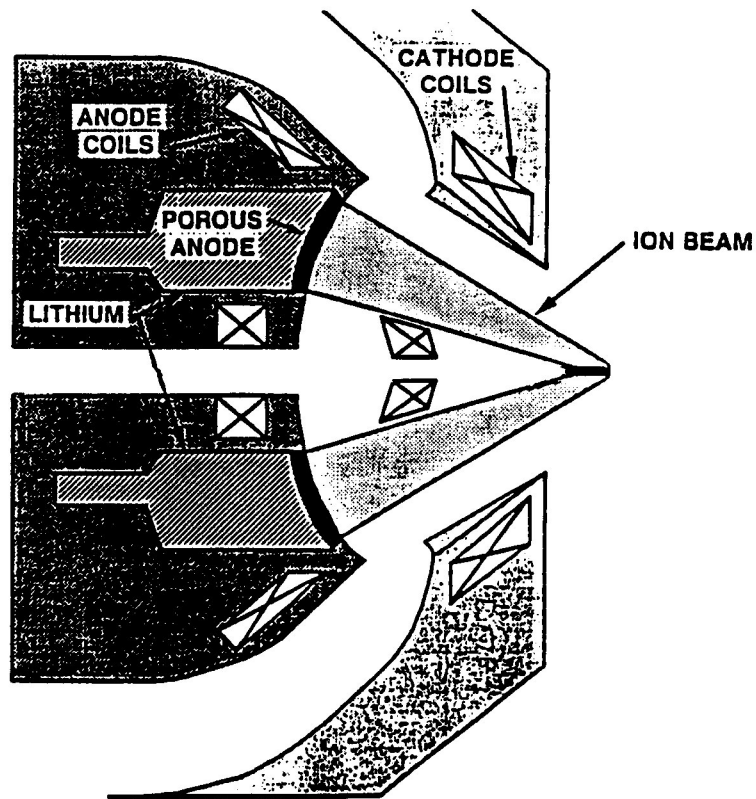


Figure 7.1. Schematic picture of an applied magnetic field light ion extraction diode.

One can then calculate the physical A-K gap, d , from the current density and voltage. The dynamic voltage is the actual distance between the virtual cathode and the ion-emitting surface after the virtual cathode has moved. For an operating voltage 50% of the critical voltage, the dynamic gap is

$$g = 0.81d.$$

- **Anode Dimensions.** To insure proper uniformity of the applied insulating magnetic field, constraints should be made on the anode geometry. The anode is annular and is defined by an outer and inner radius, r_o and r_i . It is demanded that

$$r_o - r_i = 0.2g.$$

The area of the anode is defined by the ion current density and the total current that the diode must provide. These two constraints determine the anode dimensions.

Table 7.1. LIBRA-LiTE Diode Parameters

	Main	Prepulse
Ion energy (MeV)	30	20
Ramped?	Yes	No
Energy into each diode (MJ)	0.469	0.208
Diode efficiency (%)	80	80
Energy out of each diode (MJ)	0.375	0.167
Pulse width (ns)	40	40
Average ion power per diode (TW)	9.38	4.18
Average ion current per diode (MA)	0.313	0.209
Current density (kA/cm ²)	5	5
Physical A-K gap (cm)	2.40	1.77
Dynamic A-K gap (cm)	1.90	1.43
Anode area (cm ²)	62.6	41.8
Anode outer radius (cm)	25.773	23.348
Anode inner radius (cm)	25.385	23.061
Critical magnetic field (T)	4.32	3.94
Applied magnetic field (T)	8.64	7.87

- **Critical Magnetic Field.** The critical applied magnetic field to insure insulation is

$$B_{crit} = 0.34(V^2 + V)^{1/2}/d \text{ tesla.}$$

The applied magnetic field should be twice the critical field.

The rules discussed above are used to determine parameters for the main and prepulse diodes of LIBRA-LiTE. The parameters are listed in Table 7.1. The diodes are assumed to be 80% efficient, which is consistent with PBFA-II experiments. It is also assumed that the ion current density on the anode is 2000 A/cm², which is consistent with light ion diode experiments performed on several facilities. The anode geometry that results from these assumptions is an annulus with a small inner radius. An unanswered question is whether there is enough space in the center of the anode for the necessary magnetic field coils. The diodes will need to shoot at a rate of about 4 Hz, which will be achieved with a liquid lithium anode surface. Just as in LIBRA, it is proposed that the electrohydrodynamic (EHD) effect be used to create the ions.

References

- [1] B. Badger, et al., “LIBRA - A Light Ion Beam Fusion Conceptual Reactor Design,” University of Wisconsin Fusion Technology Institute Report UWFM-800 (February 1990).
- [2] M. P. Desjarlais, “Theory of Applied-B Ion Diodes,” *Physics of Fluids B*, **1**, 1709 (1989).
- [3] M. P. Desjarlais, “The Evolution and Control of Ion Beam Divergence in Ion Diodes,” to appear in *Physics of Fluids B*.

8. Focusing Lenses

A final focus magnetic lens positioned close to the target is required for the ballistic focusing of the driver ions. The position of this lens was determined by the focusing requirements of the ions and permissible radiation lifetime of the front surface of this magnet. Neutronic calculations indicated that if this front surface were composed of ferritic steel its lifetime would be one calendar year at a distance of 2.05 m from the target. At this position a magnetic field strength of 0.6 tesla·m is required with a center bore of 0.18 m. Because the electrical resistivity of any solid conductor in such a magnet would increase rapidly due to radiation damage, and a heat transfer fluid would be needed to remove the neutronic and electrical heating, liquid Li was selected as the conductor and heat transfer fluid for the magnet similar to the design by Steiner [1]. Such a magnet would be a simple one-turn solenoid with a small gap running the length of the magnet, separating the positive and negative electrodes. The final lens design evolved from this concept, as detailed in this report.

8.1. Magnetic Field and Current Requirements

The requirements for the ballistic focusing have to fulfill the condition

$$LB_{ave} = 0.6 \text{ tesla} \cdot \text{m}$$

where L is the length of the magnet and B_{ave} is the average magnetic field strength. The limits imposed on the microdivergence along with the diode dimensions have legislated the design of the magnet. Here are six different configurations (Fig. 8.1):

	I	II	III	IV	V	VI
<u>Magnet dimensions</u>						
Inner radius, r_i (cm)	9	9	9	9	9	9
Outer radius, r_o (cm)	21.8	34.6	21.8	21.8	21.8	21.8
Total length (cm)	30	30	40	50	55	60
Number of turns	5	5	5	5	5	5

The magnetic field, B , due to current in the solenoid along the magnet centerline is

$$B = \mu N I (\cos \psi_1 - \cos \psi_2) / 2L$$

where:

- μ magnetic permeability (vacuum)
- N number of turns
- I current (A)
- L magnet length (m).

Figure 8.2 shows the variation of the magnetic field along the magnet centerline for configuration IV. Liquid lithium is the conductor in a five turn coil. The parameters for the different configurations are as follows:

	I	II	III	IV	V	VI
Average field at centerline (tesla)	2.0	2.0	1.5	1.2	1.091	1.0
Current, I (MA)	0.159	0.187	0.139	0.129	0.126	0.123
Current density, J (MA/m ²)	20.68	12.2	13.59	10.11	8.935	8.021
E.M.F. (volts)	32.85	26.75	21.6	16.05	14.2	12.75
Power (MWe/magnet)	5.22	5.01	3.0	2.078	1.788	1.567

The power consumed in the coil does not change with the number of turns for the same magnetic field, while the power consumed in the transmission lines and the magnet leads is proportional to I^2 ; therefore current optimization is required. As one can notice from Fig. 8.3 the required current is inversely proportional to the length of the magnet. However, increasing the length will affect the distance between the magnet face and the target which will effectively disturb the value of the microdivergence. A magnet length of 0.5 m has been chosen to fulfill all the restrictions.

8.2. MHD and Thermal Hydraulics Aspects of Final Focus Magnetic Lens

8.2.1. Introduction

It has long been known that a magnetic field affects the fluid mechanics of a liquid metal [2, 3] by inducing an electric current in it perpendicular to both the magnetic field and the fluid motion. This current is the source of a retarding force that gives rise to MHD effects:

First: Turbulent eddies are damped by the induced magnetic force that opposes their motion and the average velocity gradient near the wall is reduced by the magnetic field. This causes the heat transfer coefficient to be substantially degraded.

Second: The flow is retarded by the ponderomotive force that acts on the bulk of the fluid causing a higher pressure drop.

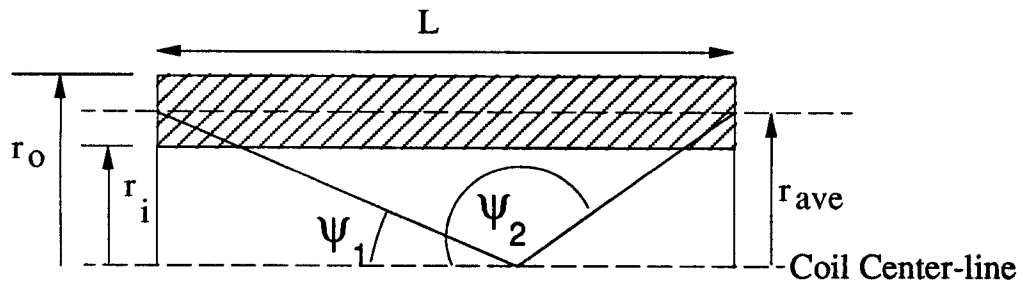


Figure 8.1. Geometry of an axial section in a solenoid.

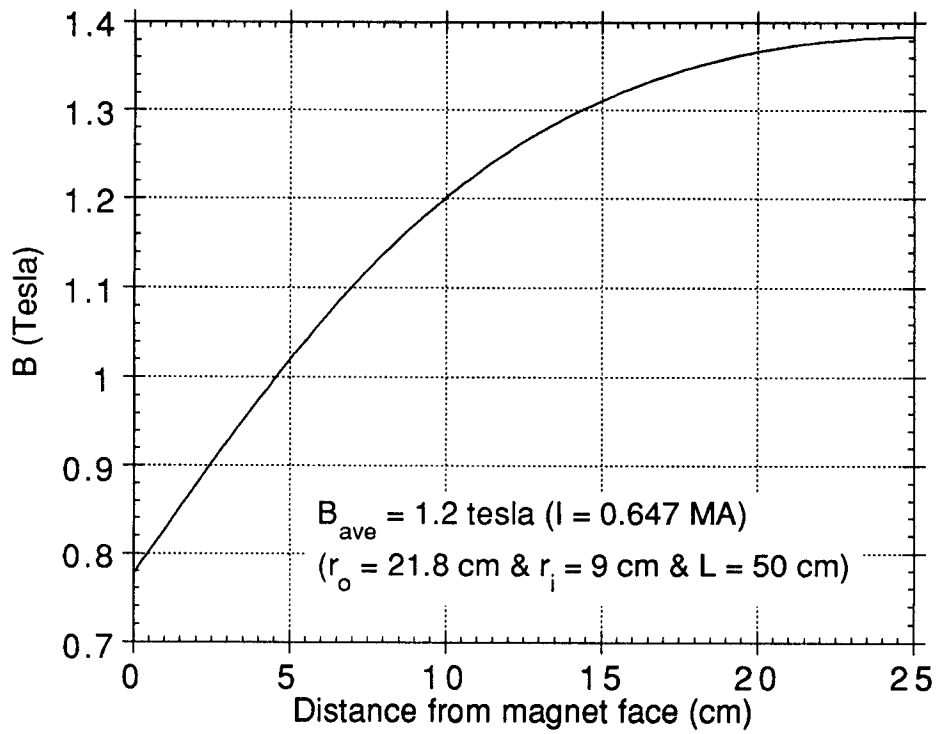


Figure 8.2. Magnetic field distribution for configuration IV for a one turn coil.

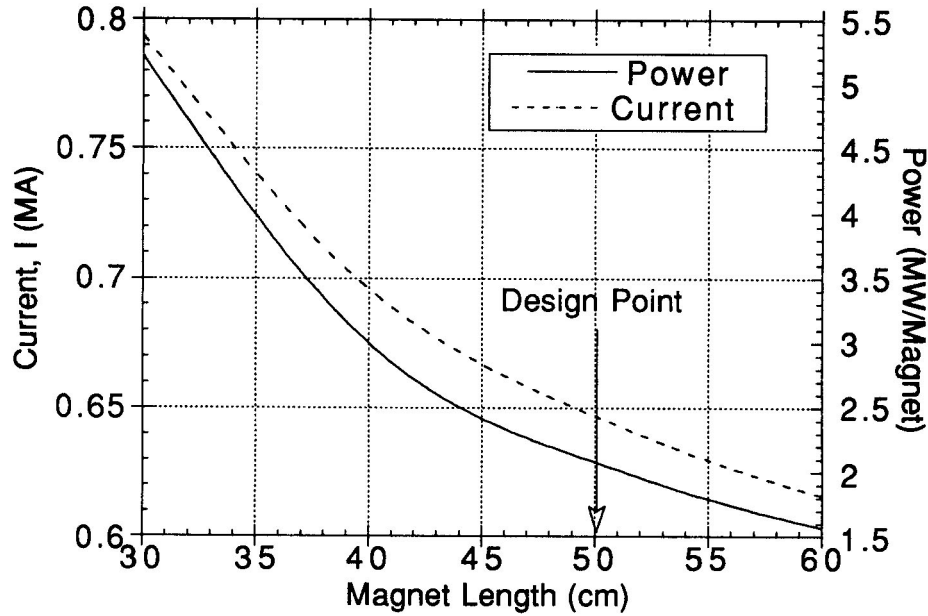


Figure 8.3. Electric power dissipation and current variations with the length of the magnet for the condition: $LB_{ave} = 0.6$ tesla \cdot m.

These MHD effects have a great influence on the general performance of the final focus magnetic lens. Magnetic pressure drop, viscous effects, thermal stresses, primary stresses and heat transfer are all coupled, which makes setting the design point such a challenging process.

8.2.2. Remarks on the thermal problem for laminar MHD channel flow of a liquid metal

The transition from laminar to turbulent flow

The critical Reynolds number, Re_{cr} , increases significantly with an increase in the Hartmann number (for $Ha > 20$) [4]. The general criterion for the transition from laminar to turbulent flow in a rectangular or circular duct can be written as $\{Re_{cr} = \text{constant}Ha\}$. It can be assumed quite reliably that the flow in any rectangular or circular duct will be laminar at $Re_{cr} < 130Ha$, while at $Re_{cr} > 215Ha$ it will be turbulent [5]. All these estimates are valid only for high Ha . In practice estimates for $Ha_R > 10$ are used, where Ha_R is the Hartmann number based on the hydraulic radius of the duct cross section. For rectangular cross sectional ducts, the most general empirical formula for the critical Reynolds number (Re_{cr}) corresponding to

laminar-turbulent transition in the presence of a transverse magnetic field is [6]:

$$Re_{cr} = Ha(215 - 85e^{-0.35b/a})$$

where:

b/a	flow channel aspect ratio ($2a$ is the channel dimension in the direction of the applied magnetic field)
Ha	Hartmann number
Ha^2	$d^2 B^2 \sigma/\mu$
Re	$\rho ud/\mu =$ Reynolds number
N	interaction parameter (Stuart number) $= Ha^2/Re$
d	channel width (meters) $= 2a$
B	magnetic field strength (tesla)
u	average fluid velocity (m/s)
σ	electrical conductivity (1/ohm-m)
μ	fluid viscosity (newton-s/m ²)
ρ	fluid density (kg/m ³)

For liquid lithium (in SI units), at 400°C and $B = 2$ tesla with u (m/s) and d (m) remaining as free parameters, the results indicate:

$$\begin{aligned} Re &= 1.33 \times 10^6 ud \\ Ha &= 1.85 \times 10^5 d \\ N &= 2.57 \times 10^4 d/u. \end{aligned}$$

The criteria for full laminarization, $Re \leq 125Ha$, leads to $u \leq 17.4$ m/s. In practice this kind of a speed is very large; the liquid lithium flow would then be laminar most of the time.

Entry length effects

It is assumed that both the velocity and the temperature profile are initially flat upon entering the channel. It is proposed that the flow remains turbulent over a large part of the stabilization length, becoming fully laminarized only at the end of this length. The hydraulic entrance length is [5] about $2d/N^{1/2}$ which means a very short stabilization length (in the range of 2 mm). For the thermal entrance length, x_t , the case is completely different, $x_t \leq 0.05 d Re Pr$, where

$$Pr \text{ (Prandtl number)} = 0.033 \text{ for Li at } 400^\circ\text{C} \text{ .}$$

For the thermal entrance length $x_t \leq 2.2 \times 10^3 ud$ (m) and for typical values of $u = 1.0$ m/s and $d = 0.01$ m, the value for the thermal entrance length is $x_t \leq 0.22$ m. For comparison, the average length of the total path of liquid lithium is 1.0 m. The thermal entrance length is 22%

of the total flow path. In this thermal entrance distance the value of the heat transfer coefficient decreases [7] monotonically to about 1/10 of its initial value upon entering the channel.

Heat transfer

Heat transfer is of paramount importance when operating the majority of engineering devices employing liquid metals. Moreover, frequently a knowledge of the hydrodynamic properties is needed mainly in order to calculate the attendant thermal phenomena. The relation describing the heat transfer during steady plane-parallel flow in a transverse magnetic field differs from the corresponding relation for flow without a field only by a term that accounts for ohmic heating (Joule-heat generation). This term should be taken into account for liquid metals, especially if a large electrical current flows through the liquid metal or if the channel walls are conducting and the induced currents in the liquid metal are large. Although heat dissipation by viscous forces can frequently be neglected, at high Hartmann number this is not the case; the viscous and Joule dissipations are of the same order of magnitude. The magnetic field modifies the heat-transfer process by changing the velocity profile. Increasing the velocity gradient near the wall results in a higher heat transfer rate. Appropriate calculations show that heat transfer in a liquid metal (fluids with low Prandtl numbers), flowing at a moderate Hartmann number in a transverse magnetic field, can increase significantly, in comparison with the case of no magnetic field. However, as the Hartmann number increases further, the rise in the heat-transfer rate becomes more moderate and reaches a constant value [8]. Hoffman [9] suggested that for laminar flow, the Nusselt number for fully-developed flows of liquid metal between parallel plates for a constant wall heat flux can be taken as high as 12 (based on the channel hydraulic diameter); $Nu = h D/k$ where

Nu	Nusselt number
h	heat transfer coefficient
D	channel hydraulic diameter
k	fluid thermal conductivity.

If the entrance effect on the laminar flow heat transfer coefficient is neglected, the relationship between h and D is illustrated in Fig. 8.4.

Thermal hydraulics calculations

Neutronics analysis is performed utilizing a one-dimensional model to calculate the distribution of the volumetric nuclear heating in the magnet. Also, a one-dimensional hydrodynamics calculations is executed to determine the cavity performance and to account for the effects of vaporization/condensation processes on the surface heat flux. The following is a steady state parameter list:

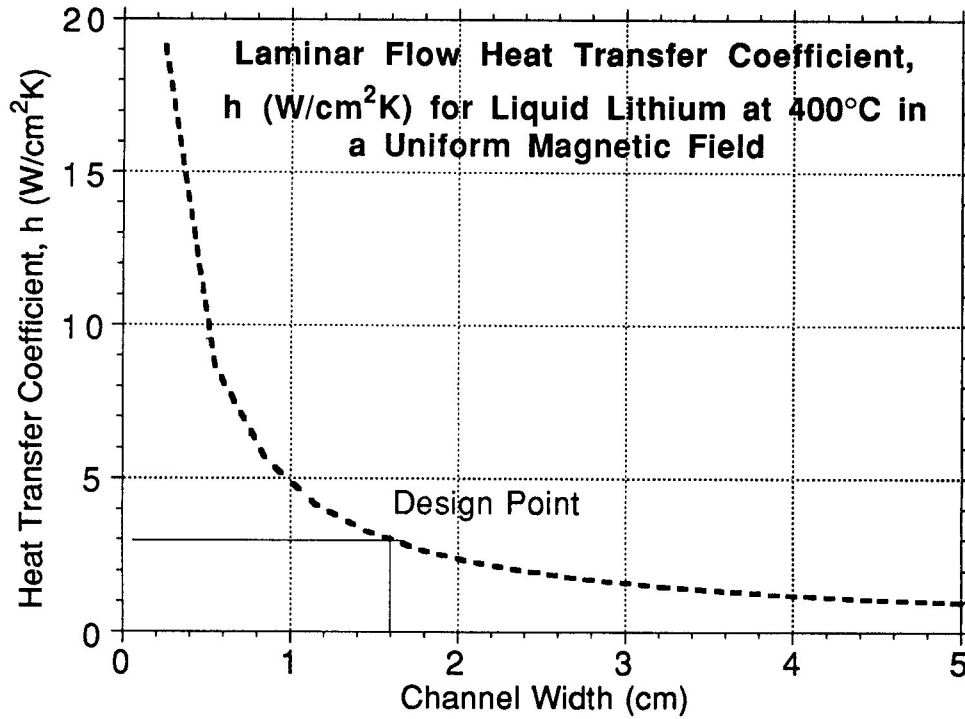


Figure 8.4. Laminar flow heat transfer coefficient for liquid lithium at 400°C in a uniform magnetic field.

Peak nuclear volumetric heating in front metal (W/cm ³)	184
Peak nuclear volumetric heating in front Li (W/cm ³)	85
Total nuclear volumetric heating/magnet (MW)	3.72 .

Moreover, when the ohmic heating is taken into account in the calculation of the thermal hydraulics performance of the magnet, the total heating in the magnet is about 5.87 MW. Consider the following thermal assumptions:

Inlet coolant temperature	275°C
Outlet temperature	525°C
Coolant temperature rise	250°C
Average coolant temperature	400°C .

By using these parameters the following results are obtained for the five turn magnet:

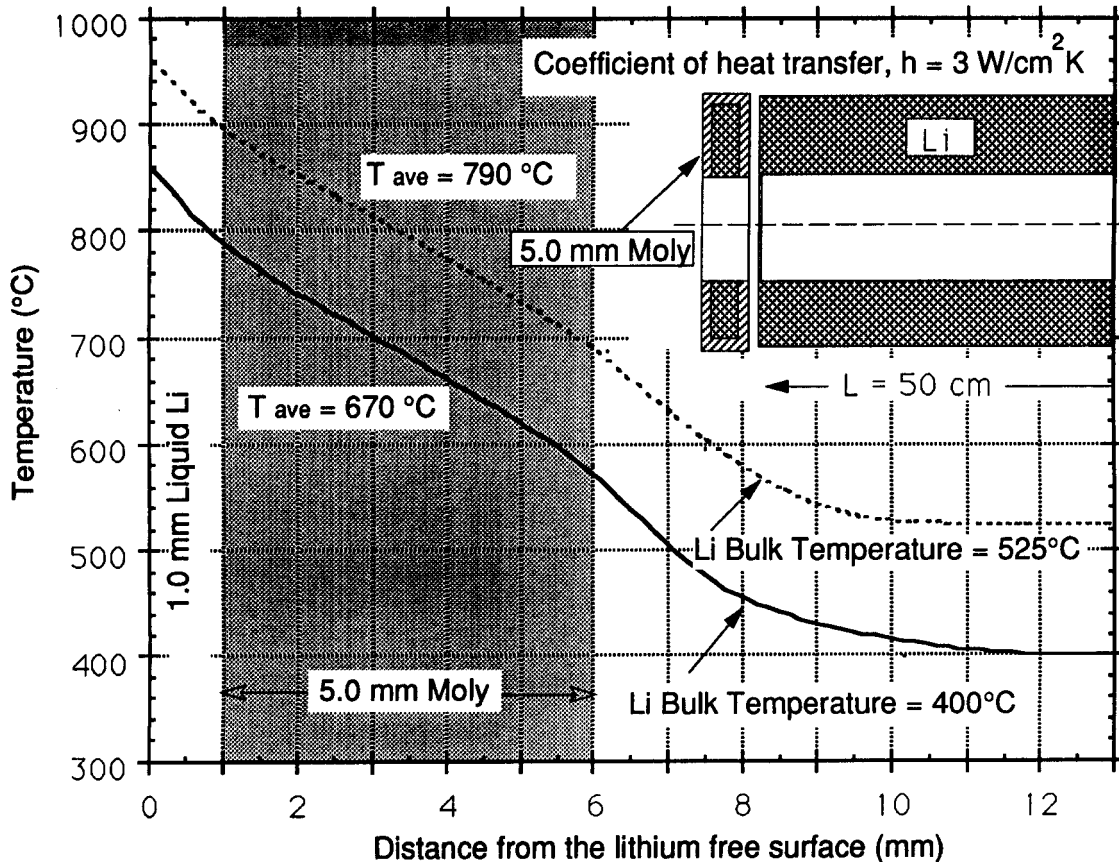


Figure 8.5. The temperature distribution in the first wall.

Average coolant velocity (m/s)	0.83
Volumetric flow rate/magnet (m ³ /s)	1.06×10^{-2}
Total volumetric flow rate in 30 magnets (m ³ /s)	0.32 .

The first wall has no ohmic heating because there is no current in the lithium. The total heating in the first wall including surface heating, volumetric nuclear heating and volumetric ohmic heating is about 0.71 MW/magnet. The same assumptions of the temperature that are applied in the previous case of the magnet are applied here too. The following parameters are applied to the first wall:

Average coolant velocity (m/s)	0.66
Volumetric flow rate/magnet (m ³ /s)	1.35×10^{-3}
Total volumetric flow rate in 30 magnets (m ³ /s)	0.04 .

That makes the total volumetric flow rate in the 30 magnets 0.36 m³/s. A two-dimensional thermal model of the first wall is used with ANSYS to calculate the temperature distribution

in the first wall. ANSYS is a commercial computer code capable of handling thermal and stress analysis applications using the finite-element method [10]. Two cases of the calculated temperature distribution in the first wall are shown in Fig. 8.5. The first case is for the coolant at the average temperature of 400°C, while the second case is for the coolant at the maximum temperature of 525°C. The value used for the heat transfer coefficient in both cases is 3.0 W/cm² K. This corresponds to a channel width of 16.0 mm as seen from Fig. 8.4. The most suitable material for the first wall that can operate in this environment at this elevated temperature has been chosen to be TZM. The following is a summary of the results:

<u>Case</u>	<u>First</u>	<u>Second</u>
Liquid lithium temperature (°C)	400	525
Maximum temperature of TZM (°C)	780	885
Minimum temperature of TZM (°C)	580	795
Average temperature of TZM (°C)	670	790

8.3. Magnetic Pressure and MHD-Induced Pressure Drop

It has long been known that in a current-carrying flow the pressure increases at the axis of cylindrical liquid conductors as a result of compression by the electromagnetic pinch force due to the interaction of the electric current and its self-magnetic field [11]. For homogeneous boundary conditions an electromagnetic force $f_e = J \times B$ can drive a fluid motion. The approximate estimate for the magnetic pressure generated within the fluid for a solenoid is $B^2/2\mu$. The MHD-induced pressure drop, Δp , is

$$\Delta p = \sigma_w t_w u B^2 L/a$$

where:

B	magnetic field strength (tesla)
u	average fluid velocity (m/s)
σ_w	wall electrical conductivity (1/ohm-m)
t_w	wall thickness normal to the field (m)
a	channel half-width in direction of the field (m)
L	fluid path length (m) .

To minimize the MHD-induced pressure drop, t_w must be minimized. A sandwich construction is proposed. The sandwich duct wall is a layered construction in which the metallic layer adjacent to the lithium is as thin as feasible and is electrically isolated from a much thicker metal structural wall. The metal layer facing the liquid lithium is assumed to be thin; it essentially provides no resistance to pressure stresses, and the burden of the internal pressure

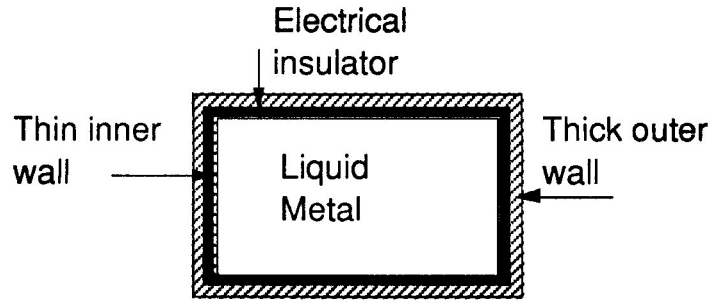


Figure 8.6. Sandwich construction.

is supported by a thick structural wall outside the insulator. In this design the following is assumed:

1. A thin inner HT-9 wall of 1 mm thickness.
2. A thin electrical insulator, $\text{MgO}\cdot\text{Al}_2\text{O}_3$; spinel of 0.5 mm thickness.
3. A thick outer HT-9 wall of some thickness (to be determined from the stress analysis).

Figure 8.7 shows the magnetic pressure and the MHD-induced pressure drop variation along the entire length of the magnet. The maximum pressure of 0.82 MPa is at the inlet of the liquid lithium coolant. In this study the viscous forces are small and are neglected. It is of interest to note that a high pressure must be provided to overcome the magnetic pressure hill through the first half-length of the magnet; on the contrary, energy dissipators should be provided in the second half-length of the magnet to avoid a strong lithium jet at the exit. The MHD-induced pressure drop, Δp_{FW} , in the first wall is:

$$\Delta p_{FW} = 0.197t_w \text{ (in mm) MPa.}$$

8.4. Mechanical Analysis

For the current design, the casing which contains the helical magnet system can be characterized as two concentric cylindrical shells with annular end plates. No structural credit is given to the helical conduit or insulation. Sectioned views of the casing are shown in Fig. 8.8. The primary loading is internal pressure. In the analysis, the magnitude was prescribed to be 1.0 MPa. Since stresses and deflections are linear functions of pressure, this facilitates

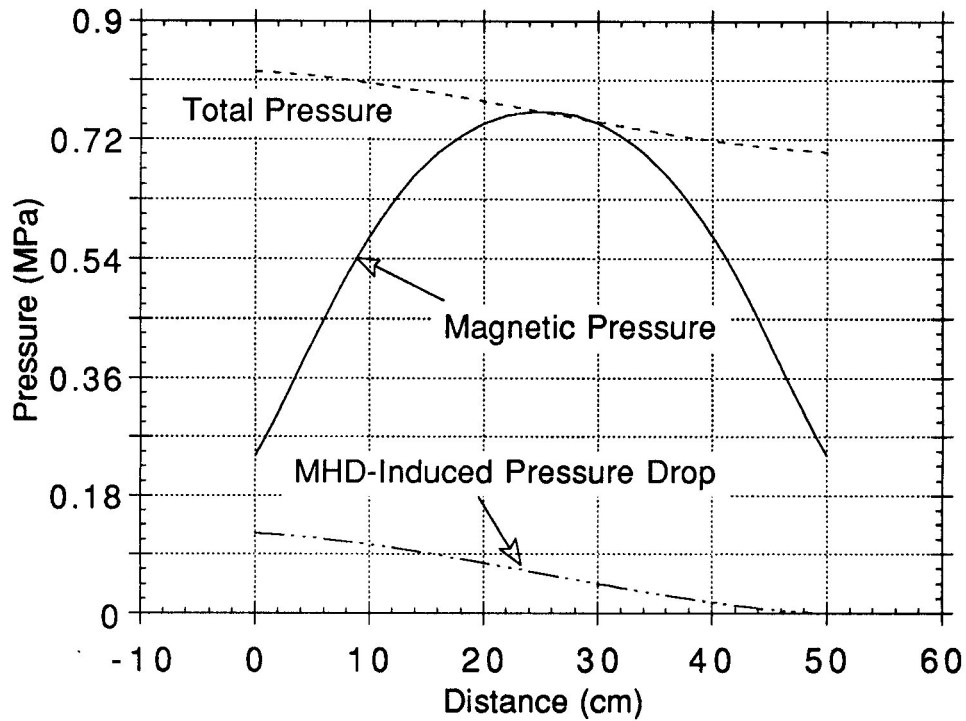


Figure 8.7. Magnetic pressure and total pressure variations across the length of the magnet.

direct scaling. The casing is HT-9 with an elastic modulus and Poisson's ratio of 180 GPa and 0.27, respectively, at 550°C [12]. The model was analyzed both by classical methods and the finite element software ANSYS with good agreement. Flexural and stretching effects were included. The particular design data presented used the fixed dimensions of Fig. 8.8 with the wall thickness of the two shells and end plates each equal to 1.0 cm. Stresses are described in terms of equivalent Von Mises values, i.e., $[(\sigma_1 - \sigma_2)^2 + (\sigma_2 - \sigma_3)^2 + (\sigma_3 - \sigma_1)^2]^{1/2}/\sqrt{2}$, where σ_1 , σ_2 and σ_3 are the principal stresses. A design based upon this will be the same as using the maximum octahedral stress or maximum energy of distortion criteria. The recommended allowable stress for HT-9 at 550°C and 150 dpa is 115 MPa [12]. This is the uniaxial (principal) stress with which the multidimensional equivalent stress is compared. Results for a pressure of 1 MPa are shown in Fig. 8.9. Maximum stress occurs near the center face of the annular end plate, 36.69 MPa, but comparable amplitudes of 34.65 MPa and 34.06 MPa develop in the larger and smaller shells, respectively, where they join the end plate. The maximum outward radial displacement of the larger shell is 23.0 μm while the inward radial displacement of the smaller shell is 5.2 μm . The maximum axial bulge in the end plate is 44.9 μm . The actual pressure is estimated to be 0.82 MPa (Fig. 8.7). With a scaling factor of 82%, results for maximum plate

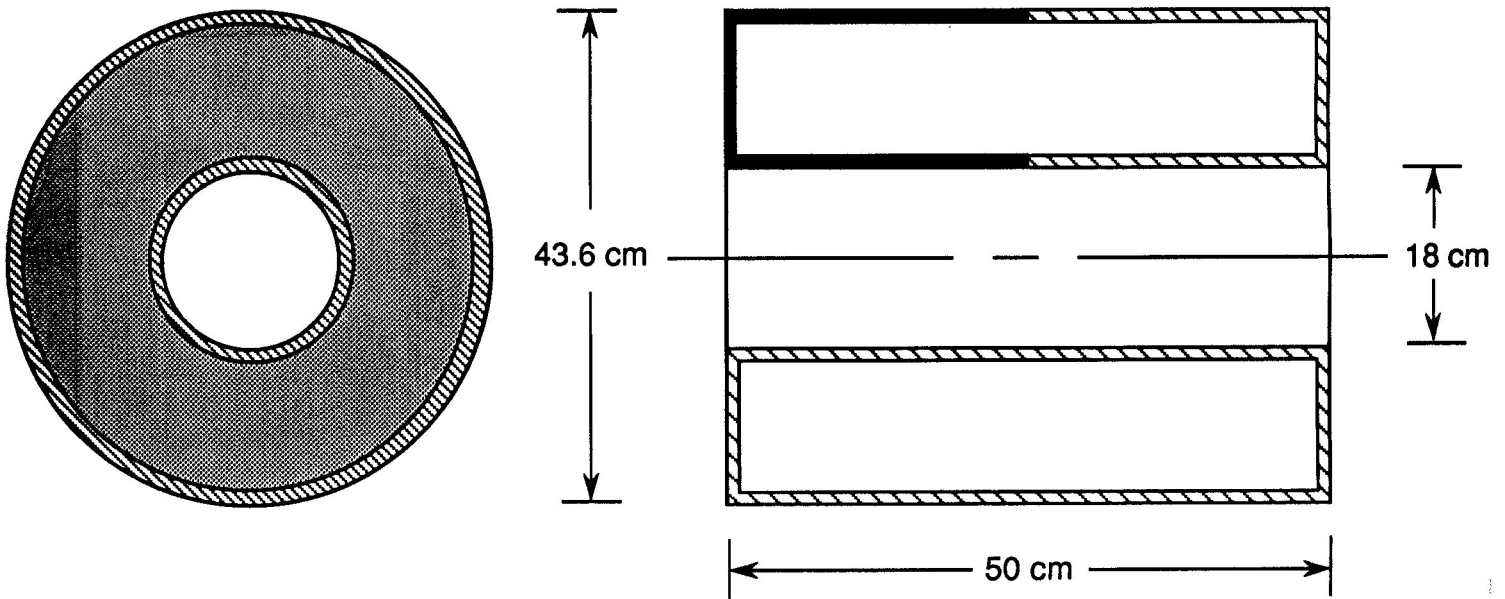


Figure 8.8. Sectioned views of final focus magnet casing. Solid shaded quarter is used to show finite element results in Fig. 8.9.

and shell stresses become 30.09 and 28.41 MPa, significantly below the given design limit. The scaled radial expansion of the outer shell is $18.9 \mu\text{m}$ while the radial contraction of the inner shell is $4.3 \mu\text{m}$.

The thickness of individual or all components could be reduced and still have maximum stresses adequately below design limits; however, this would result in larger displacements which are not desirable. Thus a 1.0 cm thick wall is considered to be a practical design specification for the magnet casing.

8.5. Conceptual Design of the Final Focus Magnetic Lens

Three views of the final focus magnetic lens are shown in Fig. 8.10, 8.11, 8.12.

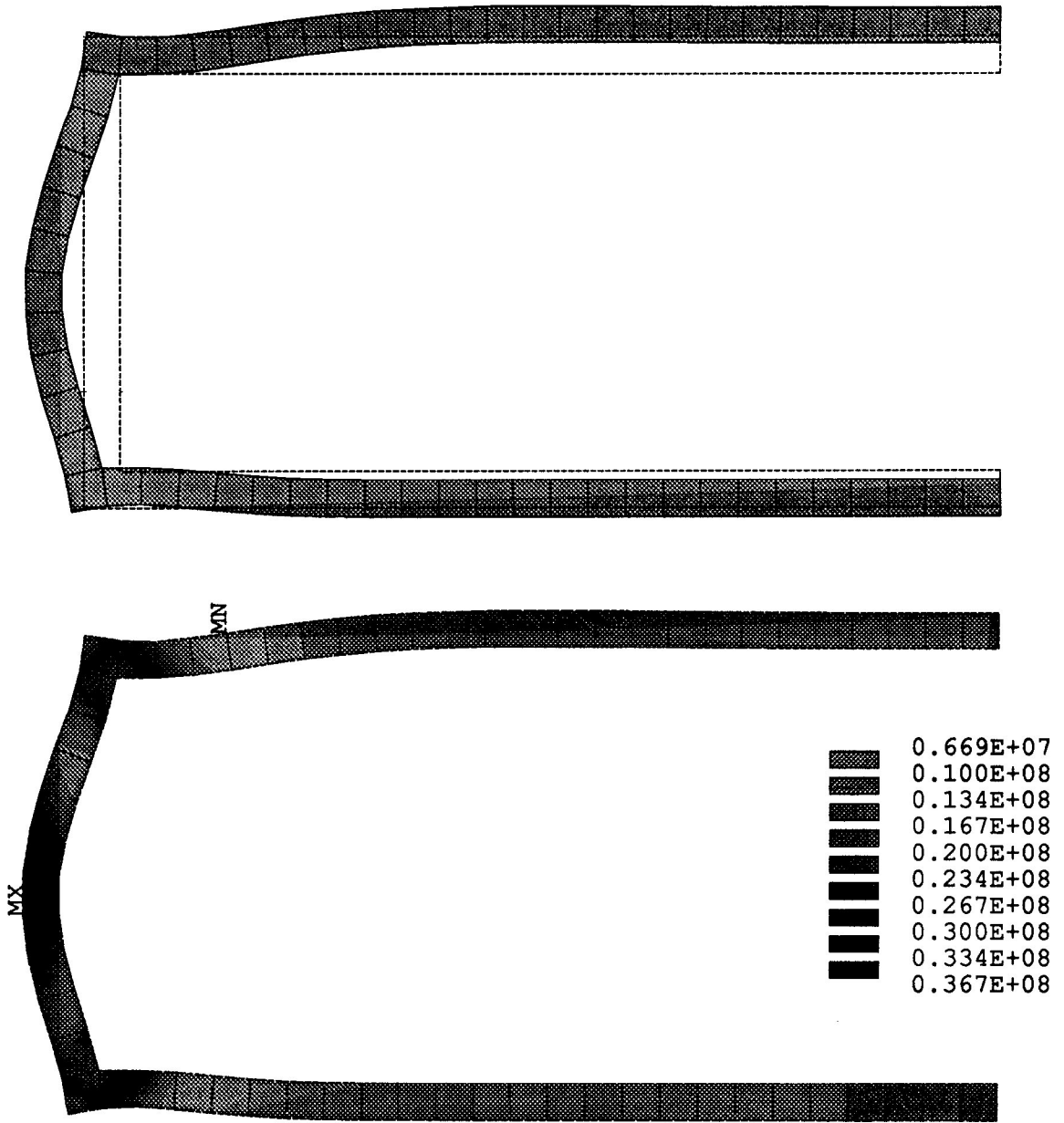


Figure 8.9. Finite element deflections and stresses for quarter section (axisymmetric) of final focus magnet casing. Pressure is 1 MPa, thickness is 1 cm and material is HT-9.

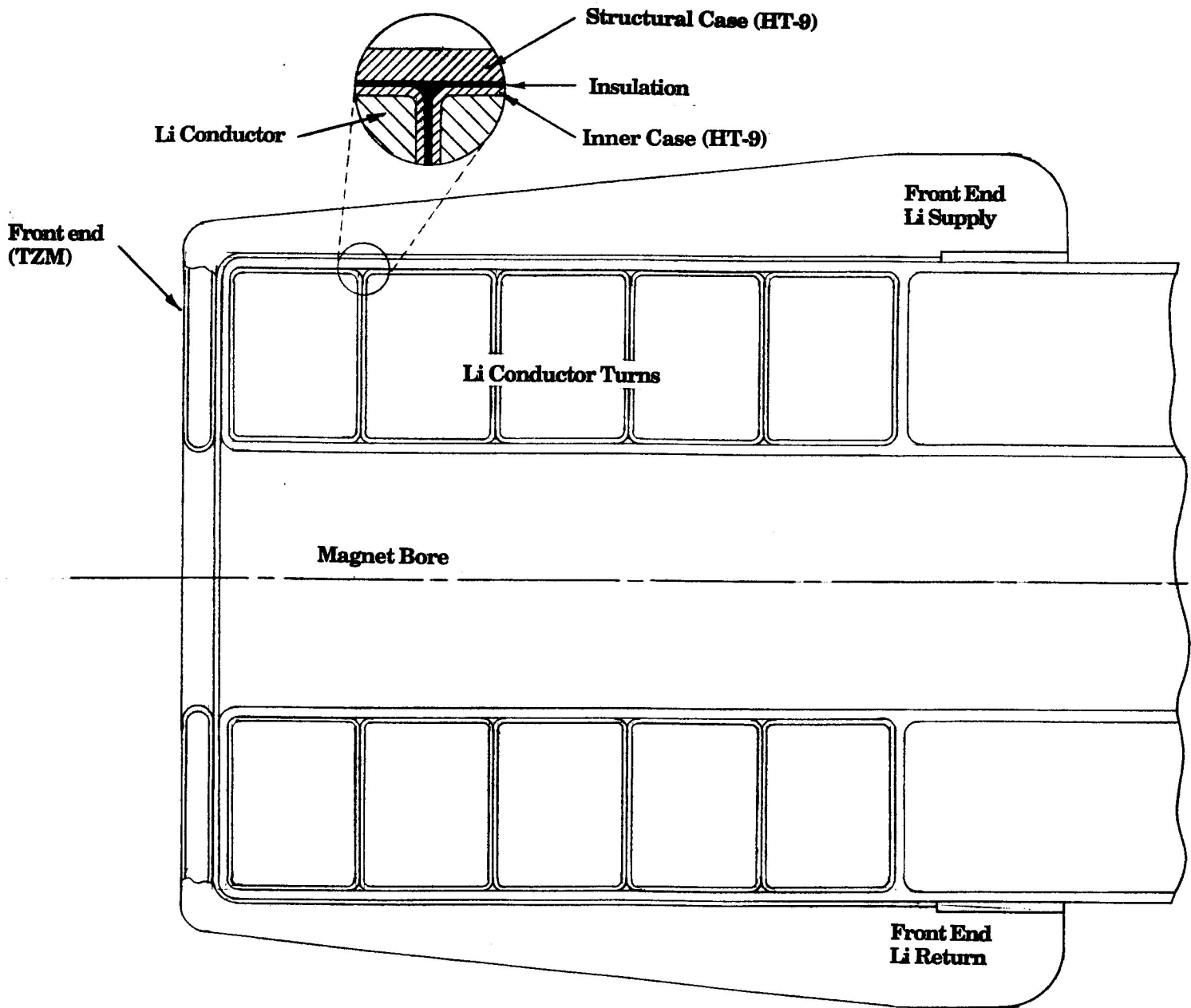


Figure 8.10. Cross-section of the final focusing magnet.

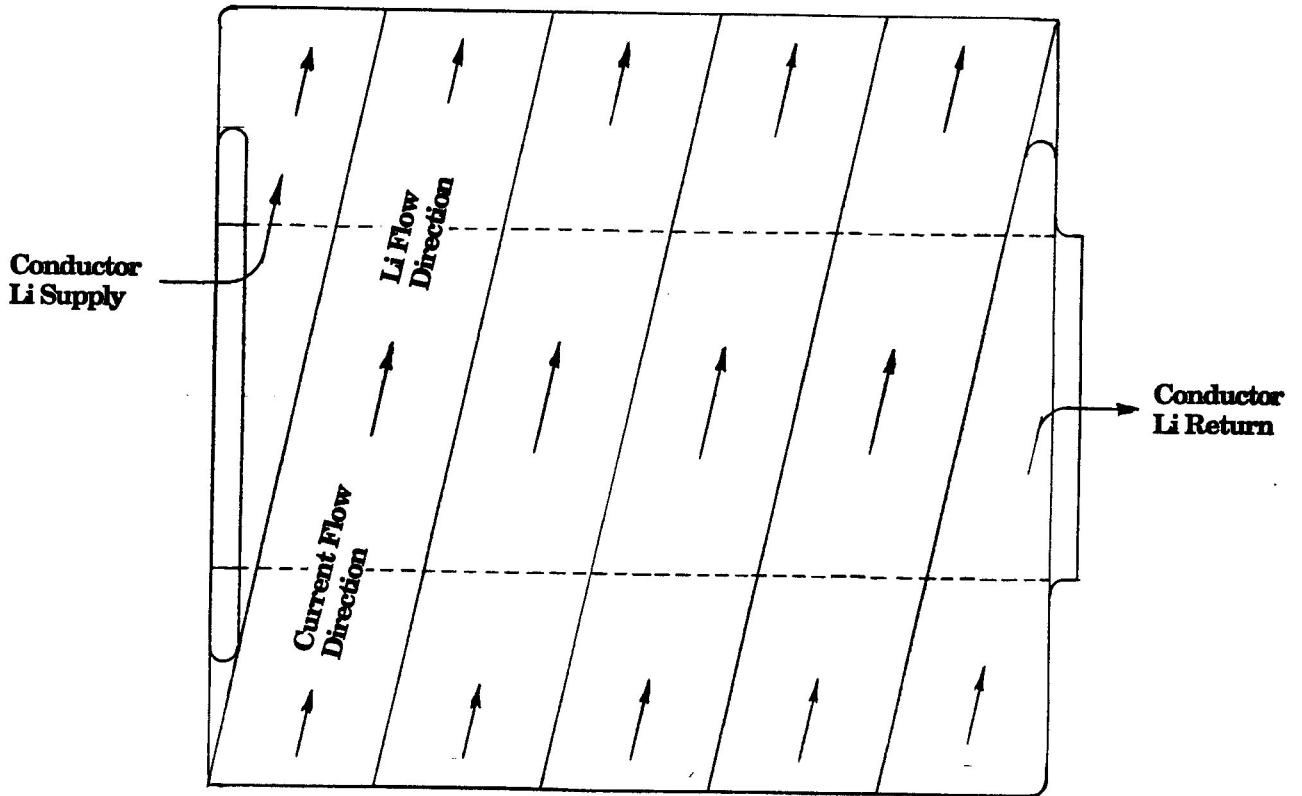


Figure 8.11. Top view of the inner magnet case.

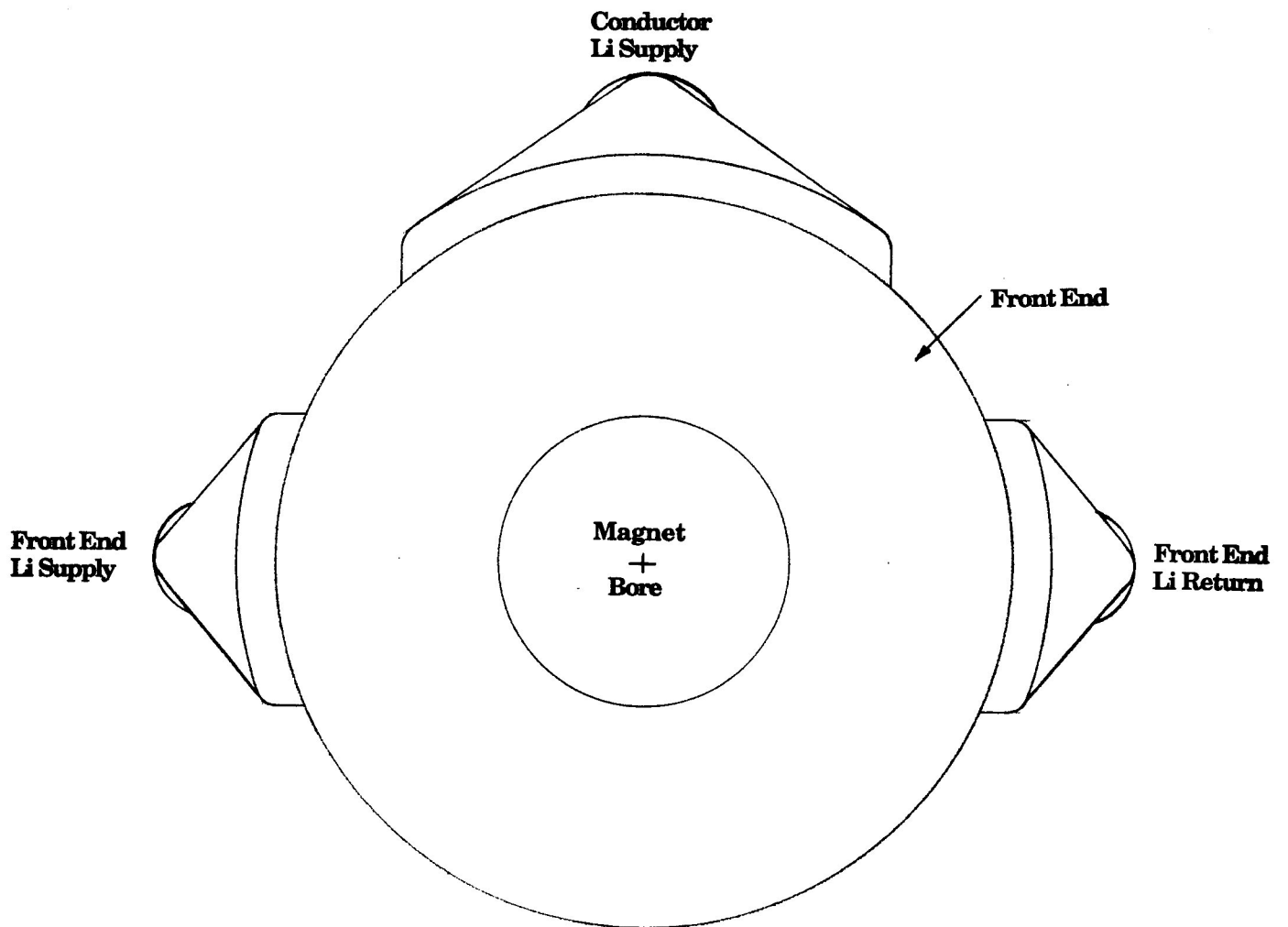


Figure 8.12. Front view of the final focusing magnet.

References

- [1] D. C. Steiner, R. C. Block and B. K. Malaviya, "The Integral-Blanket-Coil Concept Applied to the Poloidal Blanket System for a Tokamak Reactor," *Fusion Tech.*, **7**, 66 (1985).
- [2] R. A. Gardner and P. S. Lykoudis, "Magneto-Fluid-Mechanics Pipe Flow in Transverse Magnetic Field: Part 2, Heat Transfer," *J. Fluid Mech.*, **48**, 129 (1971).
- [3] R. A. Gardner, K. L. Uherka, and P. S. Lykoudis, "Influence of a Transverse Magnetic Field on Forced Convection Liquid Metal Heat Transfer," *AIAA Journal* *4*, **5:848** (1966).
- [4] R. C. Lock, "Stability of the Flow of an Electrically Conducting Fluid Between Parallel Planes Under Transverse Magnetic Field," *Proc. Roy. Soc. A*, 233:105 (1955).
- [5] H. H. Branover, "Magnetohydrodynamic Flow in Ducts," John Wiley & Sons, New York, and Israel University Press, Jerusalem (1978).
- [6] H. H. Branover, "Suppression of Turbulence in Pipes with Transverse and Longitudinal Magnetic Fields." *Magnetohydrodynamics*, **47**, 107 (1967).
- [7] M. Perlmutter and R. Siegel, "Heat Transfer to an Electrically Conducting Fluid Flowing in a Channel with a Transverse Magnetic Field," NASA Techn. Notes D875, 1961.
- [8] R. A. Gardner, "Laminar Pipe Flow in a Transverse Magnetic Field with Heat Transfer," *Int. J. Heat Mass Transfer*, **11**, 1076-1081 (1968).
- [9] M. A. Hoffman, "Magnetic Field Effects on the Heat Transfer of Potential Fusion Reactor Coolants," Lawrence Livermore National Laboratory, UCRL-73993 (1972).
- [10] Gabriel J. DeSalvo and Robert W. Gorman, "ANSYS Engineering Analysis System Users Manual," Revision 4.4, Swanson Analysis Systems, Inc., May 1989.
- [11] Ed. V. Scherbinin, "Electrically Induced Vortical Flows," *Liquid Metal Magnetohydrodynamics*, J. Lielpeteris and R. Moreau (editors), Kluwer Academic Publishers, pp. 169-178 (1989).
- [12] D. L. Smith and G. D. Morgan, "Blanket Comparison and Selection Study," Final Report, Argonne National Laboratory, ANL/FPP-84-1 (1984), Vol. 2, Chapter 6.1.

9. Ion Propagation

The ballistic focusing mode is a critical aspect of the LIBRA-LiTE study. The focusing system is depicted in Fig. 9.1. The ion beams are generated in the diodes, as described in Chapter 7. The ions propagate out of the diodes to the focusing lens magnets in hollow conical beams. The width of the conical shell to which the beams are confined thickens during transport due to scattering of beam ions by the background gas and due to microdivergence. Microdivergence is determined in the diode. Microdivergence growth due to possible plasma instability growth is neglected during transport. The beam radius, which is decreasing due to focusing by the diode, increases due to this spreading. The diode is designed so that the beam would reach a broad focus beyond the focusing lens magnet and target. The bore radius of the focusing lens magnet must be large enough to contain the converging beam. The beams are focused onto the target by the lens magnets. The focal spot size, which must be no larger than the target, is affected by microdivergence and scattering during transport between the magnets and the target.

The focusing lens magnets are designed to focus cylindrical ion beams to a target. The magnet operates by using B_r fields that exist near the ends of the solenoid to convert some of the axial ion beam velocity, v_z , into azimuthal velocity, v_θ . The axial magnetic field then acts against the v_θ to give the ions a focusing force and a radial velocity, v_r . As the ions move out of the solenoid, they once again encounter a B_r , but in the opposite direction, which removes the azimuthal motion. Conservation of canonical angular momentum requires that the ion beam has the same angular momentum on both sides of the magnet, which is assumed to be zero. In the presence of the magnetic field, the canonical angular momentum is $m\vec{v} + q\vec{A}/c$. In a solenoid, \vec{A} is azimuthal, so \vec{v} has an azimuthal component in the opposite direction while there is a finite vector potential, \vec{A} . It is important that the ion beam has no angular momentum at the target, or it will not focus to a spot.

The SCATBALL code is used to study the transport of ions from the diodes, through the focusing magnets to the target. This code calculates the envelope for the ion beam. This includes the effects of scattering by the background gas, spreading from microdivergence, focusing by the lens magnets and time-of-flight bunching of the ion beam. These properties are all calculated using analytic formulas [1]. In addition, the heating of the background gas by the ions is calculated numerically. This is a non-linear problem because the heating rate is strongly affected by the temperature of the background gas. Therefore no analytic solution is known and numerical methods must be used.

SCATBALL has been used to study the effects of microdivergence on the transport parameters. The microdivergence caused by the diodes is one of the greatest uncertainties in

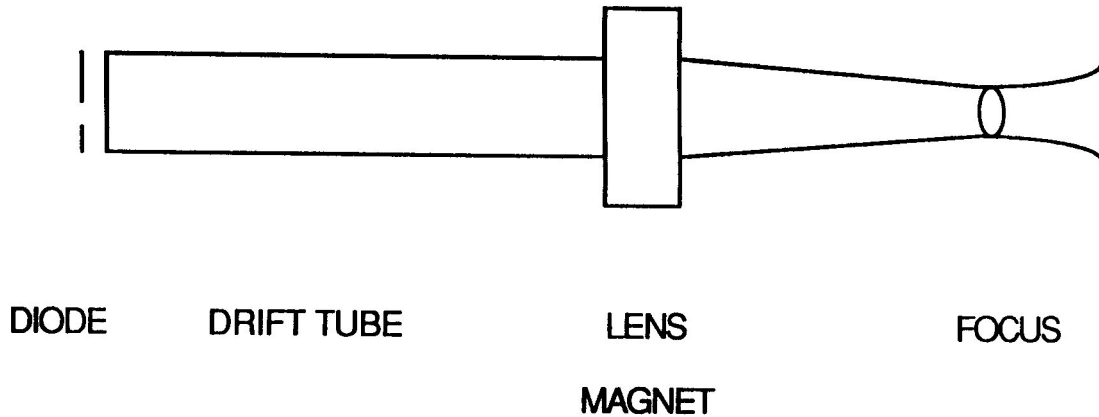


Figure 9.1. Schematic picture of ballistic ion transport system.

light ion fusion. It is believed that light ion fusion with ballistic focusing will not be credible for microdivergences greater than about 6 mrad. This is demonstrated by using the SCATBALL code to calculate the required energy on target in the main pulse to obtain 127 TW/cm^2 with a 11.8 bunching factor. This is the bunching factor chosen for LIBRA-LiTE and is slightly more than the achievable bunching predicted for the pulse power system designed for LIBRA [1]. A bunching factor greater than 11.8 is not felt to be credible. This value is chosen to minimize the required energy on target. If the distance between the target and the center of the magnets is chosen to be 230 cm, the plot shown in Fig. 9.2 is obtained. Here, the energy on target in the main pulse is plotted against microdivergence. Based on this, 4 mrad is chosen for the microdivergence, which provides 127 TW/cm^2 in the 3.4 ns main pulse containing 5.4 MJ on a 1 cm radius target. This is far below the microdivergences currently achieved on PBFA-II. The near term microdivergence goals are approximately 15 mrad on PBFA-II with lithium. Also studied is the variance of the distance between the first surface of the focusing lens magnets and the target with microdivergence if one keeps the same target parameters and 5.4 MJ in the main pulse. This is shown in Fig. 9.3 along with the neutron damage rate on the surface of the 50 cm long magnets for a 1027 MWe power plant versus microdivergence. The magnets are 50 cm long and the focal length is measured from the center of the magnet.

The heating of the target chamber gas by the ion beams has been considered. It is thought that filamentation instabilities can be avoided if the electrical conductivity of the gas is greater than 10^{14} s^{-1} . The SCATBALL code has been used to calculate the conductivity of the gas. The gas is heated by ion beam energy deposition. As the background gas temperature increases, the gas ionizes and the conductivity increases. Electron collisions dominate the conductivity, so electron temperature increases lead to higher conductivity. The conductivity

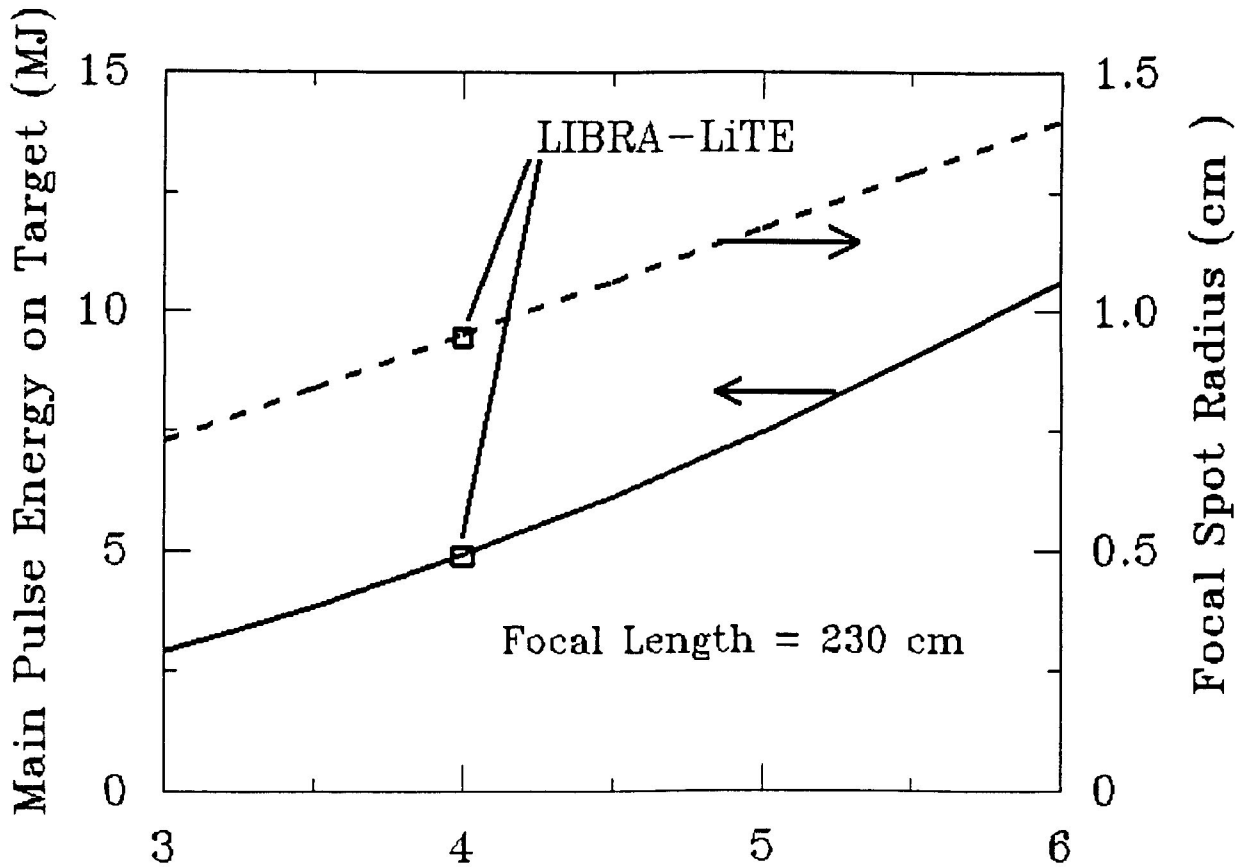


Figure 9.2. Energy on target in main pulse versus microdivergence.

at the head of each beam is very low. Therefore the leading edge of the beam is subject to the instability. The breakdown process in the head of the beam is very complicated because the low conductivity and the large time rate of change of the current density allow large electromagnetic fields to be generated. These fields are thought to initiate electron avalanche. This process is not considered in SCATBALL. After the avalanche breakdown is complete, the conductivity is still below the required value but ion beam heating and ohmic heating by the return current continues. This is included in SCATBALL. SCATBALL has been used to calculate the conductivity in the background gas at the lens magnet. The calculation assumes the transport parameters given in Table 9.1. The conductivity at the lens magnet for a main pulse beam at the tail end of the beam is $1.59 \times 10^{14} \text{ s}^{-1}$.

The design parameters for the ion transport system are shown in Table 9.1. A background gas of $3.55 \times 10^{16} \text{ cm}^{-3}$ of helium is assumed to be present throughout the entire beam transport

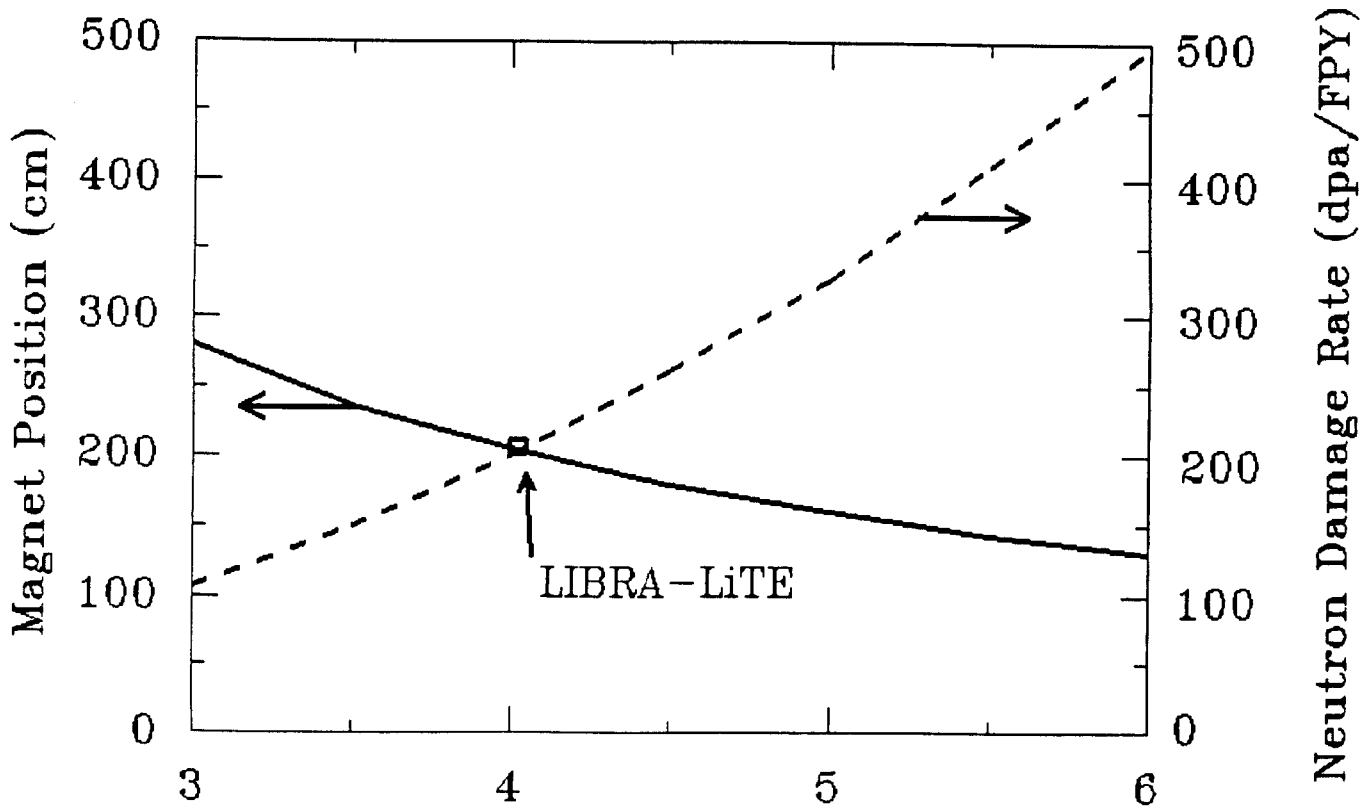


Figure 9.3. Distance from target to magnet surface and neutron wall loading to magnet surface versus microdivergence.

system. Some method of isolating the diode from the gas will be required. There will be some impurity of lithium vapor, but it is not expected to affect beam transport. The microdivergence is chosen, based on the preceding arguments, to be 4.0 mrad. SCATBALL predicts that the 7.14 cm radius beam spreads to 9.0 cm at the lens magnets. The 470 cm drift length between the diodes and the magnets is what most of the main pulse beams experience. The top row of main pulse beams will drift 765 cm and will require a larger bore magnet. The magnets have a focal length measured from the magnet center to the target of 230 cm. The magnets have an average field of 1.2 tesla and a length of 50 cm, which is required to focus a 30 MeV lithium beam. Not considered in detail is the transport of 20 MeV lithium beams but it has been assumed that the lens magnets will be similar to the main pulse ions. The main beams will be focused to a 0.95 cm radius spot.

Table 9.1. Ion Beam Transport Parameters

Gas species	Helium
Gas density	$3.55 \times 10^{16} \text{ cm}^{-3}$
Beam microdivergence	4.0 mrad
Diode outer radius	25.773 cm
Diode inner radius	25.385 cm
Diode to magnet distance	470 cm
Length of magnet	50 cm
Average magnetic field in magnet	1.2 tesla
Beam radius at magnet	9.0 cm
Magnet to target distance	230 cm
Beam radius at target	0.95 cm

References

- [1] C. L. Olson, "Achromatic Magnetic Lens Systems for High Current Ion Beams," Proc. 1988 Linear Accelerator Conference, CEBAF Report 89-001, p. 34 (1989).

10. Breeder and Coolant Choice

The features of LIBRA-LiTE have been compared for two breeder/coolant options. These are liquid lithium and the $\text{Li}_{17}\text{Pb}_{83}$ eutectic. The impact of using $\text{Li}_{17}\text{Pb}_{83}$ instead of Li on the LIBRA-LiTE performance parameters is given in Table 10.1. Neutron multiplication in lead results in a higher damage rate and shorter lifetime for the INPORT tubes and final focusing magnets. The lifetimes are reduced by 27% and 43% for the INPORT tubes and magnets, respectively. Detailed results of the neutronics performance with the two coolants is given in Chapter 14. While both yield nearly the same overall TBR and energy multiplication, highly enriched lithium should be used with $\text{Li}_{17}\text{Pb}_{83}$ compared to natural lithium in the case of liquid lithium. This is required to insure tritium self-sufficiency with adequate chamber wall protection. This results in a factor of five higher coolant/breeder cost.

The factor of ~ 17 higher density for $\text{Li}_{17}\text{Pb}_{83}$ will require more support structure for the piping and final focusing magnets. The higher electrical resistivity of $\text{Li}_{17}\text{Pb}_{83}$ results in increasing the dissipated power in the final focusing magnets by a factor of ~ 4 with a significant increase in the recirculating power. Furthermore, the $\text{Li}_{17}\text{Pb}_{83}$ vapor has a lower thermal conductivity and a higher atomic mass and, therefore, condenses more slowly than Li. This results in limiting the achievable repetition rate. In addition, the vapor in the chamber resulting from $\text{Li}_{17}\text{Pb}_{83}$ is expected to excessively scatter the ion beam. The impulse pressure from x-ray induced ablation of the first few microns of wetted surfaces is about a factor of 5 higher for $\text{Li}_{17}\text{Pb}_{83}$ compared to Li mainly due to the lower heat of vaporization. This results in a greater dynamic response of the INPORT units with $\text{Li}_{17}\text{Pb}_{83}$. Liquid metals contained in the final focusing magnets and INPORT tubes will develop a sudden pressure rise from the instantaneous temperature change associated with nuclear heating. For the same yield and geometry of the component, the peak pressure in the $\text{Li}_{17}\text{Pb}_{83}$ is higher than that in pure lithium by a factor of ~ 5.5 .

The safety concern related to using Li is the possibility of having a lithium fire. The use of lead in the intermediate heat transfer circuit will prevent the accidental mixing of lithium with the steam cycle. On the other hand, the lead in $\text{Li}_{17}\text{Pb}_{83}$ produces polonium 210 which has a high radioactive hazard potential. The low tritium solubility in $\text{Li}_{17}\text{Pb}_{83}$ results in a lower tritium inventory in the coolant but will increase the potential for tritium leakage from the primary coolant loop to the intermediate and secondary loops. Based on these comparisons, liquid lithium is chosen as the breeder and coolant in LIBRA-LiTE.

Table 10.1. Impact of Using $\text{Li}_{17}\text{Pb}_{83}$ Instead of Li on LIBRA-LiTE Performance Features

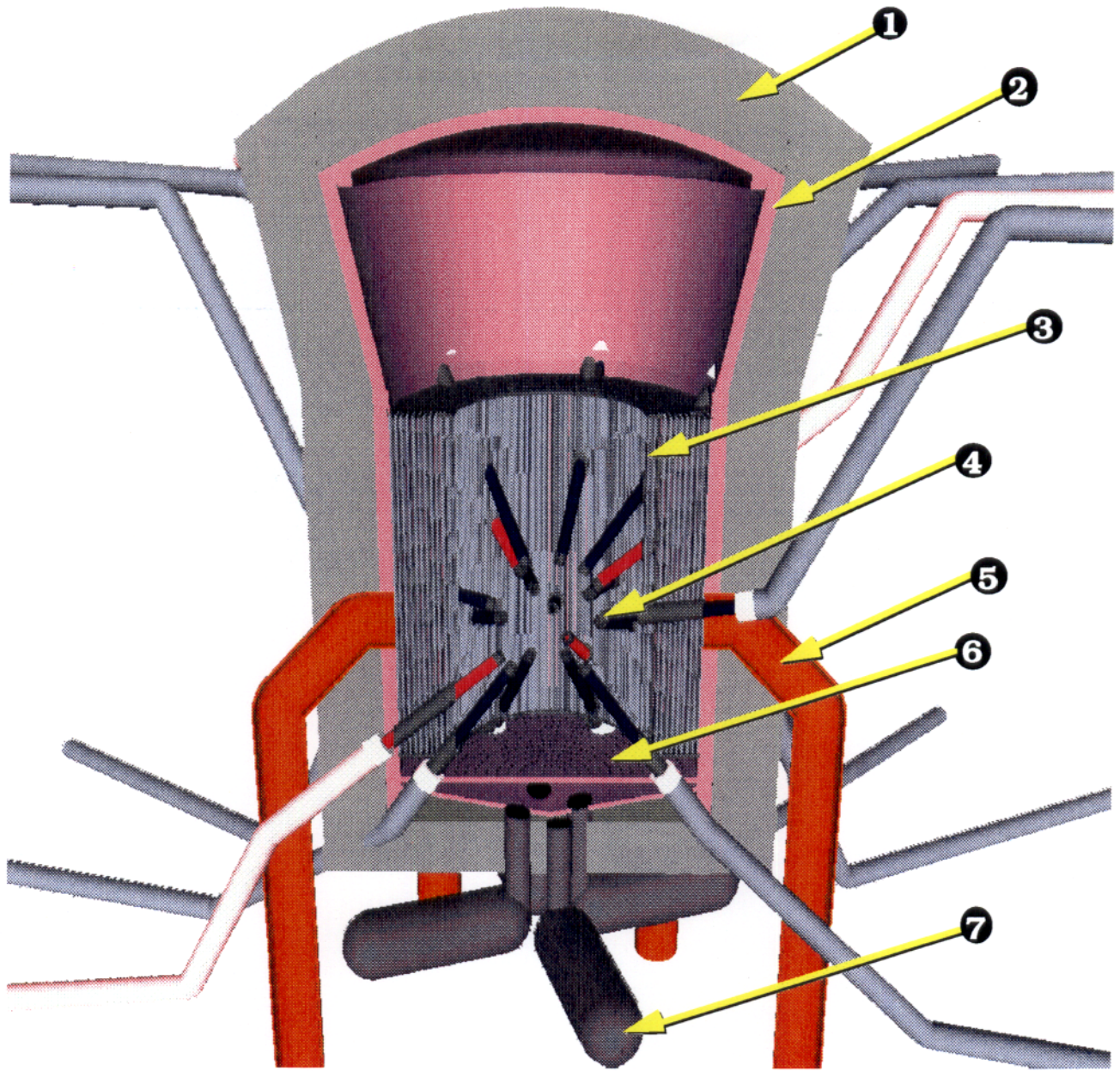
Parameter	Degradation	No Effect	Improvement
Maximum repetition rate	Lowered		
Ion beam transport	Worse		
Li enrichment	Require higher level		
Overall TBR		Same	
Overall energy multiplication		Same	
INPORT unit lifetime	Shorter		
Magnet lifetime	Shorter		
Magnet power	Higher		
Structural support	More required		
Isochoric heating	Higher		
Impulse pressure	Higher		
INPORT dynamic response	Greater		
Tritium inventory			Lower
Tritium leakage to secondary loop	Higher		
Safety concerns			Lower
Cost	Higher		

11. Reactor Chamber Layout

The reaction chamber in LIBRA-LiTE is an upright cylinder, 13.6 m high which has an inverted conical roof extending an additional 9 m above the cylindrical portion. The floor of the chamber consists of a perforated drain plate followed by a sump leading to intermediate heat exchangers (IHX) built into the base of the chamber. The radius to the cylindrical vacuum chamber wall (also the reflector) is 5.7 m and the reflector thickness is 50 cm. The chamber structural material is ferritic steel HT-9 and the breeding/cooling material is liquid lithium.

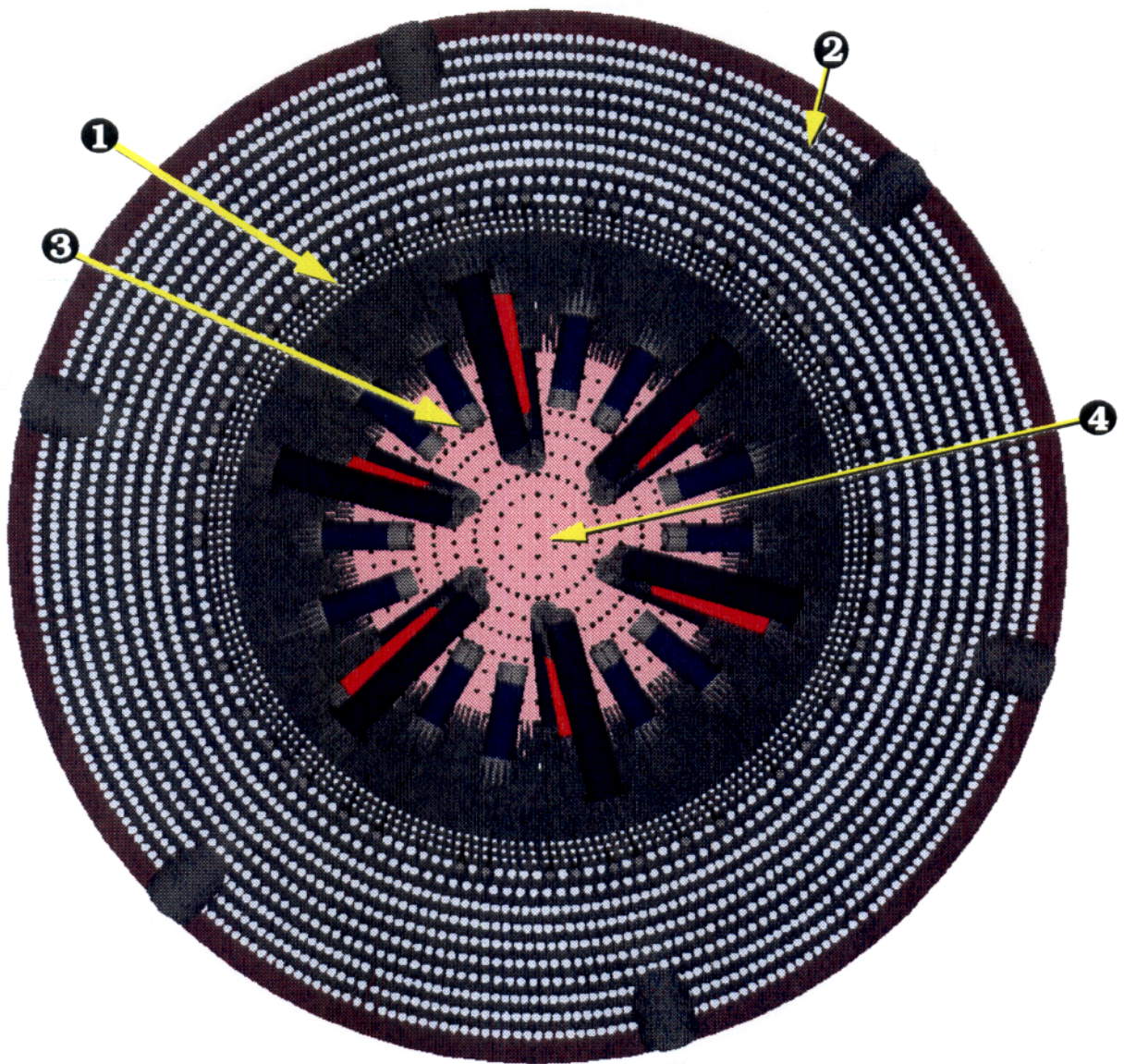
Figure 11.1 is a cross sectional view of the chamber showing the internal components. Most prominent are the beam lines which transport the ions to the target. In this figure only 18 beam lines of the total of 30 are visible. There are 24 main pulse beams and 6 prepulse beams. The 24 main pulse beams are divided into four groups of six beams each. Each beam in any one group lies along the surface of a right cone with its vertex at the target and its axis coincident with the chamber axis. There are two inverted cones with included angles of 74° and 160° respectively, and there are two upright cones with the same angles. The prepulse beams are oriented in the middle of the six sides of a cube situated with two corners on the chamber axis and the cube center at the target. Figure 11.2 is a top view of the chamber with the roof removed. All 30 beam lines can be seen. The prepulse beams are the middle beams in the grouping of three beams vertically, of which there are six.

The beam lines terminate in final focusing magnets situated at a distance of 2.05 m from the target. The ions are transported ballistically from the diodes to the final focusing magnets which then focus them onto the target. Because of the proximity of the final focusing magnets to the neutron source, it was decided to use a nonconventional magnet construction. The magnet design utilizes liquid Li as the conductor and thus gets away from the problem of degradation of electrical conductivity. In this design a five turn solenoid is used to generate a 1.2 tesla field for focusing the ions. The magnets are steady state and have a bore of 18 cm, an outer diameter of 46.3 cm and are 50 cm long. The outer case of the magnets is 0.5 cm thick HT-9 ferritic steel. On the inside of the case, however, there is a 0.1 cm thick HT-9 sheet insulated from the outer case with a layer of spinel ($\text{MgO}\cdot\text{Al}_2\text{O}_3$) ceramic. There are five turns made with this thin HT-9 sheet in a continuous fashion, extending the full length of the magnet from one end to the other. The beam lines on which the final focusing magnets are supported also contain supply and return lines for the Li as well as the busbars for energizing the magnets. These beam lines go all the way to the diodes and are designed to be disconnected for the purpose of component replacement. Focusing magnet and front INPORT unit maintenance is discussed in detail in Chapter 18. The front several centimeters of the magnet which face the target experiences a very high heat flux and consequently a very high temperature. For this



- (1) Shield
- (2) Reflector / vacuum chamber
- (3) INPORT units
- (4) Final focus magnet
- (5) Vacuum line
- (6) Perforated plate
- (7) IHX

Figure 11.1. Cross-sectional view of the reactor chamber.



- (1) Front INPORT units
- (2) Rear INPORT units
- (3) Single turn liquid LI lens magnet
- (4) Perforated bottom plate

Figure 11.2. Top view of chamber with roof removed.

reason, it is constructed from the Mo alloy TZM. This part of the magnet also has Li flowing through it at a high velocity to achieve a high heat transfer coefficient. Further, the side facing the target is designed to have a wetted surface so that heat can be dissipated by latent heat of evaporation. This energy is ultimately recovered when the vapor recondenses, but since this occurs over a longer time scale, the consequences are less severe. The remaining body of the magnet is constructed of HT-9. A detailed description of the magnet design is contained in Chapter 8 where issues of heat transfer and magnetohydrodynamics are addressed.

Figure 11.1 also shows the blanket zone which covers the entire cylindrical portion of the chamber. The function of the blanket is to breed T_2 , convert nuclear energy to thermal energy and to protect the nonreplaceable chamber components from neutron damage, specifically the reflector/vacuum chamber. The blanket zone is 2.25 m thick, with the first surface at a radius of 3.45 m from the target at the midplane. This blanket zone consists of flexible tubes made of tightly woven HT-9 ferritic steel wires through which liquid Li flows. They extend the full height of the cylindrical part of the chamber and constitute 33% volumetric fraction of the blanket zone. These tubes are called INPORT (Inhibited flow Porous Tubes) units. The idea behind the INPORT concept is to make the tubes porous so they can maintain a wetted surface, to make them flexible so that they can withstand shocks, and to surround the liquid Li stream with a structural material to prevent it from disassembling from isochoric heating following a shot. The large number of tubes provides a very large surface area to condense the vapor, while at the same time allowing a high rep-rate by preventing the Li streams from being disassembled after each shot. There are three rows of 5 cm diameter INPORT units at 10 cm between centerlines both circumferentially and radially. The distance between the rows is determined by dynamic analysis which takes into account rep-rate, tube tension, Li velocity and other parameters. The rear tubes are 12 cm in diameter and there are 14 rows of them. All the INPORT units are 11.8 m long. At the locations where the beam tubes penetrate the blanket there are collars to which the tubes are attached from above and from below. In this way the coolant goes around the beam tube and continues to flow through the tubes downstream from the penetration.

Extending from the cylindrical portion of the chamber upwards is an inverted cone terminating in a spherical segment, resembling a mushroom. Since there are no INPORT units protecting the roof, it was removed to a radius of 16 m from the target, a distance at which it becomes a lifetime component according to neutronic calculations. The roof is cooled with liquid Li as is the reflector, and thus will condense vapor. This resultant wetted surface acts to absorb the high heat flux emanating from the target. Droplets falling from the roof are not a problem since they will be evaporated long before they reach the area of the beams. The conical sides of the inverted cone are shadowed by the INPORT units and thus are also protected from

the primary neutrons. The spherical segment of the roof can be removed to provide access to the inside of the chamber for maintenance of internal components.

The base of the chamber is a pool of liquid Li. The Li from the INPORT units and from the reflector collects in the pool, then drains through a perforated plate. This plate has two important functions; it acts as a shock absorber by allowing the fluid to be forced through the perforations after a shot and it isolates the liquid pool below it by a space, thus preventing the shock from getting transmitted to the IHX. Obviously the dynamics of the Li flow have to be carefully configured for the perforated plate to perform as intended. After passing through the perforated plate, the liquid collects in a sump from which it flows into the IHX. Pumps downstream from the IHX create the suction needed to pull the Li through the IHX and the head required for circulating it back through the chamber.

The beam diodes are located at the chamber reflector, which means that the diodes are at different distances from the target. The closest diodes are 5.7 m and the farthest, 9.5 m from the target. It has been assumed that there will be a fast shutter system isolating the diodes from the beam lines leading to the target. This will allow the chamber to be at a higher pressure than the beam lines upstream from the diodes. A shutter system consisting of two discs rotating in opposite directions can isolate the diodes from the beam lines allowing them to be open at the shot frequency long enough for the beam to pass through. Differential pumping will be used to evacuate whatever noncondensable gases enter the beam lines while they are open.

The chamber is surrounded on all sides by a steel reinforced concrete shield cooled with gaseous He. The thickness of the shield is 2.7 m at the midplane but varies elsewhere, depending on the distance from the target. Extending from the reflector at midplane are six vacuum tubes leading to an expansion tank located below the reactor chamber. The function of these tubes is to exhaust the noncondensable gases along with some vapors into the expansion tank, where they are pumped out by vacuum pumps. This system is designed to extract the maximum energy from the gases by allowing them to flow through the forest of INPORT units as they expand isentropically into the expansion tank. A more detailed discussion of this system is contained in Section 12.2.

12. Chamber Gas Dynamics Analysis

12.1. Vaporization

The target microexplosion releases x-rays, neutrons and ion debris that deposit in the target chamber vapors and structures. It is assumed that the energy partitioning and the emitted spectra are the same as for the ion beam target designed by Bangerter [1]. Some parameters are shown for this target in Table 12.1. The time-integrated x-ray spectrum has been calculated [2] for this target and is shown in Fig. 12.1. The time-dependent x-ray power is shown in Fig 12.2. The x-ray emissions consist of three major components; a short burst of hard x-rays from the burning fuel, a short burst of soft x-rays from the outer lead shell heated by hard x-rays, and a longer burst at about 1.0 ns after the first two bursts that is radiated from the lead shell which has been heated by a collision with the inner shells. The effects of the neutrons are discussed in another section. The x-rays deposit in the liquid Li film on the INPORTs and the magnets. They also deposit in the domed roof, but the fluence there is low enough to avoid damage to the surface. A portion of the Li film is rapidly vaporized by the x-rays and the debris ions are deposited in that vapor and in the original Li vapor in the target chamber.

To analyze the behavior of the target chamber gases and vapors, the CONRAD computer code [3] has been used. CONRAD is a one-dimensional Lagrangian radiation-hydrodynamics computer code. Radiation transport is calculated with 20 group radiation diffusion and time-dependent target x-ray and ion deposition is included. The code includes calculation of vaporization and recondensation of materials from an outer wall and heat transfer through the wall. CONRAD simulations provide information on vaporization of wall materials, thermal and pressure loads on the walls, and condensation of vaporized material.

CONRAD simulations have been carried out for vaporization over materials from the surface of the INPORTs and the focusing lens magnets. Input parameters and results are listed for both calculations in Table 12.2. The initial temperature of the lithium film is respectively taken to be 500°C and 700°C for the INPORTs and focusing lens magnets. The initial temperatures are set by the bulk temperatures of the flowing lithium, the deposited heat that remains in the film after vaporization, the repetition rate, and heat transfer properties of the film and substrate. One result of these simulations is the energy remaining in the unvaporized part of the film, so iteration in the initial temperature is required. Heat transfer calculations in the lithium are reported in Chapters 8 and 16 and result in slightly different initial film temperatures from what has been assumed for these CONRAD simulations. The magnet initial temperature reported in Chapter 8 is about 800°C, which will lead to more energy being carried

Table 12.1. LIBRA-LiTE Target Parameters

Energy on target	6 MJ
Gain	100
Yield	600 MJ
X-ray yield	118 MJ
X-ray pulse width (ns)	1.5 ns
Debris ion yield	60.9 MJ
Neutron yield	407 MJ
Gamma yield	1.74 MJ
Endoergic losses	12.5 MJ

Table 12.2. CONRAD Simulations

	INPORTs	Magnets
Input		
Target to surface distance (cm)	345	205
X-ray fluence (J/cm ²)	78.9	224
Ion fluence (J/cm ²)	40.7	115
Initial film temperature (°C)	500	700
Initial film thickness (μm)	1000	1000
Initial vapor density (10 ¹⁵ cm ⁻³)	3.55	3.55
Results		
Mass vaporized (mg/cm ²)	3.47	7.79
Thickness vaporized (μm)	65.6	147
Remaining film thickness (μm)	934	853
Peak pressure at interface (GPa)	4.59	7.30
Impulse (Pa-s)	103	188
Final energy in vapor (J/cm ²)	76	267
Final energy in liquid (J/cm ²)	44	72.5

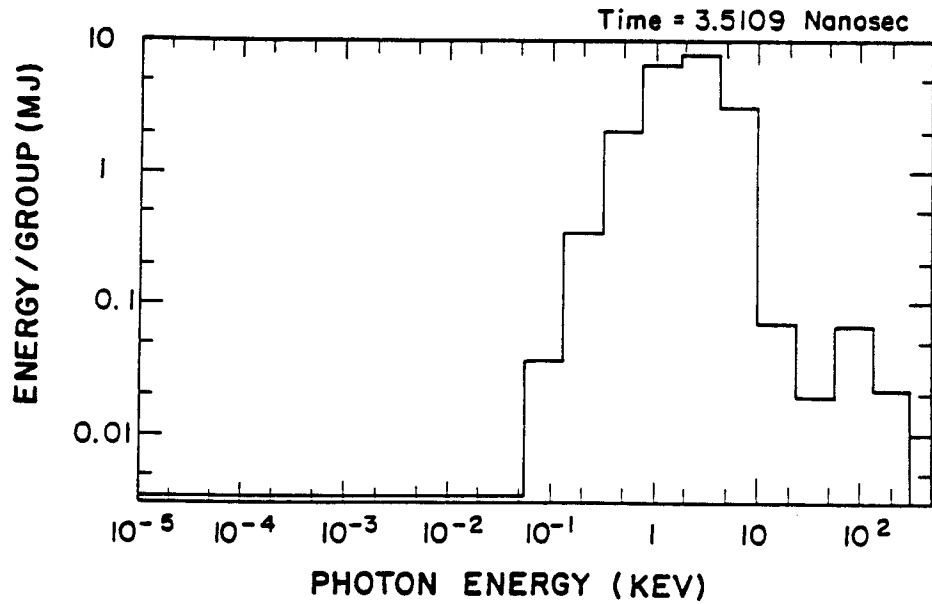


Figure 12.1. Time-integrated spectrum of x-rays emitted by LIBRA-LiTE target.

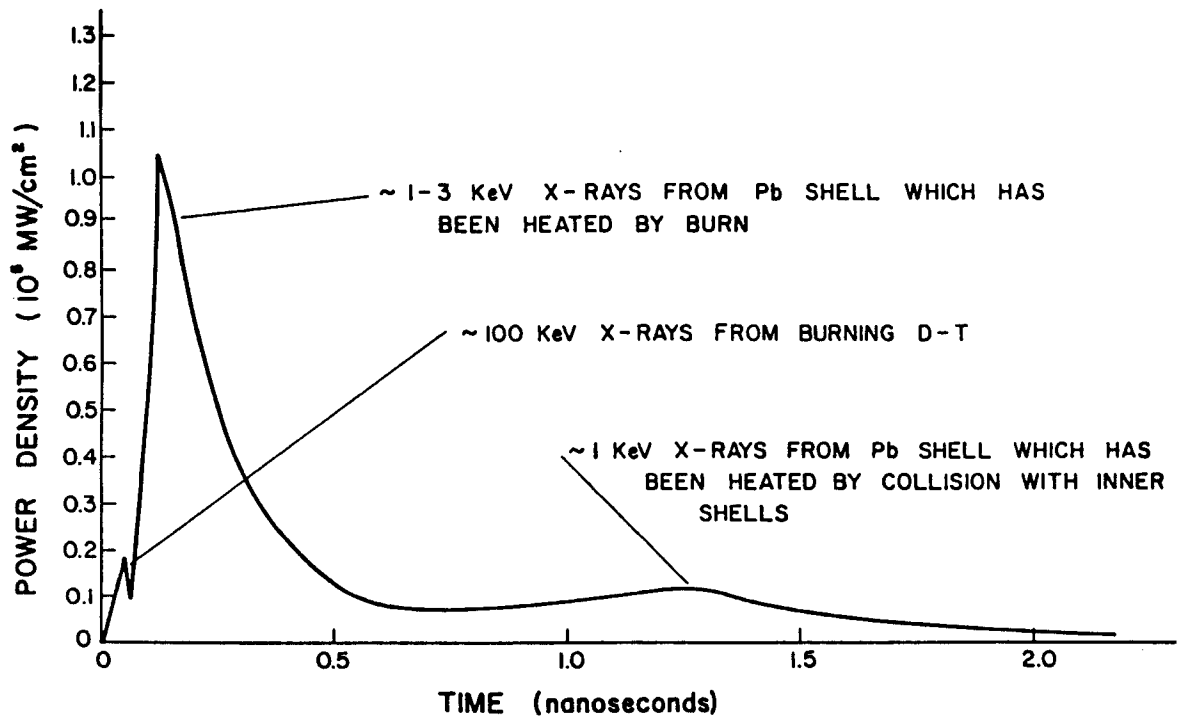


Figure 12.2. Time-dependent x-ray power emitted by LIBRA-LiTE target.

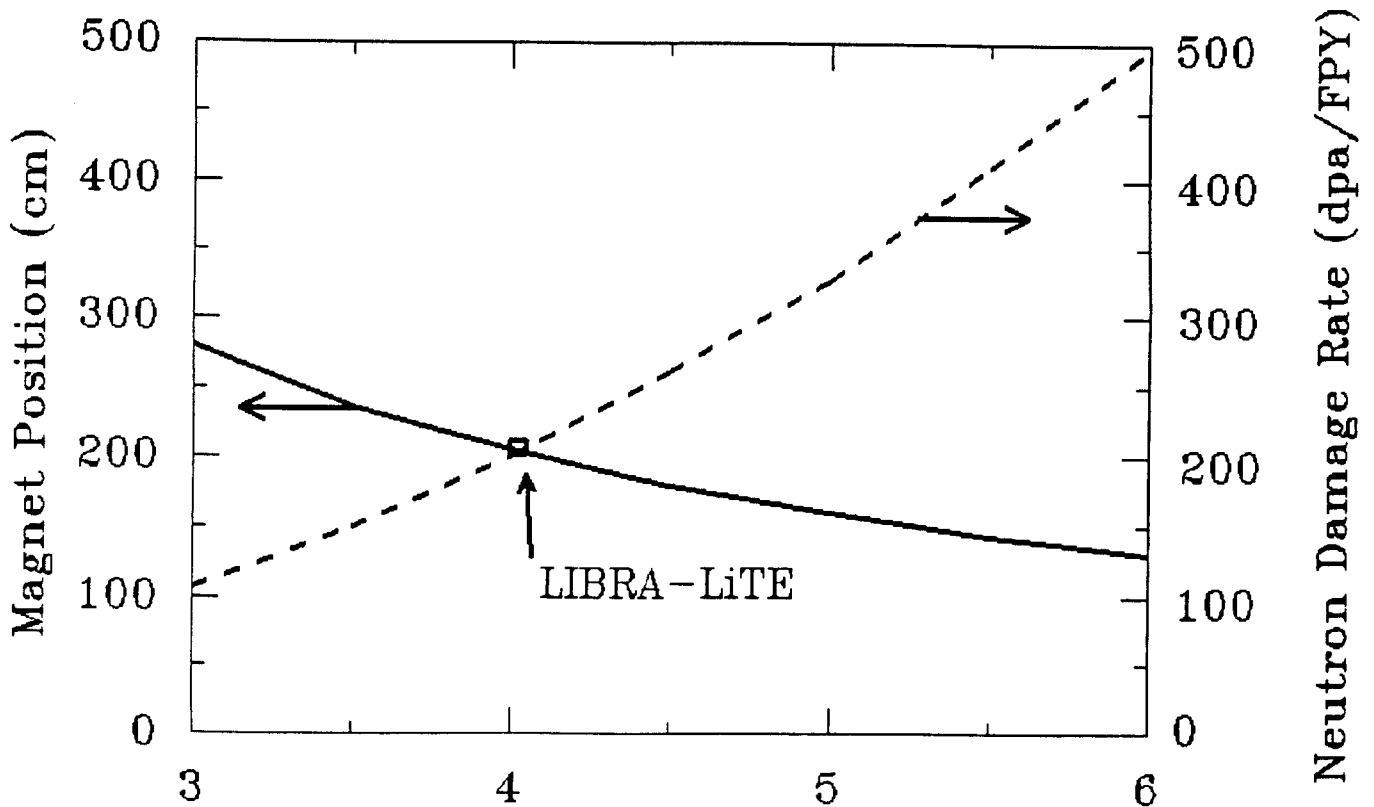


Figure 12.3. Pressure at vapor/liquid interface on surface of magnets.

off in the vapor in the CONRAD simulations and a lower average surface heating rate. The calculated initial temperature in the INPORT film is very close to the value assumed for these simulations. The simulations have shown that a shock wave is launched in the vaporized Li that leads to a very high peak pressure imposed on the remaining liquid at the vapor/liquid interface. The peak pressure is several GPa, which is certainly high enough to force a shock into the liquid. The pressure at the vapor/liquid interface on the focusing lens magnet surface and on the INPORT surface closest to the target is plotted against time in Fig. 12.3 and 12.4.

Not considered is the propagation of the shock in the liquid. The high peak pressure on the unvaporized portion of the film will send a shock through the film that could splash the film off of the INPORT or damage the INPORT over many shots. This remains a key development issue for LIBRA-LiTE. The impulses on the INPORTs and magnets will drive the bulk mechanical response of the INPORTs. The analysis of the bulk mechanical response of the INPORTs is discussed in Chapter 13.

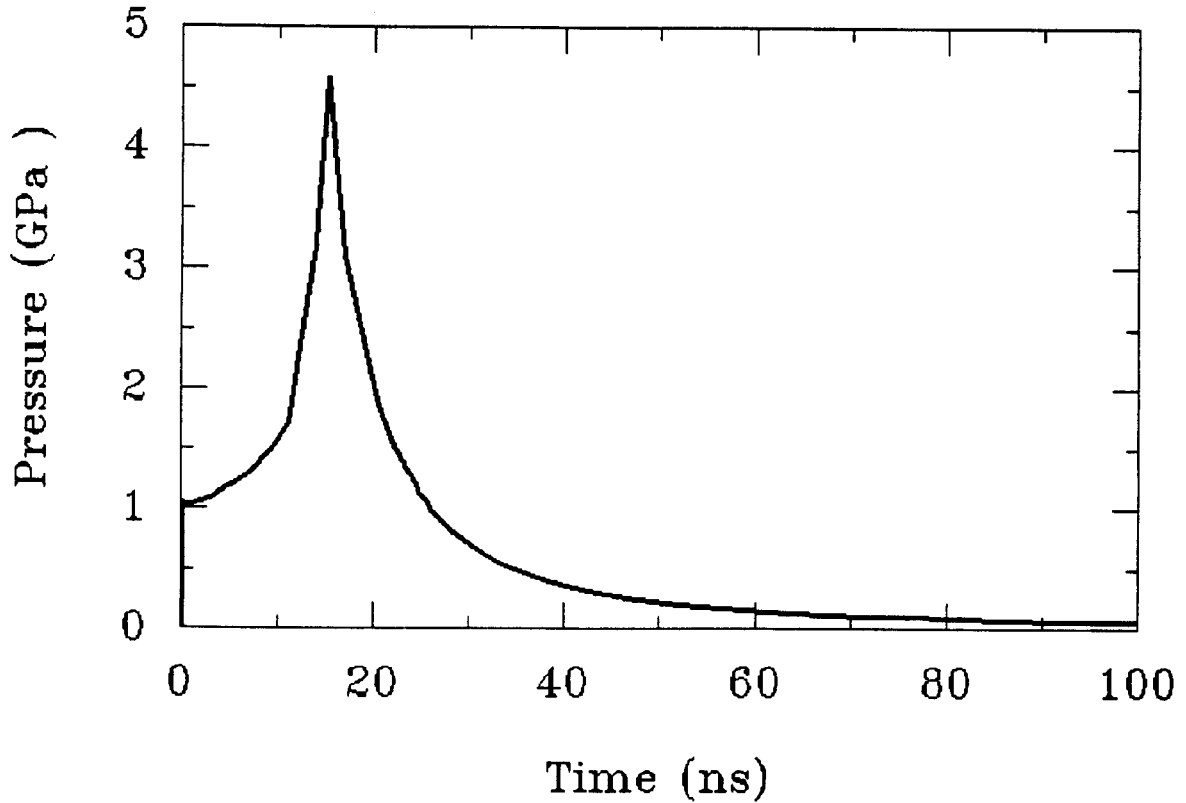


Figure 12.4. Pressure at vapor/liquid interface on surface of INPORTS.

After the vapor leaves the surfaces of the INPORTs and magnets, it flows to the center of the chamber and then up to the domed roof. The vapor will condense to some degree on the walls on the target chamber first surface. The rest of the vapor will pass through the INPORT banks, which will act like a cross-flow heat exchanger and extract much of the heat and mass from the vapor. The vapor and energy that remains at the back of the INPORT banks will flow into pipes that carry the vapor away to a surge tank. This flow will be self-driven by the pressure due to the energy deposited in the vapor.

12.2. Reactor Chamber Clearing

The LIBRA-LiTE reactor has a rep-rate of 3.9 Hz, which means the chamber environment must return to initial conditions in 256 ms after each shot. The initial conditions are that the chamber must have a He gas fill of one torr at 273 K which corresponds to an atom density of 3.55×10^{16} atoms/cm³. Since the temperature of the gas in the chamber will be more consistent with the temperature of the surrounding components, it is assumed to be 800 K. Immediately

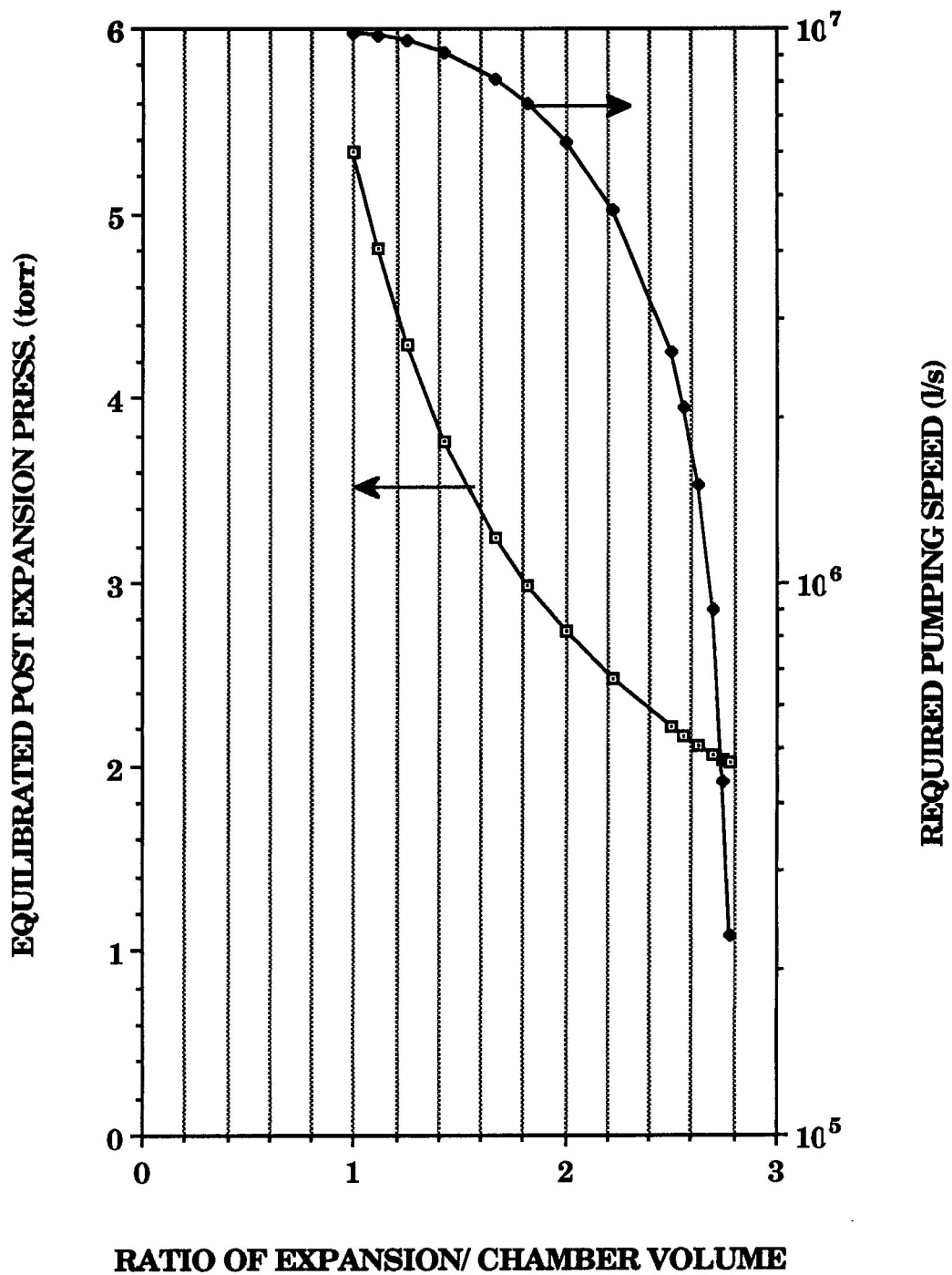


Figure 12.5. Equilibrated post expansion pressure and required pumping speed as a function of expansion/chamber volume ratio.

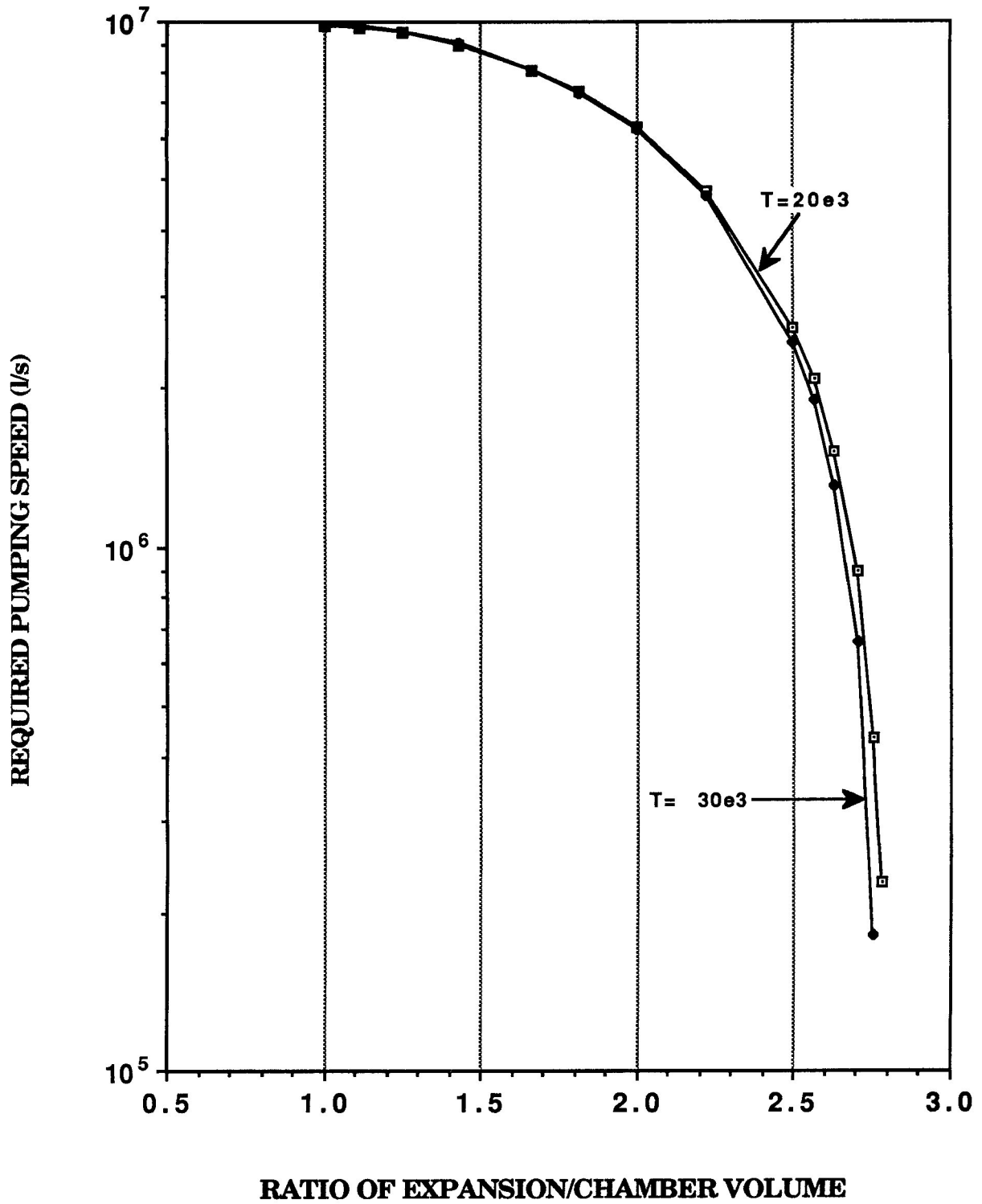


Figure 12.6. Required pumping speed for two He gas cooldown temperature as a function of chamber volume ratio.

Table 12.3. Chamber Evacuation Parameters

Chamber volume (m ³)	2.553 × 10 ³
Fill gas	He
Atom density (#/cm ³)	3.55 × 10 ¹⁶
He pressure at 273 K (torr)	1
<u>Before Shot</u>	
He gas temperature (K)	800
He gas pressure (torr)	3
<u>After Shot</u>	
He gas temperature (K)	30,000
He gas pressure (torr)	200
<u>Before Expansion</u>	
He gas cools down to	~ 20,000 K
Corresponding He gas pressure (torr)	132

after a shot, the temperature and pressure in the chamber rise to very high values. The hot Li vapor begins to condense on the cool internal chamber surfaces cooling the noncondensable He gas as well. At the same time the high pressure in the chamber expands into the expansion tank through the six large tubes arranged on the wall of the reflector at the midplane. In this analysis it is assumed that the gas will undergo an isentropic expansion, cooling itself in the process. At the same time, that gas which enters into the expansion tank is cooled to 800 K by a spray of a Li mist which rains continuously in the tank. Table 12.3 gives the parameters used in the determination of the expansion tank size and the pumping capacity needed within it.

As the vapor and the residual noncondensable gases continue to cool down to 800 K, depending on the size of the expansion tank the pressure in the system equilibrates to some value > 2 torr. Figure 12.5 is a plot of the equilibrated pressure in the system after expansion and cooldown to 800 K as a function of the ratio between the expansion tank volume and the chamber volume. It can be seen that when the ratio reaches a value of 2.8 the pressure is slightly higher than 2 torr. The figure also shows the required pumping speed as a function of the volume ratio. One can see that for a ratio of 2.8 the vacuum pumping speed is a reasonable 2.3×10^5 l/s. Just prior to the next shot fresh He gas is injected into the chamber to build up the atom density and pressure to the initial pre-shot conditions.

One might ask whether the assumption that the gas cools down to 20,000 K is reasonable. However, it is found that the system is very insensitive to the initial temperature before the expansion. Figure 12.6 gives the pumping speed requirement as a function of chamber

volume ratio for initial temperatures of 20,000 K and 30,000 K. The required pumping speed is essentially the same.

References

- [1] R. O. Bangerter, "Targets for Heavy Ion Fusion," *Fusion Technology*, **13**, 348 (1988).
- [2] B. Badger, et al., "HIBALL - A Conceptual Design Study of a Heavy-Ion Driven Inertial Confinement Fusion Power Plant," University of Wisconsin Fusion Technology Institute Report UWFDM-450 (June 1981).
- [3] R. R. Peterson, J. J. MacFarlane, and G. A. Moses, "CONRAD - A Combined Hydrodynamic-Condensation/Vaporization Computer Code," University of Wisconsin Fusion Technology Institute Report UWFDM-670 (1988).

13. INPORT Performance

The general equations of motion describing the mechanical response of the INPORT units under sequential impulse loadings can be found in earlier publications [1, 2]. The three-dimensional motion of the tubes is characterized by considering the radial and circumferential displacements when coupled with the axial component. (Axial inertia can be neglected in this case, however, coupling exists through nonlinear displacements.) It is expected that the first two rows of INPORT units will be subjected to the radial impulse load. This pressure load (applied uniformly over the length) has been calculated to be approximately 103 Pa-s for the 600 MJ target. The primary response to the dynamic impulse load will be radial; however, it has been shown that the tubes could begin to “whirl” depending upon the specific design parameters. For practical purposes, it would be advantageous to allow only planar motion of the INPORT units.

For the proposed LIBRA-LiTE cavity, a number of the tube design parameters are fixed. Table 13.1 shows the INPORT system parameters which have been set by power requirements, heat transfer requirements, material selections, etc. Obviously, the length of the tubes and the pretension (applied via spring-like supports) remain as design variables. Two possibilities have been considered for the length option, i.e., either the tubes span the full length of the chamber unsupported (equivalent to 11.8 m) or a midspan support is included. Consequently, a parametric study was performed to determine the effect of the axial pretension on the maximum dynamic response for the two possible lengths.

For a preliminary analysis, the maximum transient response in the radial and circumferential directions was calculated as the tension varied from 4.0 to 40 kN. Damping was set at 20%; however, lower levels will also be considered in future computations. The computer simulations showed that for the design parameters given in Table 13.1, the dynamic response remained planar (circumferential displacements were essentially zero). Figure 13.1 shows the maximum radial displacements as a function of the applied pretension. Resonant conditions are apparent as the tension is increased, yielding peaks in the response curves. In addition, it is evident from the figure that in order to keep the maximum transient displacement below 10 cm, either the axial tension must be set extremely high or a midspan support is needed. It should be noted that steady state conditions involve displacements of lower magnitudes, which in the past have been kept to approximately 5 or 6 cm. The transient displacements were used here to serve as guidelines and illustrate a worst case scenario; the final design, however, will be based on steady-state conditions.

Determining the maximum allowable tension in the tube depends upon the actual construction of the INPORT unit in conjunction with the maximum allowable stress. For HT-9 at

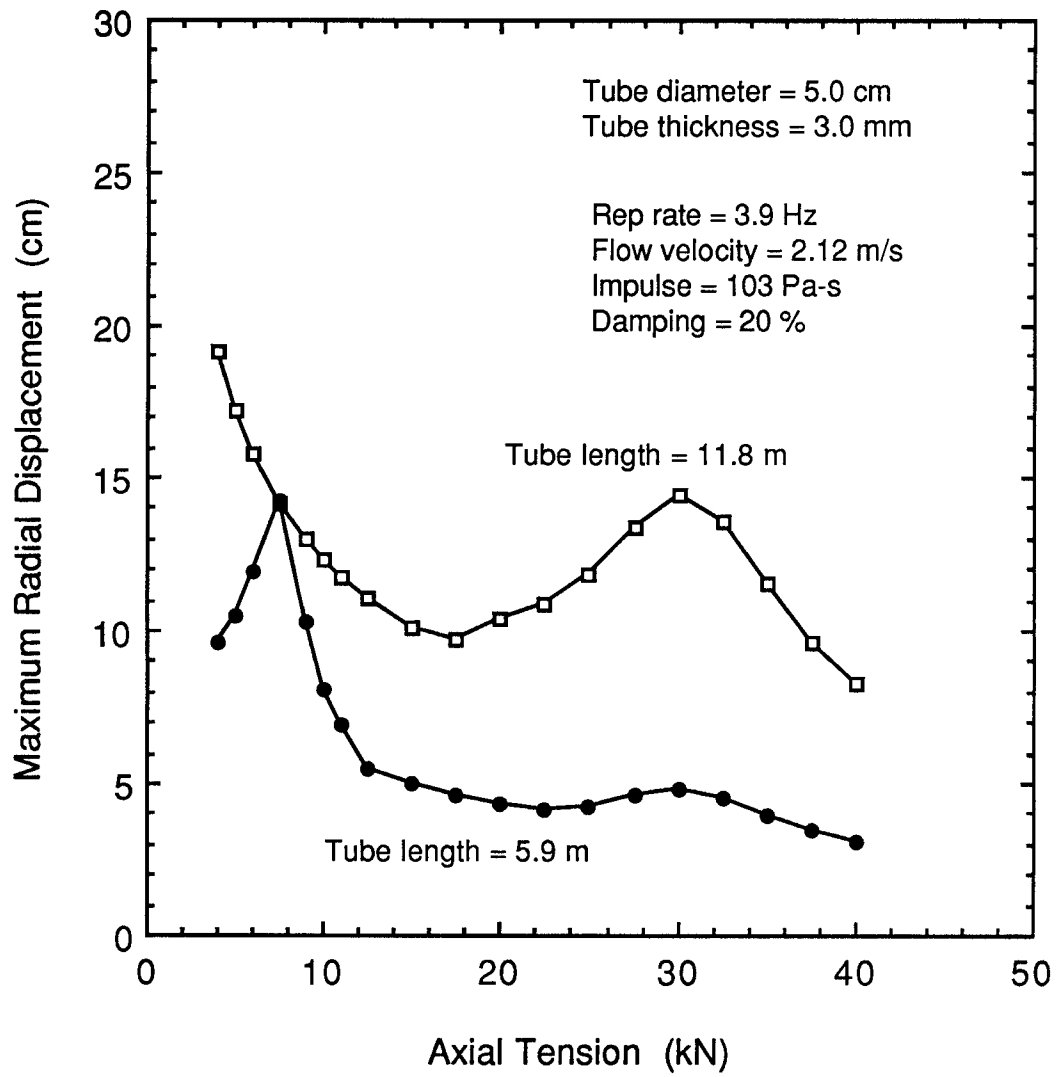


Figure 13.1. Maximum transient displacement of the INPORT units as a function of applied axial pretension.

Table 13.1. INPORT System Parameters

Tube material	HT-9
Liquid metal	Li
Tube diameter (cm)	5.0
Tube thickness (mm)	3.0
Flow velocity (m/s)	2.12
Rep rate (Hz)	3.9

550°C and 150 dpa the creep-rupture strength is rated at 115 MPa [3]. With the inner diameter and thickness of the tube set at 5.0 cm and 3.0 mm, respectively, the geometric cross section is equal to $3.333 \times 10^{-4} \text{ m}^2$. It is also essential that the INPORT units have sufficient porosity to provide a protective layer of liquid lithium. Assuming a 67% solid density for the tubes, of which 33% to 67% is of axial load bearing material, yields allowable tensions of 12.78 kN to 25.56 kN. Consequently, using Fig. 13.1, the optimum design for minimum displacements would include a midspan support with an axial pretension of 22.5 kN applied to the INPORTs.

References

- [1] R. L. Engelstad and E. G. Lovell, "Basic Theory for Three-Dimensional Motion of LIBRA INPORT Tubes," Fusion Power Associates Report FPA-84-2, October 1984.
- [2] B. Badger et al., "LIBRA - A Light Ion Beam Fusion Conceptual Design," UWFD-800, University of Wisconsin Fusion Technology Institute, July 1989, Revised February 1990.
- [3] "Blanket Comparison and Selection Study - Final Report," Argonne National Laboratory, ANL/FPP-84-1, Vol. 2, Chapter 6, p. 6.7-6.

14. Neutronics Analysis

14.1. Calculational Method

Neutronics analysis has been performed for LIBRA-LiTE by performing several one-dimensional spherical geometry calculations for the different regions surrounding the target. The discrete ordinates code ONEDANT [1] was utilized along with 30 neutron – 12 gamma group cross section data based on the ENDF/B-V evaluation. A point source is used at the center of the chamber emitting neutrons and gamma photons with the LIBRA target spectrum [2]. The target spectrum takes into account neutron multiplication, spectrum softening and gamma generation resulting from the interaction of the fusion neutrons with the dense target material. For each DT fusion reaction, 1.025 neutrons are emitted from the target with an average energy of 11.64 MeV. In addition, 0.013 gamma photons are emitted with 3.85 MeV average energy. 2.1% of the fusion energy is lost in endoergic reactions in the target and 69.5% of the target yield is carried by neutrons and gamma photons which interact with the different regions surrounding the target resulting in tritium breeding, nuclear heating, and radiation damage. The rest of the target yield is carried by x-rays and debris which deposit their energy as surface heat. The results presented here are normalized to a 600 MJ DT fuel yield and a repetition rate of 3.9 Hz.

14.2. INPORT Tube Region

The primary goal of the neutronics analysis performed for LIBRA-LiTE is to determine the blanket design that satisfies tritium self-sufficiency, large energy multiplication (M), and wall protection requirements. The blanket is made of banks of INPORT tubes with 0.33 packing fraction. The liquid lithium breeder flows in tubes which are made of the ferritic steel alloy HT-9. The tubes consist of 2 vol.% HT-9 and 98 vol.% Li. A 0.5 m thick reflector consisting of 90 vol.% HT-9 and 10 vol.% Li is used behind the blanket. A minimum local (1-D) tritium breeding ratio (TBR) of 1.3 is required in the INPORT tubes and reflector. This relatively high TBR is required to achieve overall tritium self-sufficiency with a simple roof design that does not have a breeding blanket. In addition, the INPORT tubes are required to provide adequate protection for the front of the reflector (chamber wall) to make it last for the whole reactor life. In this study, we adopted a conservative end-of-life dpa limit of 150 dpa for the ferritic steel HT-9. Hence, for 30 full power years (FPY) of operation, the peak dpa rate in the HT-9 chamber wall should not exceed 5 dpa/FPY. The inner radius of the chamber wall is determined by the diode location and is taken to be 5.7 m.

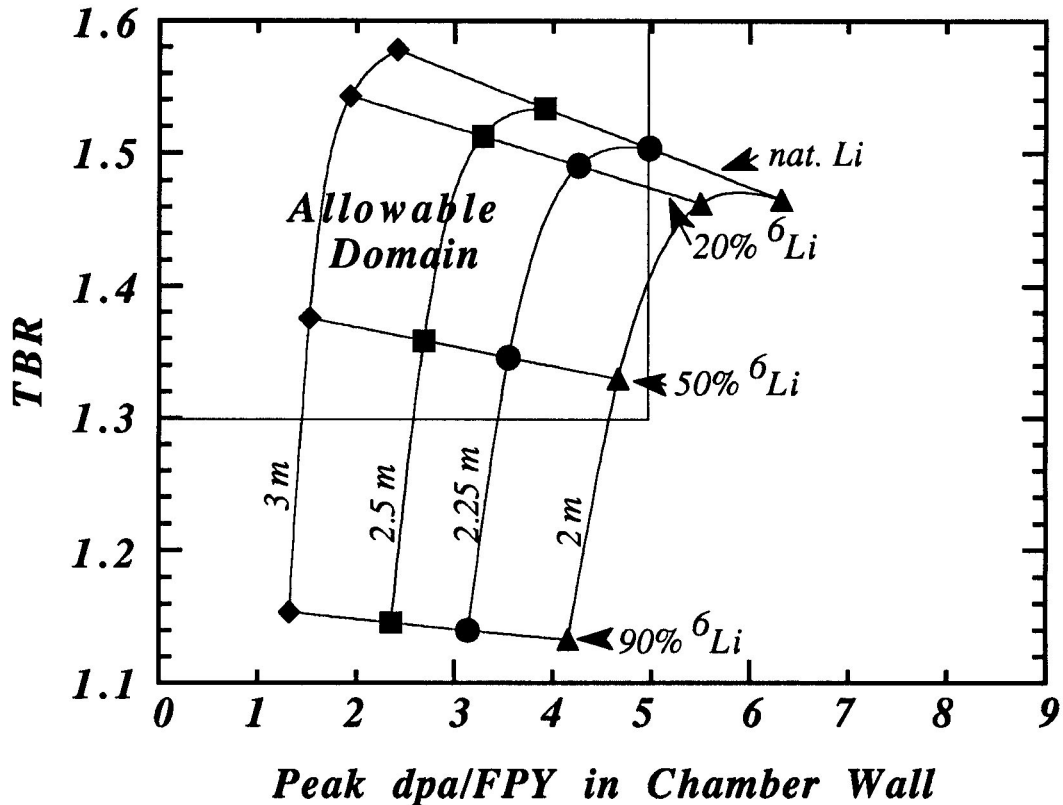


Figure 14.1. TBR and chamber wall damage rate for different blanket design options.

Several calculations have been performed for different blanket thicknesses and lithium enrichments. The results are mapped in Fig. 14.1. In order to satisfy the tritium breeding and wall protection requirements, the design point should be in the box indicated in the upper left corner of the graph. For a fixed lithium enrichment, increasing the blanket thickness results in significant reduction in chamber wall damage, a small enhancement in the TBR, and slight reduction in energy multiplication as indicated in Fig. 14.2. Decreasing the lithium enrichment for a given blanket thickness results in a small increase in chamber wall damage and a significant increase in TBR. The energy multiplication is not sensitive to the lithium enrichment as shown in Fig. 14.3.

The peak damage rate in the INPORT units nearly doubles as the blanket thickness increases from 2 m to 3 m. Hence, there is a strong incentive for reducing the blanket thickness. Therefore, the blanket design point should be close to the right boundary of the allowable domain indicated in Fig. 14.1. Along this boundary different designs can be chosen ranging from a 1.9 m thick blanket with 50% ⁶Li enrichment to a 2.25 m thick blanket with natural

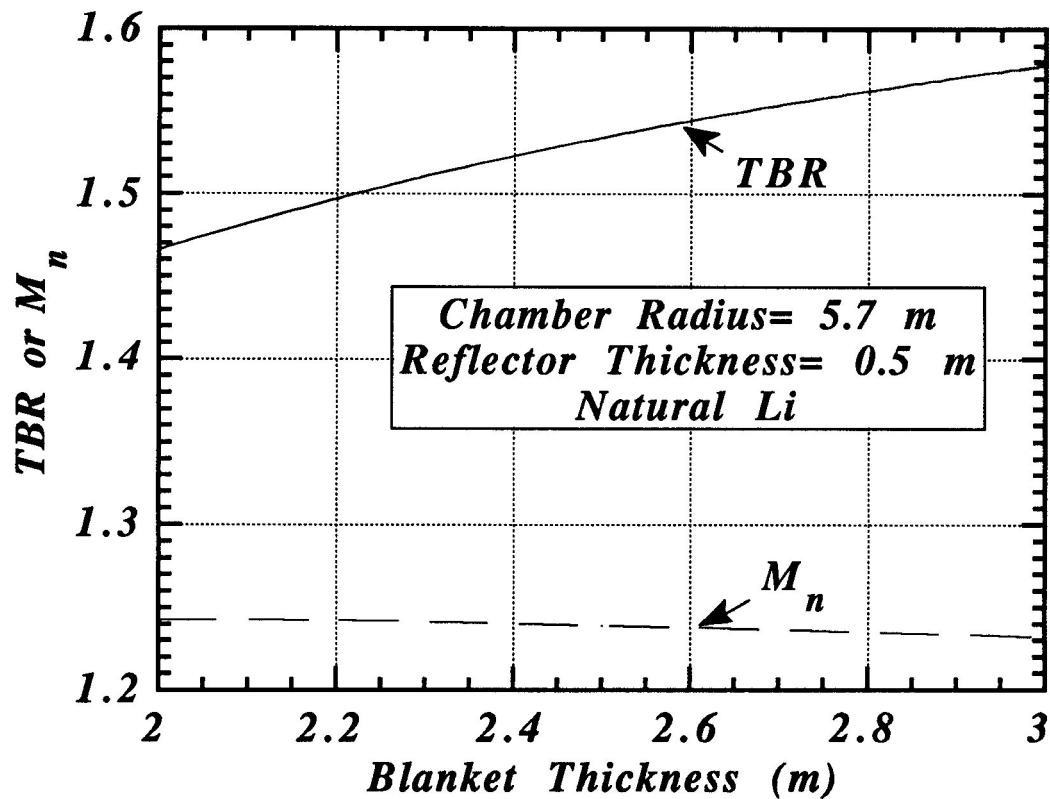


Figure 14.2. TBR and nuclear energy multiplication as a function of blanket thickness.

lithium. Comparing the nuclear performance for these two design points reveals that they yield nearly the same M with the thicker blanket resulting in 15% higher TBR. On the other hand, the thinner blanket results in 20% longer life for the INPORT tubes while requiring about an order of magnitude more expensive lithium that is enriched to 50% ${}^6\text{Li}$ in order to provide adequate chamber wall protection. Based on these results, the reference design point was chosen to be a 2.25 m thick blanket with natural lithium.

The front surface of the INPORT tubes is at 3.45 m from the target and is exposed to a neutron wall loading of 10.6 MW/m^2 . The peak dpa rate in the INPORT units is 68 dpa/FPY implying a lifetime of 2.2 FPY which corresponds to about 3 calendar years (CY) at 75% availability. A gradual reduction in the replacement frequency for the INPORT tubes can be achieved as one moves toward the back of the blanket with the back row of tubes being replaced only once during the reactor life. The peak dpa and helium production rates in the chamber wall are 5 dpa/FPY and 18.8 He appm/FPY, respectively. The chamber wall will last for the whole reactor life. Since spherical geometry has been used in the calculations, the damage rates

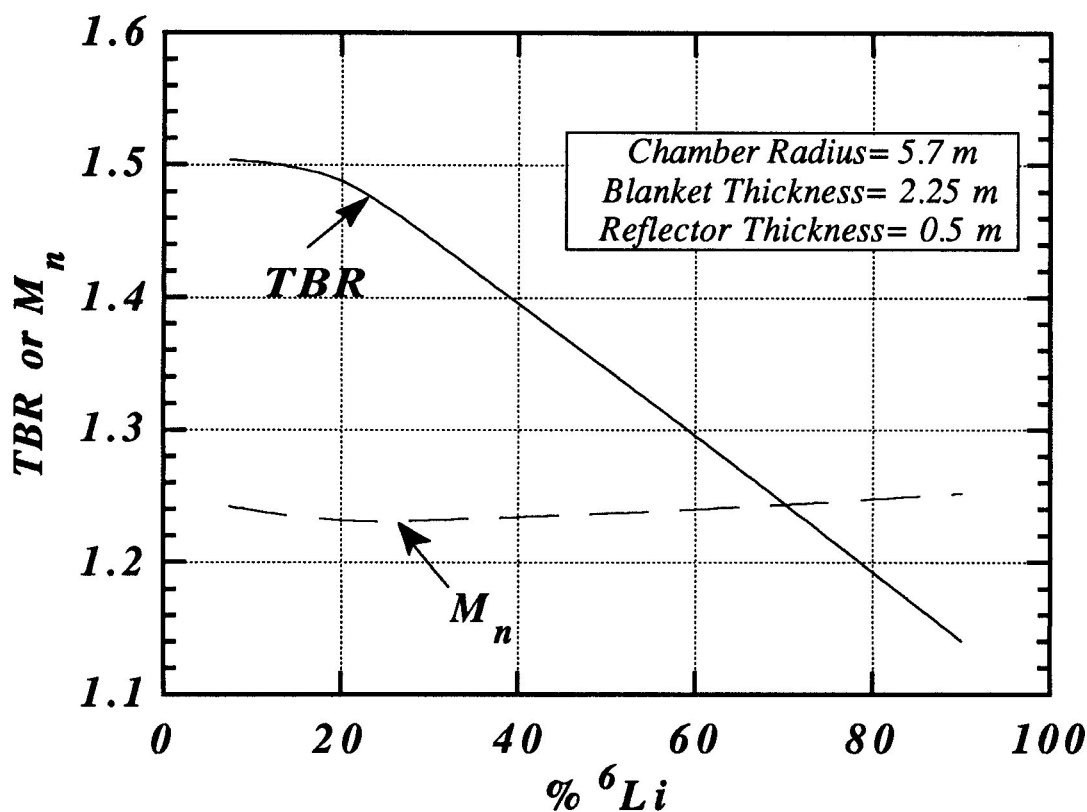


Figure 14.3. Effect of lithium enrichment on TBR and M_n .

given above represent the worst case conditions at the midplane of the cylindrical chamber. The local TBR is 1.504 and the local blanket nuclear energy multiplication M_n , defined as the ratio of nuclear heating to the energy of incident neutrons and gamma photons, is 1.242. The spatial variation of nuclear heating has been calculated for use in the thermal hydraulics analysis. The results are given in Fig. 14.4. The power density peaks at 23.3 W/cm³ in the front INPORT tubes and drops to 3.5 W/cm³ in the back tubes. The peak power density in the chamber wall is 4.8 W/cm³.

14.3. Reactor Roof

The roof of the chamber is a large dome that is required to be a lifetime component. The roof is 50 cm thick and consists of 80 vol.% HT-9 and 20 vol.% Li. Fig. 14.5 shows the peak dpa rate in the roof as a function of distance from the target. Based on these results, the roof of the LIBRA-LiTE chamber is located at 16 m from the target to ensure that it lasts for the whole reactor lifetime. The roof is exposed to a neutron wall loading of 0.49 MW/m². The

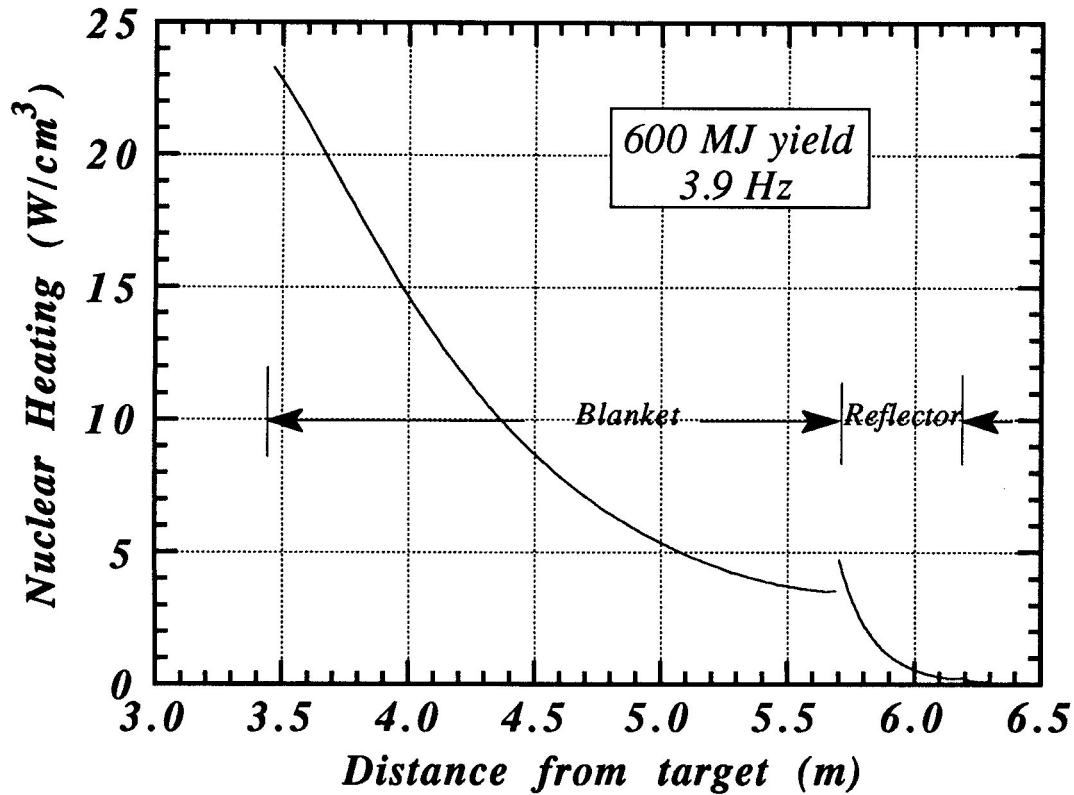


Figure 14.4. Spatial variation of nuclear heating in the INPORT units and reflector.

peak dpa and helium production rates in the HT-9 roof are 5 dpa/FPY and 28 He appm/FPY, respectively. The local TBR and M_n values are 0.558 and 1.299, respectively.

14.4. Bottom Lithium Pool

The bottom of the chamber consists of a lithium pool which is formed by the coolant flowing through the INPORT tubes. It drains through a 15 cm thick perforated plate made of HT-9, which acts as a reflector as well as a shock damper. This perforated plate consists of 80 vol.% HT-9 and 20 vol.% Li. The depth of the Li pool at the bottom of the reactor was determined to allow the bottom perforated plate to be a lifetime component. The upper surface of the pool is at 5 m from the target and is exposed to a neutron wall loading of 5 MW/m². Figure 14.6 shows the peak damage rate in the bottom plate as a function of pool depth. The results indicate that the pool depth should be at least 0.75 m implying that the bottom plate should be located at 5.75 m from the target. The peak dpa and helium production rates in

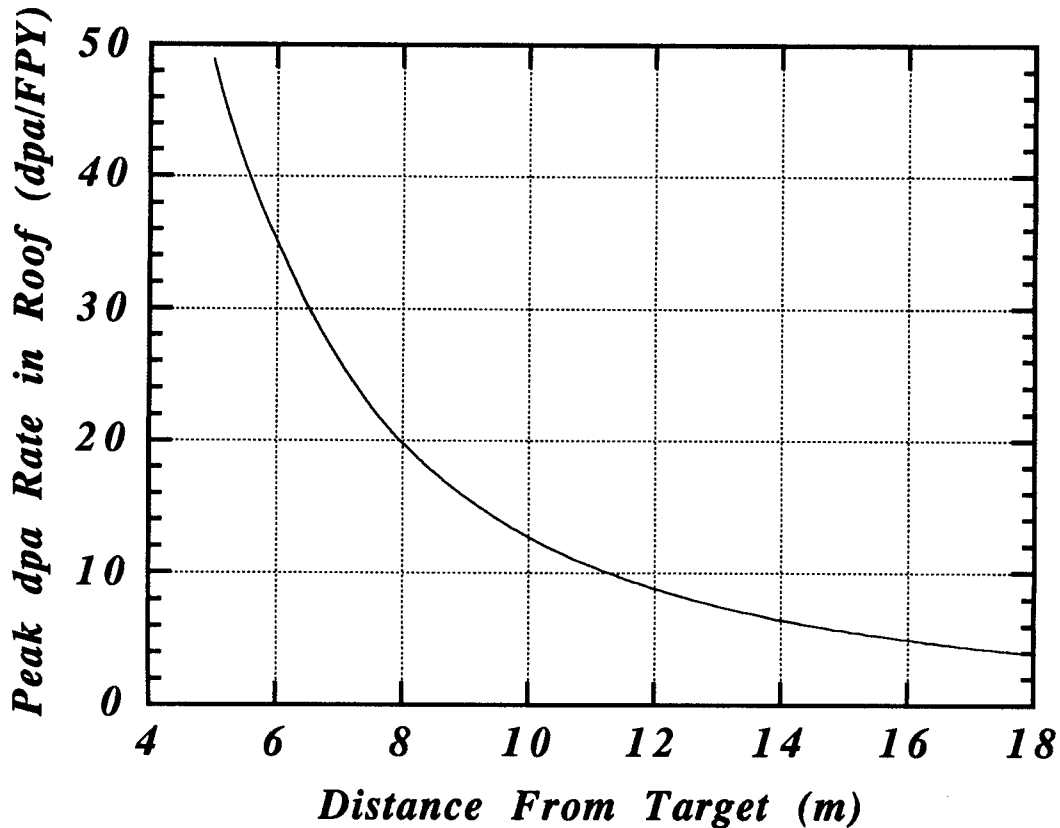


Figure 14.5. Peak damage rate in roof as a function of distance from target.

HT-9 are 5 dpa/FPY and 22 He appm/FPY, respectively. The local TBR and M_n values are 1.575 and 1.221, respectively.

14.5. Final Focusing Magnets

The final focusing magnets utilize lithium as a conductor flowing in a metallic case. Each of the 30 magnets has a center bore radius of 9 cm, a 12.8 cm thickness and a length of 50 cm. Ballistic propagation of the light ions requires the magnets to be located as close as possible to the target. The lifetime of the magnets is determined by radiation damage to the front metallic casing. Figure 14.7 shows the peak damage rate in the front of the magnet as a function of distance from the target. The location of the magnet is determined to be 2.05 m from the target to achieve a peak dpa rate of 150 dpa/CY implying magnet replacement every one calendar year. The neutron wall loading at the front surface of the magnet is 29 MW/m². The peak helium production is 1700 He appm/FPY. The local TBR and M_n values for the magnets are 1.017 and 1.034 respectively. Nuclear heating profiles in the magnet have been

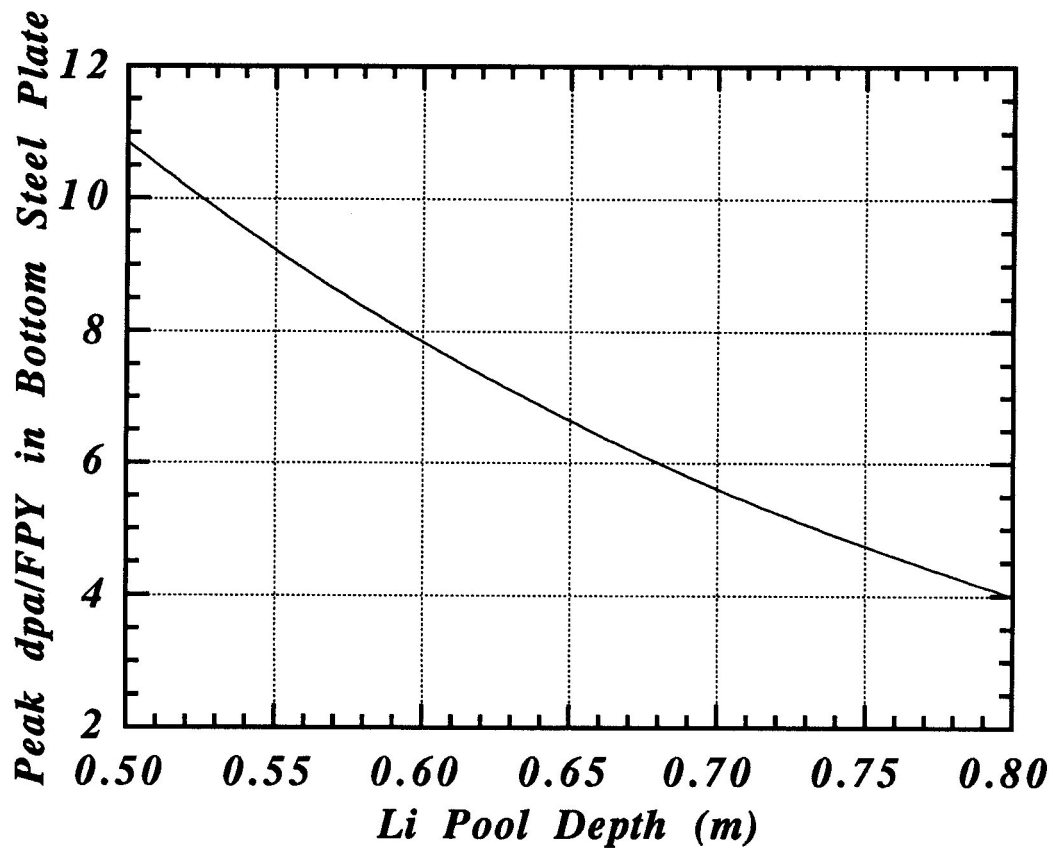


Figure 14.6. Effect of Li pool depth on damage in bottom steel plate.

determined for use in the thermal hydraulics analysis. The nuclear heating deposited in each magnet is 3.87 MW with the peak power density being 191 W/cm³ in the front casing.

14.6. Biological Shield Design

The reactor shield is designed such that the occupational biological dose rate outside the shield does not exceed 2.5 mrem/hr during reactor operation. The biological shield consists of 70 vol.% concrete, 20 vol.% carbon steel C1020 and 10 vol.% He coolant. Figure 14.8 gives the dose rate at the back of the shield at the reactor midplane as a function of shield thickness. A 2.6 m thick shield is required to yield an acceptable operational dose rate of 2.5 mrem/hr. Similar calculations performed for the chamber roof indicate that the biological shield thickness above the roof should be 2.75 m thick.

Table 14.1. Neutronics Parameters for the Different Regions of LIBRA-LiTE

Coolant/breeder	Liquid Li
Lithium enrichment	7.42% ^6Li
<u>Blanket</u>	
Chamber wall radius	5.7 m
Inner radius of blanket	3.45 m
Neutron wall loading	10.6 MW/m ²
TBR	1.504
M_n	1.242
Peak INPORT dpa rate	68 dpa/FPY
Peak INPORT He production rate	602 He appm/FPY
Power density in the front INPORT tube	23.3 W/cm ³
Minimum INPORT lifetime	2.2 FPY
Peak chamber wall dpa rate	5 dpa/FPY
Peak chamber wall He production rate	18.8 He appm/FPY
Peak power density in chamber wall	4.8 W/cm ³
Chamber wall lifetime	30 FPY
<u>Roof</u>	
Distance from target	16 m
Thickness	0.5 m
Neutron wall loading	0.49 MW/m ²
TBR	0.558
M_n	1.299
Peak dpa rate	5 dpa/FPY
Peak He production rate	28 He appm/FPY
Lifetime	30 FPY
<u>Bottom</u>	
Distance of pool surface from target	5 m
Li pool depth	0.75 m
TBR	1.575
M_n	1.221
Peak dpa rate in steel plate	5 dpa/FPY
Peak He production rate in steel plate	22 He appm/FPY
Lifetime	30 FPY

Table 14.1. (Continued)

<u>Magnets</u>	
Distance of magnet front from target	2.05 m
Magnet length	0.5 m
Neutron wall loading	29 MW/m ²
TBR	1.017
M _n	1.034
Peak dpa rate	200 dpa/FPY
Peak He production rate	1700 He appm/FPY
Peak power density in front case	191 W/cm ³
Peak power density in Li	88 W/cm ³
Nuclear heating per magnet	3.87 MW
Lifetime	0.75 FPY
<u>Biological Shield</u>	
Thickness at midplane	2.6 m
Thickness above roof	2.75 m
Operational dose rate at back of shield	2.5 mrem/hr

Table 14.2. Overall Reactor Tritium Breeding Ratio and Energy Multiplication

Region	Coverage Fraction	TBR	M _n
INPORT	77.52%	1.504	1.242
Beam ports	1.45%	0	0
Magnets	7.03%	1.017	1.034
Roof	5.15%	0.558	1.299
Bottom	8.85%	1.575	1.221
Total reactor	100%	1.405	1.211

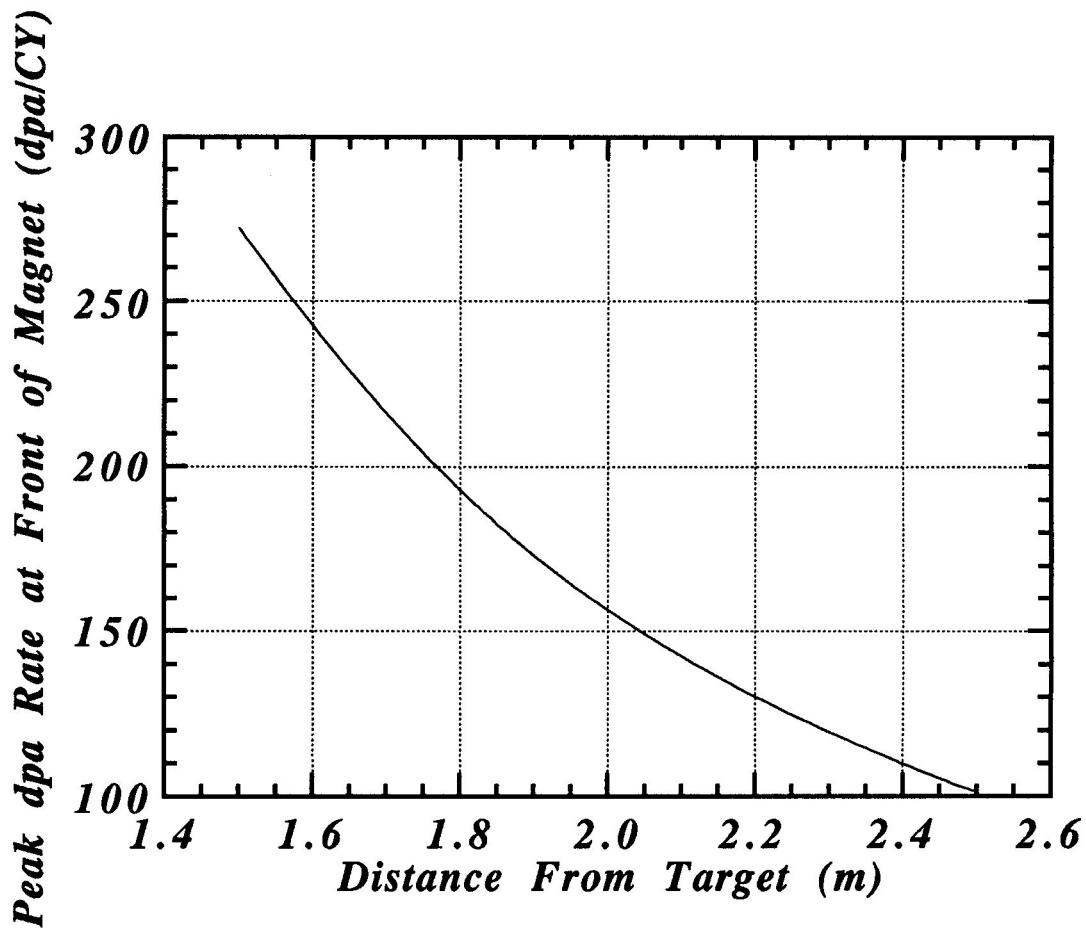


Figure 14.7. Peak damage rate in magnet as a function of distance from target.

14.7. Overall Reactor Neutronics Parameters

Table 14.1 lists the main neutronics parameters for the different regions of the reactor chamber. Using the coverage fractions and local nuclear parameters calculated for the different reactor regions surrounding the target, the overall reactor TBR and M_n can be determined. The results given in Table 14.2 indicate that the overall TBR and M_n values in LIBRA-LiTE are 1.405 and 1.211, respectively. Taking into account surface heating by the x-rays and debris, the overall reactor energy multiplication, defined as the ratio of the total power deposited by x-rays, debris, neutrons and gamma photons to the fusion power, is 1.123.

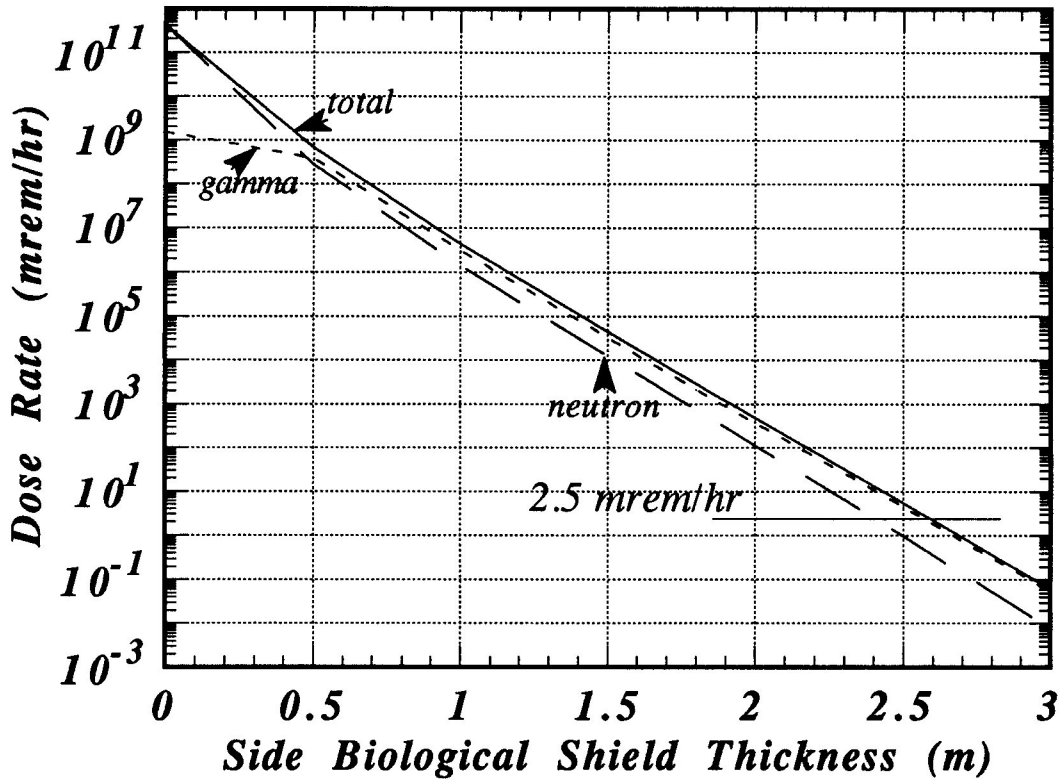


Figure 14.8. Effect of side biological shield thickness on dose rate during reactor operation.

14.8. Neutronics Performance with Lithium Lead

The option of using the $\text{Li}_{17}\text{Pb}_{83}$ eutectic as a coolant and breeder instead of liquid lithium has been considered. This is motivated mainly by the need to avoid safety concerns related to the possibility of having a lithium fire and a high tritium inventory in the coolant. The impact of using $\text{Li}_{17}\text{Pb}_{83}$ on the neutronics performance of LIBRA-LiTE has been assessed. Figure 14.9 shows the impact of blanket thickness and lithium enrichment on the local TBR in the INPORT units and the damage rate in the chamber wall for the case when $\text{Li}_{17}\text{Pb}_{83}$ is utilized as a coolant and breeder. The results indicate that a 1.7 m thick blanket with a lithium enrichment of 90% ^6Li should be used. Even though the front surface of the INPORT units will be at 4 m from the target compared to 3.45 m in the lithium case, the lifetime of the INPORT units is reduced by 27% due to neutron multiplication in the lead. Neutronics calculations for the final focusing magnets indicate also that the magnet lifetime is reduced by 43% when $\text{Li}_{17}\text{Pb}_{83}$ is used. Table 14.3 gives a comparison between the neutronics related parameters obtained using Li or $\text{Li}_{17}\text{Pb}_{83}$ in LIBRA-LiTE. While using $\text{Li}_{17}\text{Pb}_{83}$ results in nearly the

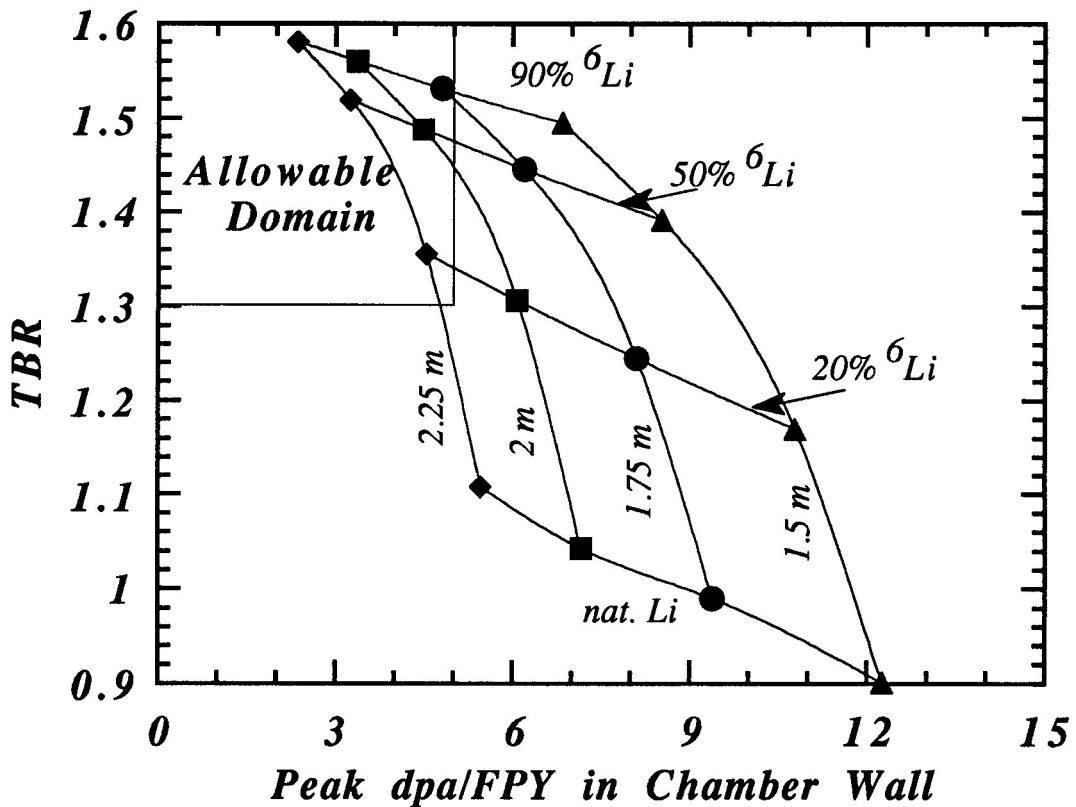


Figure 14.9. TBR and chamber wall damage rate for different blanket designs utilizing $\text{Li}_{17}\text{Pb}_{83}$ as the coolant and breeder.

same overall TBR and M, the lifetimes of the INPORT units and final focusing magnets are reduced, a slightly bigger roof should be used, and more expensive highly enriched lithium must be used. Based on these results and other considerations related to the larger magnet power, lower repetition rate and larger weight associated with using $\text{Li}_{17}\text{Pb}_{83}$, liquid lithium is chosen as the reference coolant and breeder in LIBRA-LiTE as explained in Chapter 10.

References

- [1] R. O'Dell et al., "User's Manual for ONEDANT: A Code Package for One-Dimensional, Diffusion-Accelerated, Neutral Particle Transport," Los Alamos National Laboratory, LA-9184-M, 1982.
- [2] B. Badger, et al., "LIBRA - A Light Ion Beam Fusion Conceptual Reactor Design," University of Wisconsin Fusion Technology Institute Report UWFD-800, 1989.

Table 14.3. Neutronics Parameters for LiPb vs. Li

	Li	LiPb
Percent ^6Li	7.42	90
Blanket thickness (m)	2.25	1.7
Inner radius of blanket (m)	3.45	4
INPORT lifetime (CY)	3	2.2
Magnet lifetime (CY)	1	0.57
Roof distance from target (m)	16	17
Pool depth (m)	0.75	0.55
Overall TBR	1.405	1.415
Overall energy multiplication	1.123	1.144

15. Tritium Systems

The tritium subsystems within the reactor complex are identified and their tritium inventories located within the various reactor systems are assessed. Such information is needed in order to evaluate the potential radiological hazards due to tritium releases during normal and off-normal operations, as summarized in Table 15.1.

15.1. Tritium Fuel Preparation

The fuel targets are prepared in a target fabrication facility which is separated from the reactor facility. The proposed fuel targets consist of a three-layer structure of spherical shells, 6.20 mm O.D. The interior surface of a polymeric shell contains 3.55 mg of tritium (T) and 2.37 mg of deuterium (D) per target. This polymeric shell is overcoated with a Pb shell. At a fueling rate of 3.9 Hz nearly 337,000 targets are required per full power day. The targets are filled in a high pressure box containing 93 g(T), as previously described [1]. As part of the process, filled targets must be stored as batches in a cryogenic refrigerator for two hours, which would contain ~ 100 g(T). The total tritium in the processing system would be 193 g(T). Additionally, a one-day's supply of filled targets would be stored in a refrigerated vault, containing ~ 1200 g(T). As needed these pellets are transferred to a storage chamber adjacent to the pellet injector, which will contain a one hours's supply, 50 g(T).

15.2. Tritium Breeding and Recovery

Liquid Li serves as the reactor coolant and neutron absorber to produce tritium. All of the Li flowing throughout the reactor exits through the sump pump at the floor of the reactor. At the pellet fueling rate of 3.9 Hz and a breeding ratio of 1.38, 5.76 mg(T)/s is generated in the Li. In addition, only 30% of the D/T is consumed during the ignition of the pellet in the reactor chamber. As a result, the unburned fuel accumulates in the chamber and eventually condenses in the Li pool at the floor at the rate of 9.67 mg(T)/s. At a Li flow rate of 3.77×10^3 kg/s, the total concentration of T in the Li increases at the rate of 4.09×10^{-3} wppm/s.

It is necessary to remove the buildup of T in the Li by diverting a portion of the flowing Li to a Tritium Removal System. For this study, the TRS utilized the extraction of T from the Li to a fused salt system with the subsequent recovery of T₂ from the fused salt by electrochemical methods [2]. Such a system has demonstrated $> 90\%$ T removal efficiency. The quantity of Li(T) bypassed to the TRS depends upon the permissible concentration of T in Li so that the diffusion of T₂ at the intermediate heat exchanger does not exceed the guidelines for T₂ release to the environment. At a T concentration of 1 ppm (0.5 wppm) in the Li, the T₂ pressure

is 7×10^{-8} Pa at the average IHX temperature of 425°C. The IHX would have a surface area of 722 m² with tubes of 1 mm wall thickness; consequently, the T₂ diffusion at the IHX would be only 14 Ci/day. In order to maintain the concentration of 1 appm T in Li only 30 liters/s (0.4%) of the total Li flow must be diverted to the TRS. The total weight of Li in the reactor and auxiliary systems is ~ 460 Mg; consequently, at a concentration of 0.5 wppm(T), the total tritium inventory in the Li would be 230 g.

15.3. Evaluation of Tritium Inventories and Release Rates

The tritium inventories which are given in Table 15.1 for the target fabrication facility and the reactor hall have been previously discussed except for the exhaust chamber vacuum system. For this system it was assumed that the exhaust ejected from the chamber contained $\sim 10\%$ of the unburned T in the gas phase (~ 1 mg/s), existing principally as the molecule LiT. When this species contacts the molten lead in the surge tank, gaseous T₂ will be released and pumped to a tritium recovery system which accumulates tritium for two hours, yielding an inventory of ~ 7 g. The breeder TRS would have ~ 2 min contact time for the liquid Li with the fused salt and a similar amount in the electrochemical cell for a total inventory of 4 g(T). The product from this cleanup scheme should contain only gaseous hydrogenic species and can go directly to the cryogenic distillation system. The distillation system must isotopically separate 366 mole/day of DT. Based upon previous experience at TSTA, the tritium inventory in the distillation system would be 70 g; however, recent optimization studies [3] have indicated that the inventory can be diminished by 50%, to ~ 35 g(T).

The routine release from the several processing systems in LIBRA-LiTE is estimated based upon recent experiences at TSTA [4] which indicated that only 1.5 Ci were released through the stack during the processing of 100 g of T for 38 hr, ~ 1 Ci/d/100 g(T). Based upon these findings and the processing rates required in the LIBRA-LiTE facilities, a release of ~ 12 Ci/d would be expected from the target fabrication facility, and 17 Ci/d each from the reactor hall and fuel processing facility, as given in Table 15.1. The total tritium release to the air would be ~ 46 Ci/d. In addition, ~ 14 Ci/d of T would permeate through the intermediate heat exchanger into the Pb intermediate fluid. Because no tritium removal system exists in the Pb circuit, the loss of tritium to the steam cycle would reach the same steady state value. Based upon the environmental analysis in LIBRA [1], this routine tritium release from a 100 m stack subjects the most exposed individual at 100 m from the site to a dose of $\sim 3 \times 10^{-5}$ Sv/y (3 mrem/y) which is below the German Radiation Protection Guideline of 3×10^{-4} Sv/y (30 mrem/y).

The potential accidental releases of tritium are listed in Table 15.1 based upon the inventory of tritium in each of the subsystems and the probability of each subsystem to fail. For instance, the probability of tritium being released from the two storage vaults (the inactive storage vault and the cryogenic pellet storage vault) is very small and not considered as a conceivable event. The cryogenic pellet storage vault would be connected to a large evacuated chamber containing tritium getter materials which would absorb the tritium and prevent release in the event that the cryogenic refrigerator failed.

A conceivable accidental event would be a fire involving the liquid Li followed by a breach in the containment structure. Such an event would release all the T in Li, 230 g, plus the tritium in the associated system; namely, the exhaust chamber vacuum system (7 g), the fuel cleanup system (4 g) and the fuel targets in the fuel injector (50 g). A total of 291 g of T might be involved, therefore, in a puff release (2 hr). This release would probably be vented from the top of the building, ~ 50 m high. Based upon the environmental analysis given in LIBRA if all the tritium were in the HTO form, the maximum dose would be 15×10^{-3} Sv (1.5 Rem) to the most exposed individual at 300 m from the site. This dose is well below the 25 Rem guideline required by the U.S. Nuclear Regulatory Commission to require an evacuation of the neighborhood. A complete analysis of such an event would require an analysis of the other radioactive isotopes which would be released in addition to the tritium; however, the radiological hazard due to the contained tritium does not appear as a limiting safety concern in the siting of this power plant.

References

- [1] B. Badger, et al., "LIBRA - A Light Ion Beam Fusion Conceptual Reactor Design," University of Wisconsin Fusion Technology Institute Report UWFDM-800, KfK-4710, 1989.
- [2] W. F. Calaway, "Electrochemical Extraction of Hydrogen from Molten LiF-LiCl-LiBr and Its Application to Liquid-Lithium Fusion Reactor Blanket Processing," *Nuclear Technology*, **39**, 63 (1978).
- [3] R. H. Sherman, Los Alamos National Laboratory, private communication, Oct. 1991.
- [4] J. L. Anderson, et al., "Experience of TSTA Milestone Runs with 100 Grams-Level of Tritium," *Fusion Technology*, **14**, 438 (1988).

Table 15.1. Tritium Inventory and Release

Location	System	Inventory T, g	Release	
			Routine Ci/d	Accident T, g
Target Fabrication Facility			12	
	In-process	193		193
	Storage (1 day)	1200		0
Reactor Hall			17	
	Fuel targets (1 hr)	50		50*
	Breeder alloy	230		230*
	Exhaust chamber	7		7*
Fuel Processing			17	
	Fuel cleanup	4		4*
	Isotope separation	35		35
Storage	Inactive (2 day)	2500	0	0
Steam Generator	Water	-	14	-
Total		4219	46 (air) 14 (water)	291*

*Largest conceivable release.

16. Heat Transfer

16.1. Introduction

The thermal hydraulics of the final focus magnet is discussed in detail in Chapter 8. Here, only the thermal hydraulics performance of the INPORT tubes will be discussed.

16.2. Geometry

The INPORT units in the LIBRA-LiTE blanket have the configuration of a concentric cylindrical shape surrounding the target at the center of the reactor chamber. The general shape of the reactor chamber is a mushroom-like configuration, the stem being the INPORT units and the head is the roof (Fig. 16.1). The INPORT units consist of two groups, front and secondary; both are made of vertical austenitic stainless steel, low activation HT-9 tubing. A detailed description of these two groups follows:

- First group: The front group consists of three concentric rows of woven metallic tubing. The woven walls of this system of tubing allow the internal coolant/breeder fluid to seep through the woven walls and wet the outer surface of the tube. The lithium wetted wall is designed to protect the metallic material from x-rays, charged particles and target/reaction debris.
- Second group: The secondary tubes consist of 14 concentric rows of solid HT-9 tubing. They are relatively colder than the rest of the reactor. It is expected that the lithium vapor will recondense on the outer secondary tube surfaces. The general parameters for the INPORT unit geometry are as follow (Fig. 16.2 and Fig. 16.3):

<u>The front group</u>	
Number of rows	3
Number of tubes/row	218
Total number of tubes	654
Diameter of each tube (cm)	5.0
Diameter of the first row (cm)	345.0

<u>The secondary group</u>	
Number of rows	14
Number of tubes/row	122
Total number of tubes	1708
Diameter of each tube (cm)	12.0
Diameter of the first row (cm)	380.0

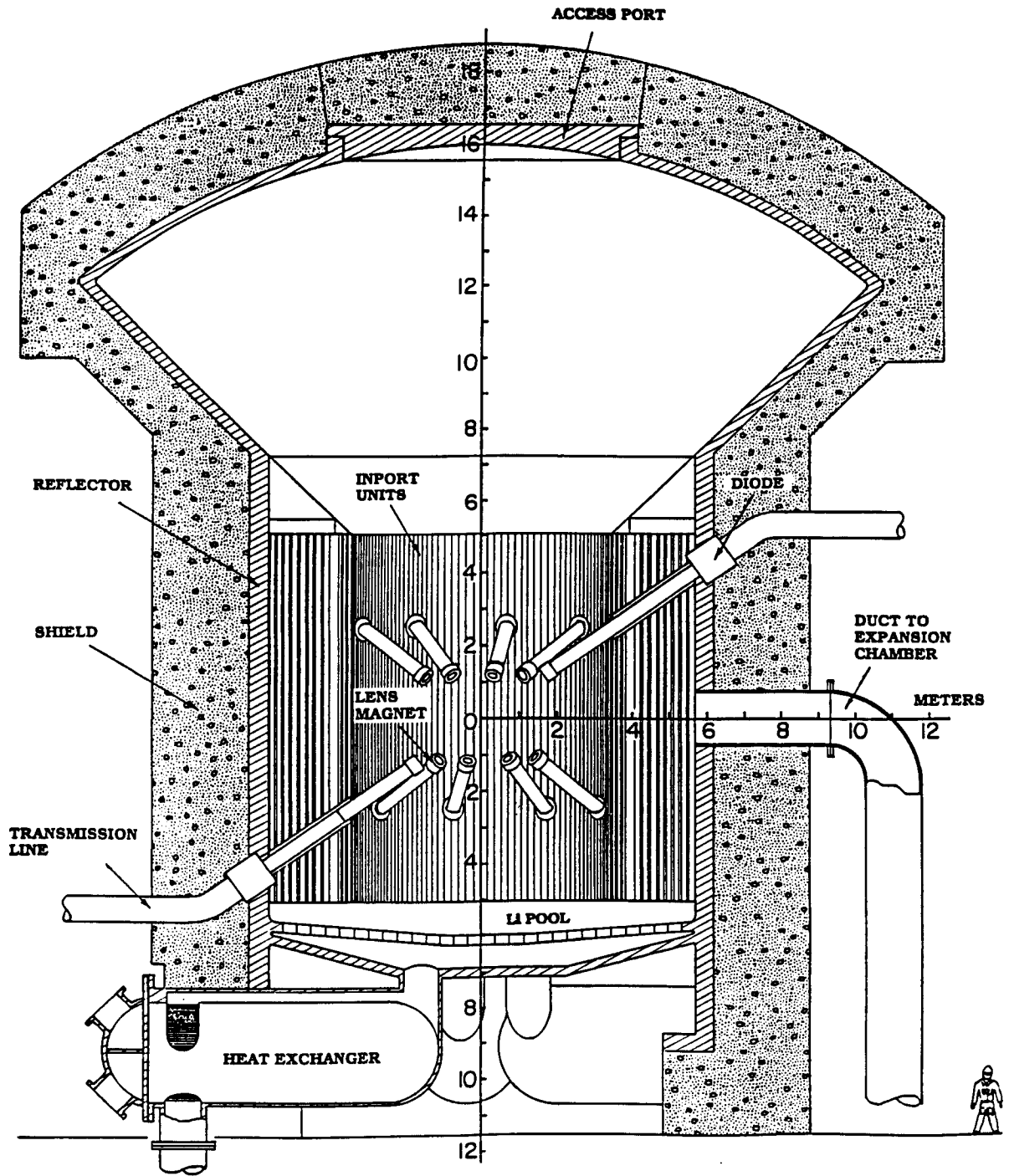


Figure 16.1. A general cross-sectional view of the LIBRA-LiTE chamber.

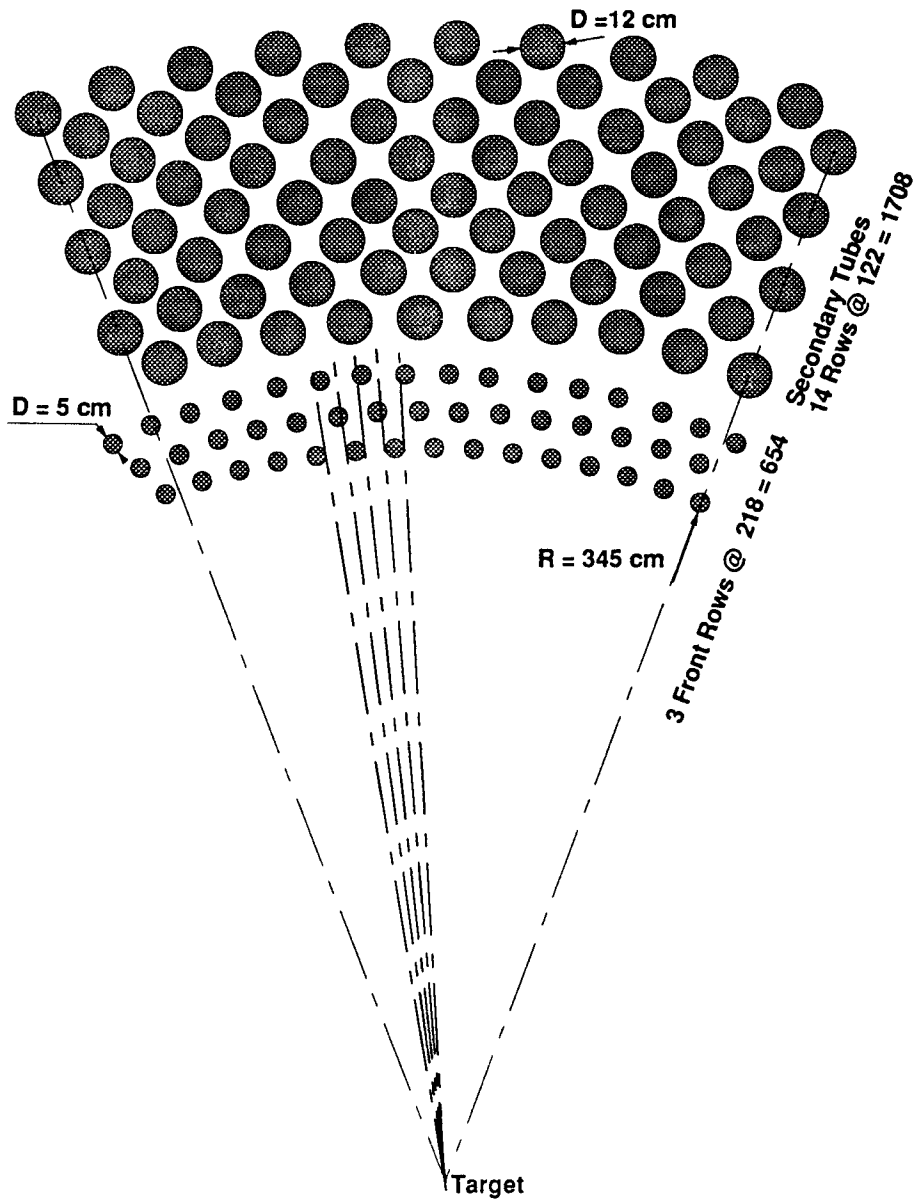


Figure 16.2. A general layout of the INPORT units in the LIBRA-LiTE chamber.

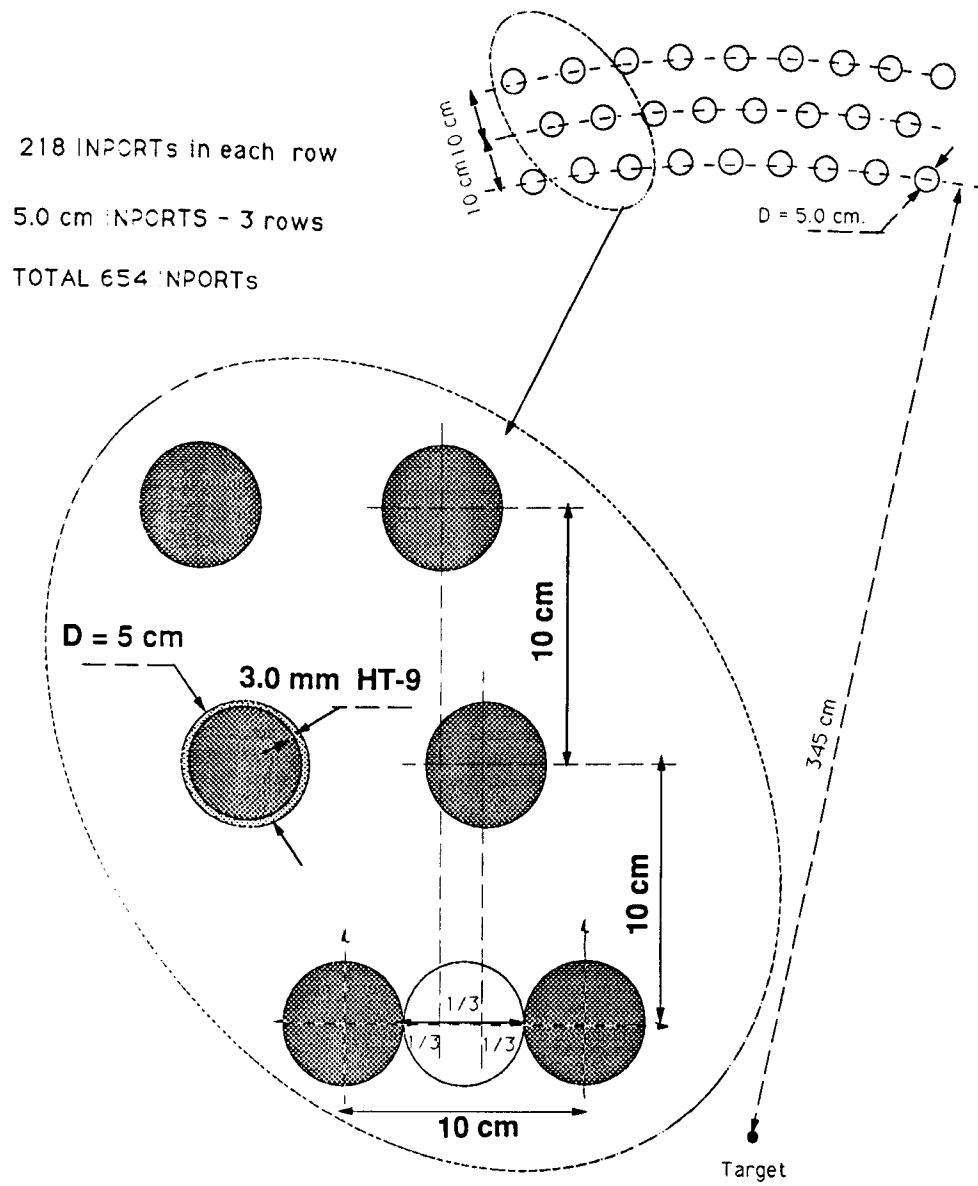


Figure 16.3. A general view of the first row INPORT arrangement in the LIBRA-LiTE chamber.

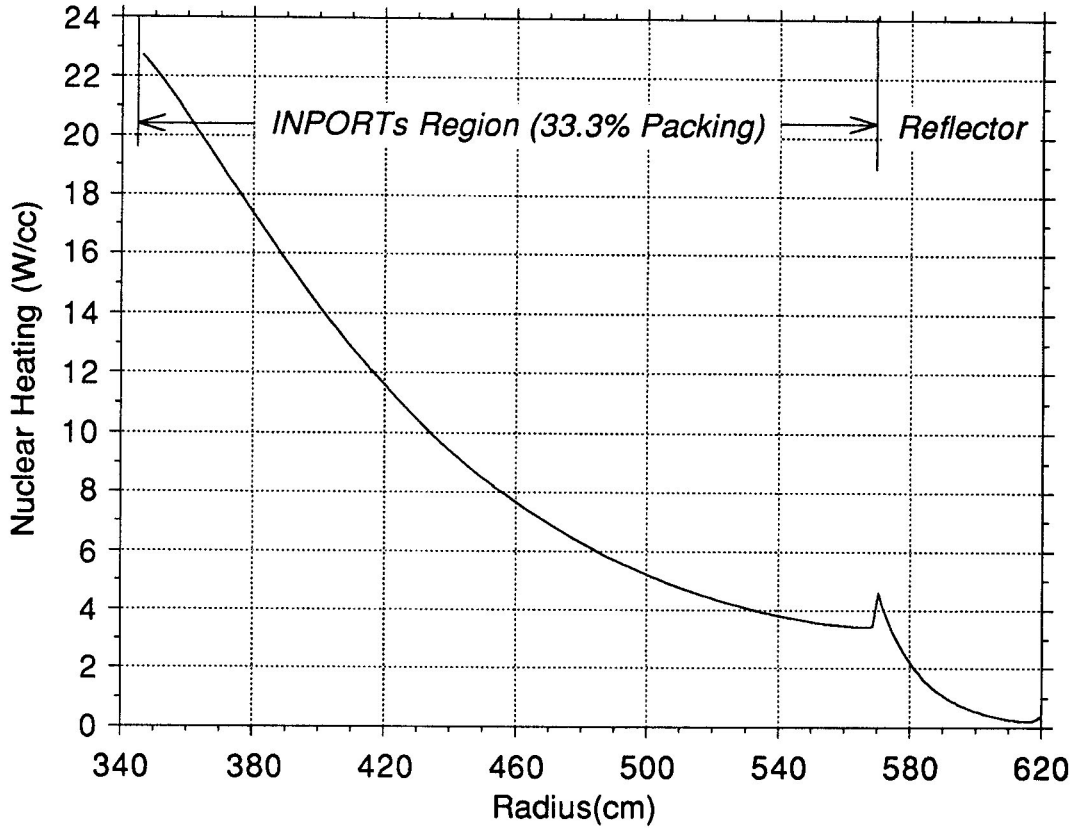


Figure 16.4. Steady state nuclear heating distribution in LIBRA-LiTE INPORTs and reflector.

16.3. Thermal Hydraulics Calculations

Neutronics analysis is performed utilizing a one-dimensional model to calculate the distribution of the volumetric nuclear heating in the blanket (INPORT unit). Also, a one-dimensional hydrodynamics calculation is executed to determine the cavity performance and to account for the effects of vaporization/condensation processes on the surface heat flux. The following is a steady state parameter list:

Peak nuclear volumetric heating in front metal (W/cm ³)	46.0
Peak nuclear volumetric heating in front Li (W/cm ³)	22.2
Average nuclear volumetric heating in front tube (W/cm ³)	22.4
Maximum surface heat flux at midplane (W/cm ²)	171.6
Minimum surface heat flux at the upper/lower end (W/cm ²)	25.5
Average surface heat flux (W/cm ²)	77.7

The steady state nuclear heating distribution at the midplane is shown in Fig. 16.4. For thermal hydraulics calculations consider the following thermal assumptions:

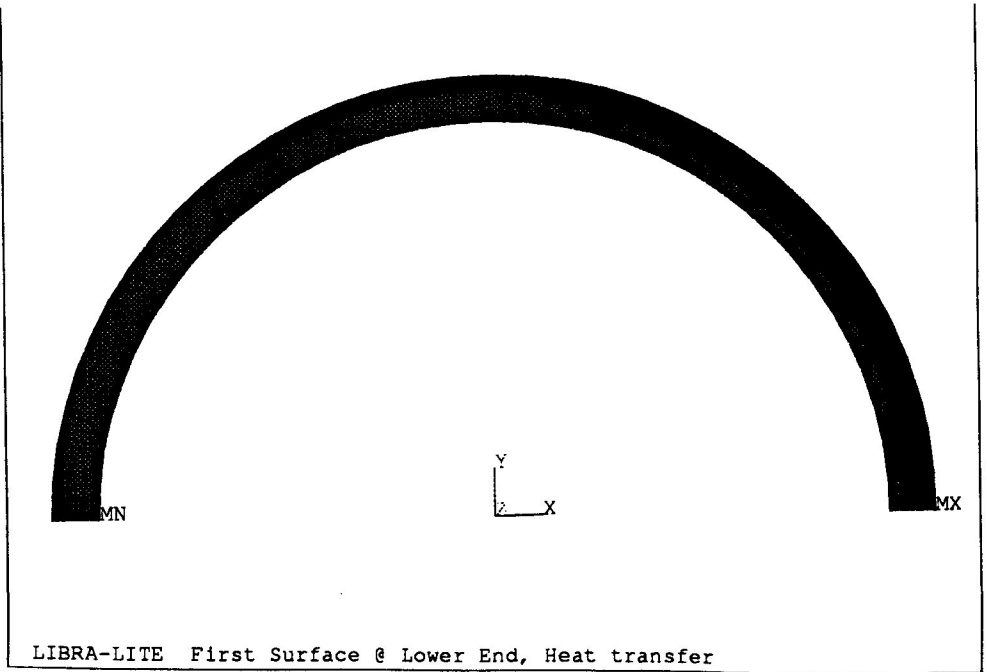
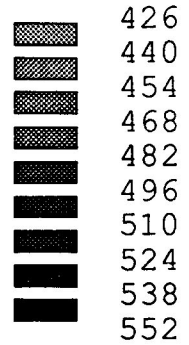
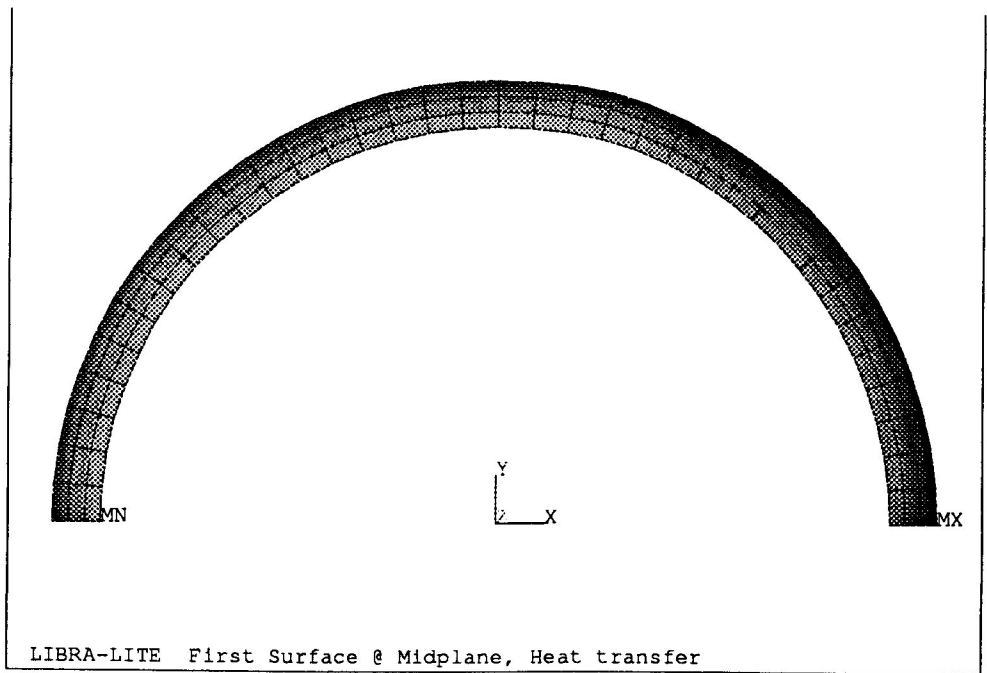


Figure 16.5. The temperature distribution in the first row tubing.

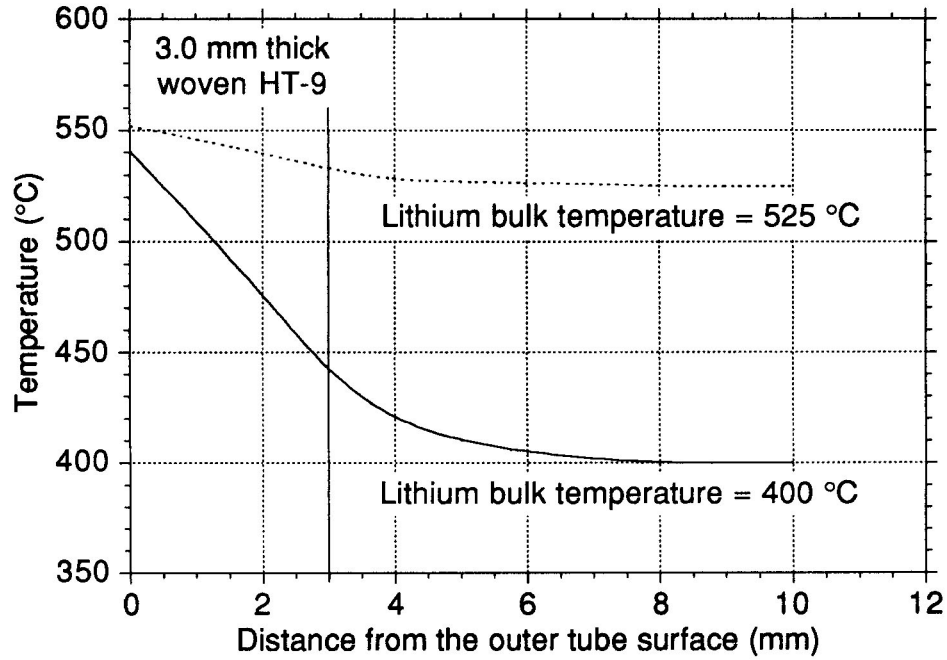


Figure 16.6. The temperature distribution at the midplane and the lower end at the front of one of the first row tubes.

Inlet coolant temperature	275°C
Outlet temperature	525°C
Coolant temperature rise	250°C
Average coolant temperature	400°C

By using these parameters the following results are obtained:

First row tubes

Average coolant velocity (m/s)	1.53
Maximum coolant velocity (m/s)	2.09
Volumetric flow rate/tube (m ³ /s)	3.0×10^{-3}
Total volumetric flow rate/first 3 rows (m ³ /s)	1.967
Total mass flow rate/first 3 rows (kg/s)	983

Secondary row tubes

Maximum coolant velocity (m/s)	0.26
Maximum Volumetric flow rate/tube (m ³ /s)	2.94×10^{-3}
Total average volumetric flow rate/14 rows (m ³ /s)	2.63
Total mass flow rate/14 rows (kg/s)	1316.6

INPORT unit tubing

Total lithium volumetric flow rate in the INPORT unit (m ³ /s)	4.8
Total lithium mass flow rate in the INPORT unit (kg/s)	2.3×10^3

A two-dimensional thermal model of the first row tubes is furnished for use with ANSYS (ANSYS is a commercial computer code capable of handling thermal and stress analysis applications using the finite-element method) to calculate the temperature distribution in the first row tubes. Because of the symmetry in the heat loads on each tube, only half of a front tube is modeled. Two cases of the calculated temperature distribution in the first row tubes are shown in Fig. 16.5. The first case is at the midplane, where the coolant is at the average temperature of 400°C. The second case is at the lower end of the tube, where the coolant is at the maximum temperature of 525°C. The value used for the heat transfer coefficient in both cases is 2.65 W/cm² K. The following is a summary of the results:

	<u>First Midplane</u>	<u>Second Lower End</u>
Liquid lithium temperature (°C)	400	525
Maximum temperature of HT-9 (°C)	540.6	551.9
Minimum temperature of HT-9 (°C)	426.5	528.6
Average temperature of HT-9 (°C)	483.5	540.3

Figure 16.6 shows the temperature distribution at the midplane and lower end at the front of one of the first row tubes.

17. Power Cycle

17.1. Introduction

The power cycle in LIBRA-LiTE utilizes a liquid lead-lithium intermediate loop to transfer the thermal energy from Li to the steam. This arrangement minimizes the possibility of Li-water interaction. It also minimizes the tritium diffusion into the steam. The heat exchangers are built into the base of the target chamber. The Li flows from the bottom of the pool to the heat exchangers. A counterflow configuration is utilized in the heat exchanger between Li and LiPb. The LiPb enters at 255°C and exits at 500°C. A two reheat stage superheated steam power cycle is proposed, with the steam temperature at 480°C and steam pressure 24 MPa. With these parameters the gross thermal efficiency is 44%. Figure 17.1 is a power flow diagram for LIBRA-LiTE. The figure shows that a total energy of 2340 MW is released from the target. A loss of 48.9 MW due to endoergic reactions leaves 699 MW from x-rays and 1592 MW from neutrons and gammas. The blanket energy multiplication is 1.211. The total thermal energy, including Li and Pb pump heating, and heat generated in the magnet leads (75 MW), is equal to 2710 MW. The gross electric power generated at 44% efficiency is 1192 MWe of which 192 is needed to run the plant (e.g. driver and magnet). A net electric power of 1000 MWe is available for use making the overall plant efficiency 36.9%. The following table gives the power cycle parameters for LIBRA-LiTE:

Lithium inlet temperature (°C)	275
Lithium outlet temperature (°C)	525
Lithium mass flow rate (kg/s)	2580
LiPb inlet temperature (°C)	255
LiPb outlet temperature (°C)	480
LiPb mass flow rate (kg/s)	6.4×10^4
Steam temperature (°C)	460
Steam pressure (MPa)	24
Gross thermal conversion efficiency	44%
Gross electric power generated (MW)	1192
Net plant efficiency	36.9%
Net electric power generated (MWe)	1000

18. Maintenance

A critical aspect of the LIBRA-LiTE reactor is the ability to maintain reactor components both internal and external. In this chapter the maintenance of the final focusing magnets, the INPORT units and the drivers is discussed.

18.1. Final Focusing Magnets and Front INPORT Units

The proximity of the final focusing (FF) magnets to the target makes them especially vulnerable to damage by the neutrons. In particular, damage to the spinel ($\text{MgO}\cdot\text{Al}_2\text{O}_3$) electrical insulation will determine the lifetime of these magnets. In the past, the criterion for determining the limits for insulators has been the swelling. In spinel, 4% swelling is reached at a fluence of 4×10^{22} n/cm². For conventionally wound magnets with turn to turn insulation between solid conductors, this is very critical. However, for the type of magnets used in the final focusing system in LIBRA-LiTE, the swelling is not as critical. Here the insulation separates the ducts which carry the liquid Li through the magnet from the outer casing. The outer casing is a thick (0.5 cm) plate of HT-9, the inner duct wall is a thin sheet (0.1 cm) of HT-9, and the insulation is sandwiched between them. Swelling of this insulation will put the inner duct wall in compression. Since the voltage that exists between turns is on the order of one volt, the requirement on the insulation is not severe. If it is assumed that a ceramic coating on the inner channel ducts is 0.5 mm, even a 10% swelling will have a minimal effect on the duct wall. A more critical limit is when the insulation essentially disintegrates into a powder. This limit is not known, but is likely to be an order of magnitude higher than the 4% swelling limit currently used for spinel. If a damage criterion for HT-9 of 150 dpa is used, this occurs at a fluence of 1.5×10^{23} n/cm², or one calendar year of operation in the reactor. This fluence is only a factor of four times higher than the 4% swelling limit in spinel. For the present, it is assumed that the lifetime of the FF magnets will be one calendar year.

The FF magnets are integrated into the frame which supports the front rows of INPORT units. The frame is made of HT-9 and consists of solid tubes located in the first row of large tubes. These solid tubes hold apart the upper plenums feeding the INPORT units and the lower assembly to which the units are attached. The beam tubes are designed to come apart at the interface between the front INPORT units and the rear units. The front ends of the beam tubes are attached to the frame. However, when the beam tubes are disconnected, the FF magnets have to be supported. This is accomplished with the aid of a fixture inserted into the reactor at the time of FF magnet changeout. The fixture supports the magnets while the beam tubes are disconnected and has the tools needed to perform the task integrated into it.

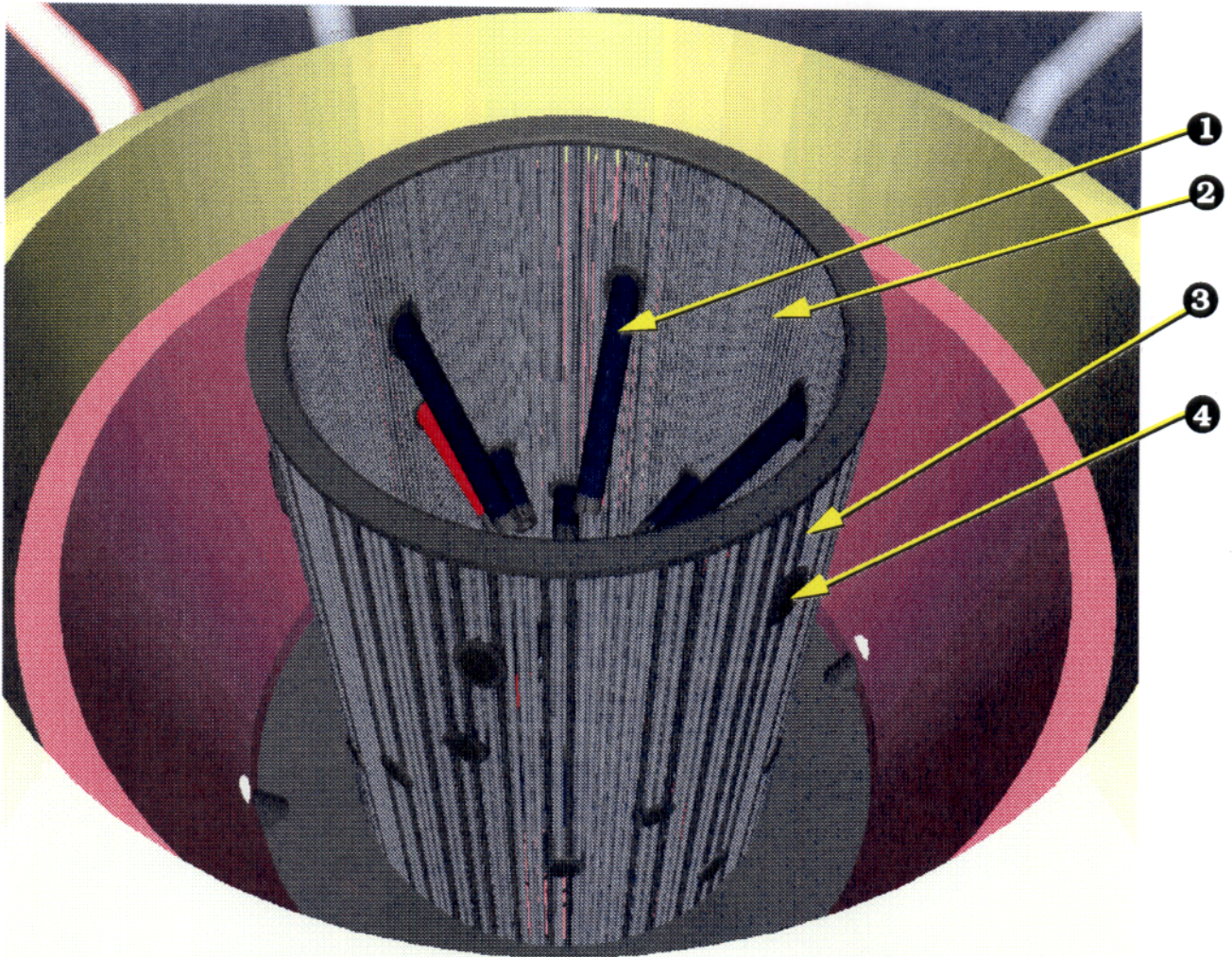
Figure 18.1 shows the FF magnets and the front rows of INPORT units being taken out of the reactor. The following sequence is needed to perform this task:

- The roof shield is disassembled and removed in sections.
- The chamber cover is unbolted and removed as a unit.
- Coolant lines to the plenum feeding the front INPORT units are disconnected.
- A fixture is inserted into the reactor. The fixture supports the magnets while inserting a tool into the bore of a beam tube to disconnect it. This is repeated until all the beam tubes are taken apart.
- The fixture and the support frame are removed from the reactor as a single unit and taken to a hot cell. In the hot cell the magnets are replaced with new assemblies including beam lines up to the joint with the original beam line.
- A spare fixture and frame complete with front INPORT units and a new set of magnets is then guided into the reactor and located on dowels. The beam lines are individually reconnected. The fixture is removed.
- The coolant lines are reconnected and the roof assembly replaced.

The front INPORT units have a lifetime of three calendar years and they would be replaced every third time that particular frame had been in the reactor. The sequence will be as described above.

18.2. Rear INPORT Units

The rear INPORT units starting with the second row of large tubes have a lifetime of four calendar years. The radiation damage in succeeding rows falls off rapidly and the last row needs no replacing during the lifetime of the reactor. However, to maintain the integrity of these units, periodic replacement will be made of the front rows of the rear tubes. For ease of maintenance, the rear INPORT units have been divided into eight groups, or two groups per chamber quadrant. Each group (or octant) is designed as a standalone assembly. This means that the tubes in the rear rows of the assemblies are solid and can provide the rigidity needed to make the assemblies self-supporting. Since these rear rows receive little radiation damage, they can be counted on for structural support. Two octants of rear tube units will be replaced every year starting with the fourth year. They will be replaced at the same time the



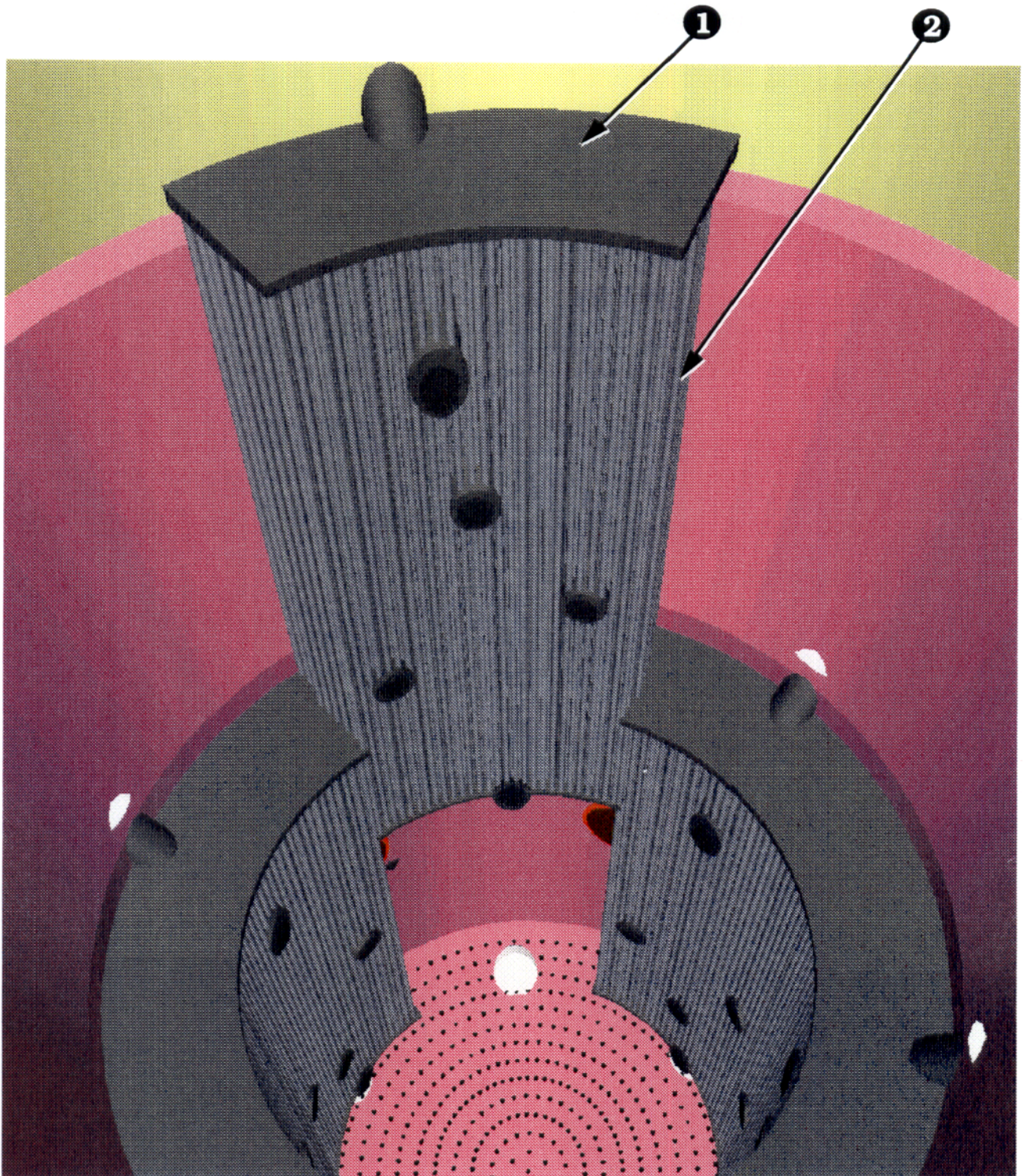
- (1) Final focusing magnet support
- (2) Front INPORT units
- (3) Support tube
- (4) LI shunt manifold around beam line

Figure 18.1. View showing the removal of front INPORT units and the final focusing magnets.

FF magnets are replaced. Figure 18.2 shows one of the octants being removed from the reactor. This would occur in the sequence right after the FF magnets and integral front INPORT units have been removed. To save time, there will be two spare octants which have been previously reconditioned, ready to take the place of the removed ones.

18.3. Driver Modules

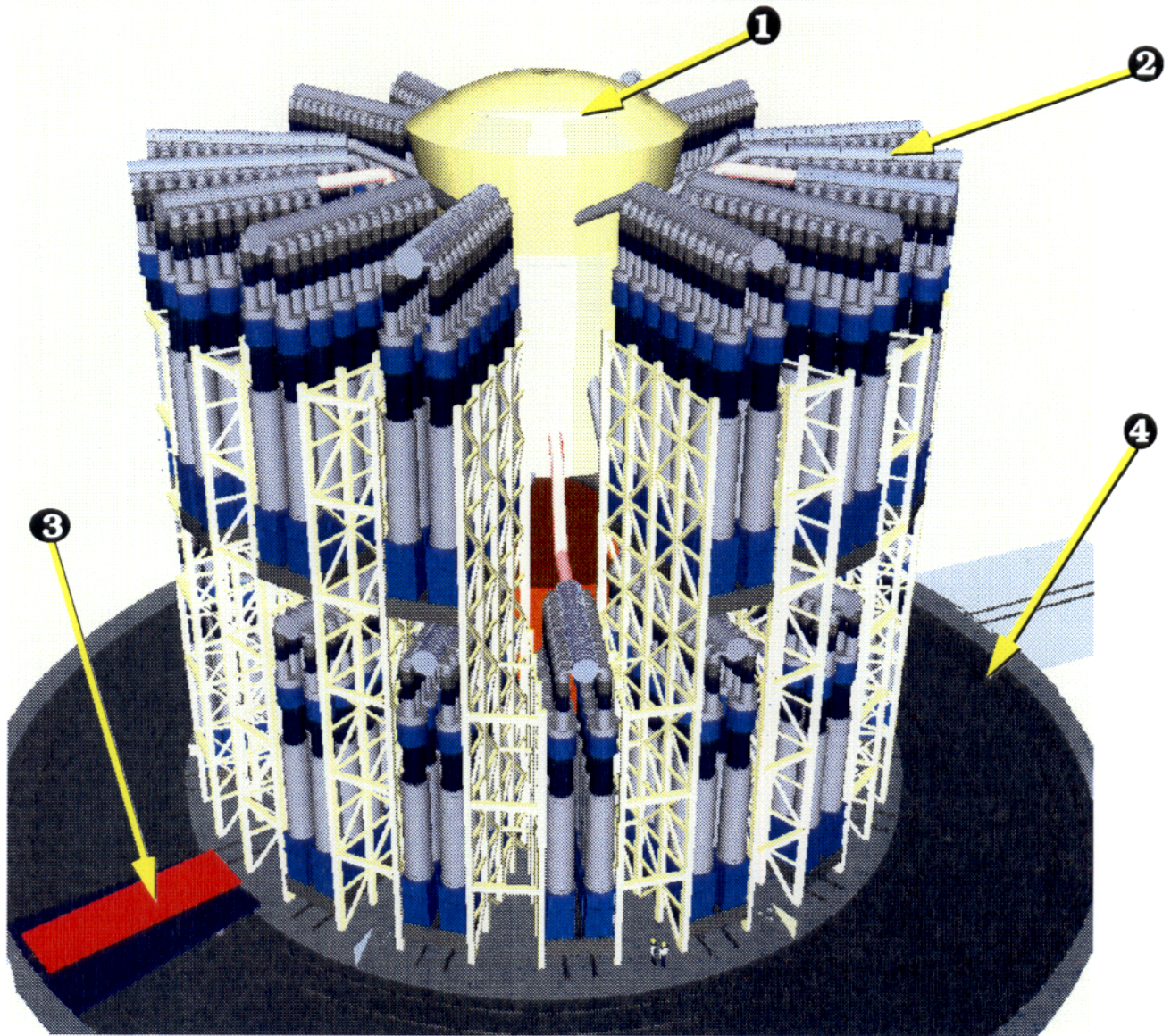
There are thirty driver modules in the reactor distributed around the chamber in eighteen equal sectors. Twelve of the sectors have tandem drivers and six have only one. Further, of the six sectors with only one driver, three have drivers on the bottom level and three on the top. Figure 18.3 is a side view of the chamber and drivers. This view also shows a set of circumferential rails surrounding the reactor on the outer periphery. Several carriages are able to use the rails simultaneously. These carriages are designed to go underneath a lower level module, lift it up, then retract radially back onto the circumferential rails and then transport the module to a hot cell where it can be serviced. Upper level modules are independently supported on the tandem frame. In order to remove an upper level module, the lower level module has to be removed first, then the upper level module lowered down onto another carriage for extraction and transport to the hot cell. The details of how to disengage the pulsed power line from the driver during these operations have not been worked out. Figure 18.4 shows a lower driver module being transported on the rails to a hot cell. It is significant to note that if all the fluids are drained from the driver it still has a mass of about 1000 tonnes. The carriage and the rails will have to be specially designed to be able to transport such a large mass.



(1) Rear INPORT Units' Assembly Being Removed from Reactor

(2) Rear INPORT Units

Figure 18.2. View showing the removal of an octant of rear INPORT units.



- (1) Reactor chamber
- (2) Driver
- (3) Transport carriage
- (4) Circumferential rails

Figure 18.3. Side view of reactor with containment building wall removed.

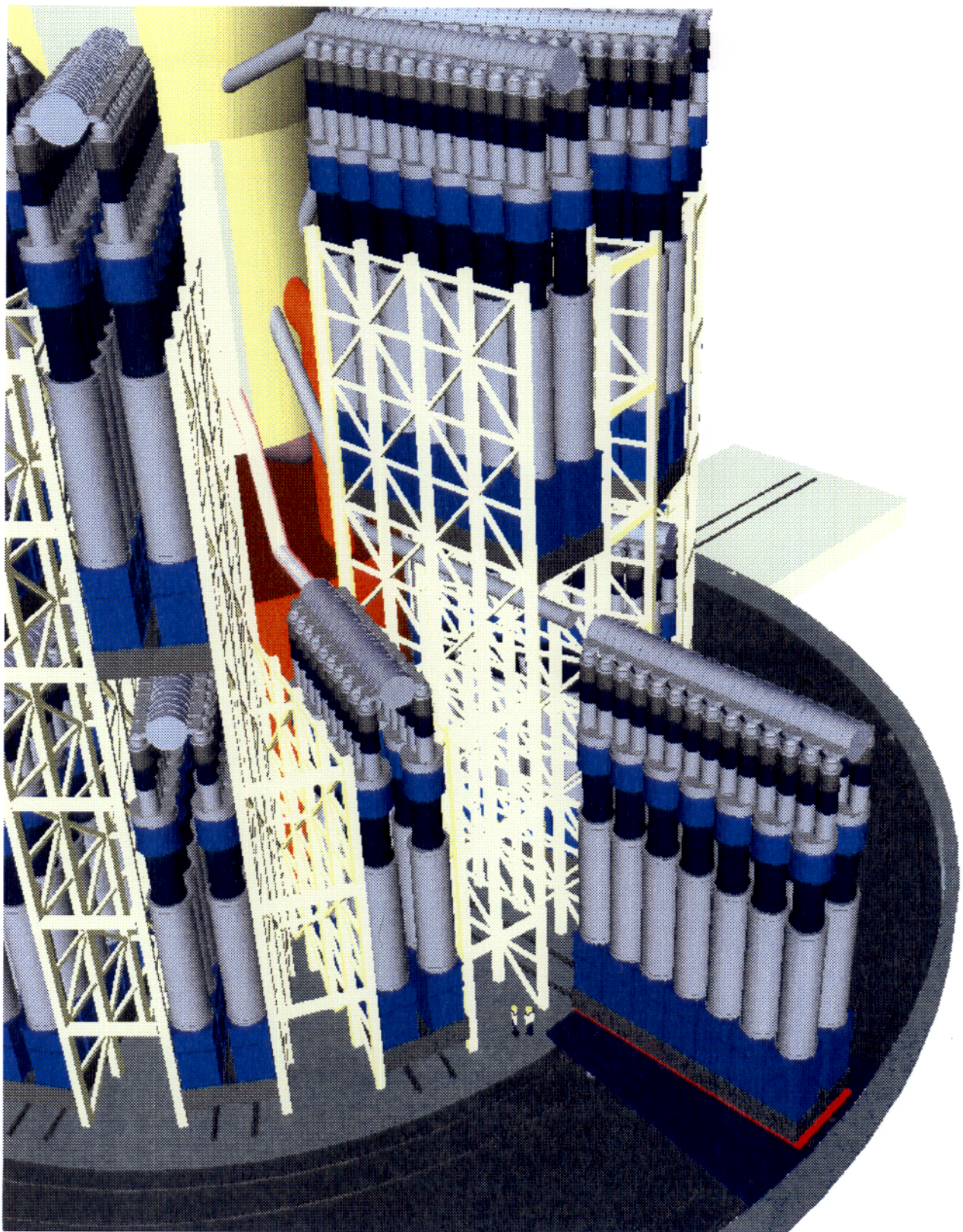


Figure 18.4. View showing a driver module being transported to a hot cell.

19. Economics

A preliminary cost analysis has been performed on the LIBRA-LiTE reactor using the FUSCOST code. The direct costs are calculated using up to date scaling algorithms and the costing is done in current dollars. An inflation rate consistent with the actual consumer price index is used to scale costs from those given in FUSCOST, which are given in 1986 dollars.

Figure 19.1 is a bar chart of the direct costs. The cost of the driver dominates the direct costs. The original driver cost algorithm as derived by PSI for LIBRA has been modified to reflect a reduction in metglas cost from \$15/kg to \$5/kg as reported by the manufacturers for lots greater than 1000 tonnes. This algorithm, escalated to 1991 is:

$$\text{Driver (1991 M\$)} = (271.2 + 3.414 \text{ CRR}) (\text{DET}/4)^{0.8}$$

where CRR is the chamber rep-rate and DET the driver energy on target. For a 6 MJ driver at 3.9 Hz, the cost is 480 M\$.

Table 19.1 gives the parameters used in the economic model and Table 19.2 gives a summary of the cost parameters for the reactor. In this case a 6 year construction period has been assumed at an interest rate of 8%, a target cost of 0.15\$/unit, a 44% power cycle efficiency and a 75% plant availability. Construction, home office and field office factors were taken as 10% each, and the owner's cost factor as 5%. In addition a 5% project contingency has been factored in as well as a 1% annual interim replacement cost. The cost of electricity (COE) is 42.6 mills/kWh, of which 29.7 mills/kWh is contributed by the interest on capital. The operation and maintenance contributes 10.8 and the fuel cost 2.1 mills/kWh respectively. Figure 19.2 shows the variation in the COE with both interest rate on capital and target cost. At 8% interest and 0.05\$/target the COE is 40.5 mills/kWh while on the other extreme, a 12% interest rate and a target cost of 0.3\$/unit, the COE is 56 mills/kWh.

This preliminary analysis shows that light ion beam inertial confinement fusion is very competitive with other fusion systems both inertial and magnetic.

Table 19.1. Parameters Used in Economic Model

Plant availability (%)	75
Years of accelerated tax depreciation	10
General inflation rate (%)	4
Cost escalation rate, average (%)	4
Construction time in years	6
Plant life in years	30
Construction factor (%)	10
Home office factor (%)	10
Field office factor (%)	10
Owner's cost factor (%)	5
Fraction of capital borrowed (%)	100
Interest rate on capital borrowed (%)	8-12
Investment tax credit rate (%)	8
Property tax rate (%)	2
Levelized interim replacement cost fraction (%)	1

Table 19.2. Summary of Costs for the Case at 8% Interest Rate and 15¢ Targets
\$M(1991)

Total direct capital costs	1669
Total indirect capital costs	697
Total overnight costs	2366
Time related costs	285
Total capital costs	2651
Annualized fuel costs	14
Annualized O&M costs	71
Annualized cost of capital	195
Total annualized costs	280

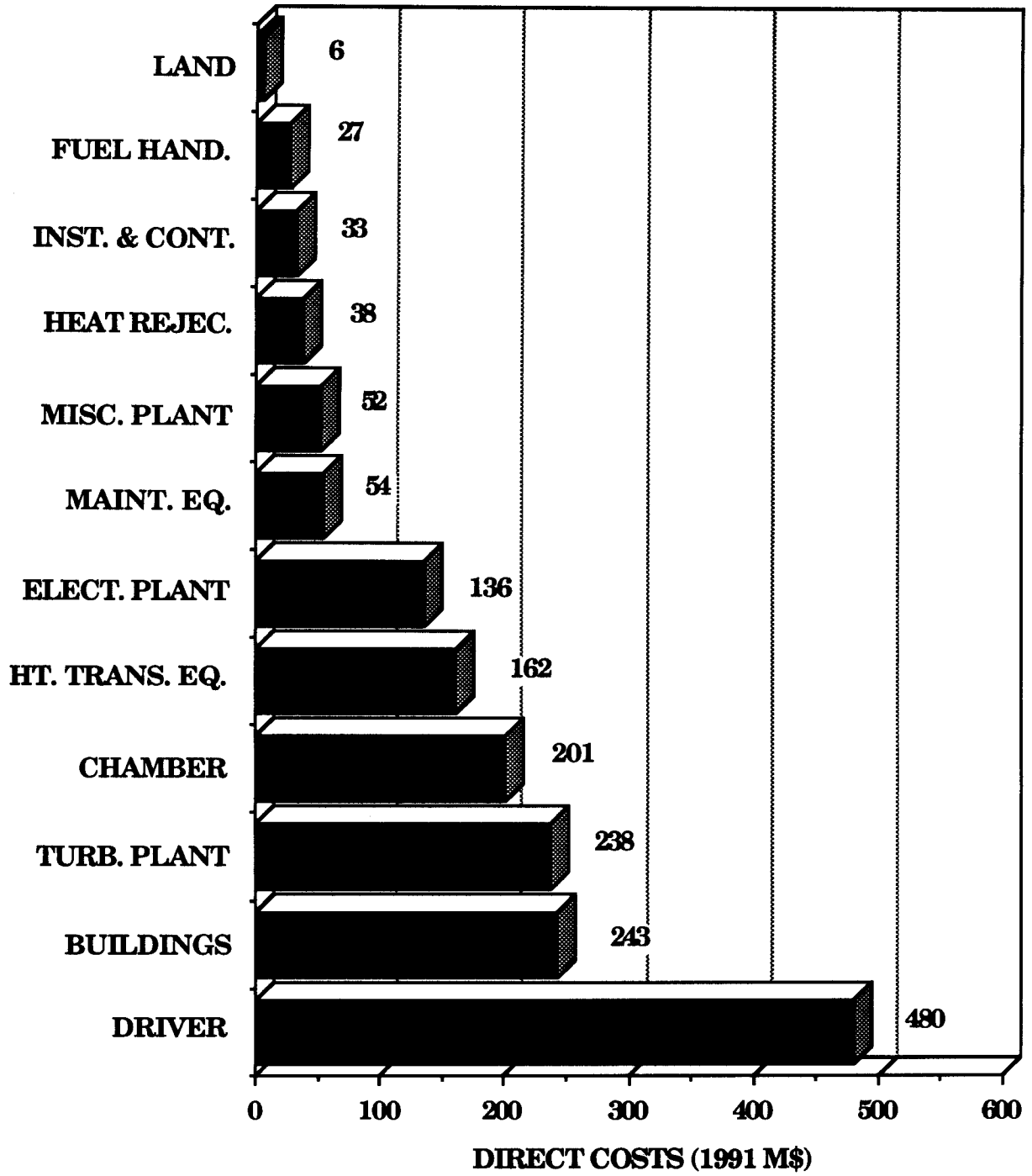


Figure 19.1. Bar chart of LIBRA-LiTE direct costs.

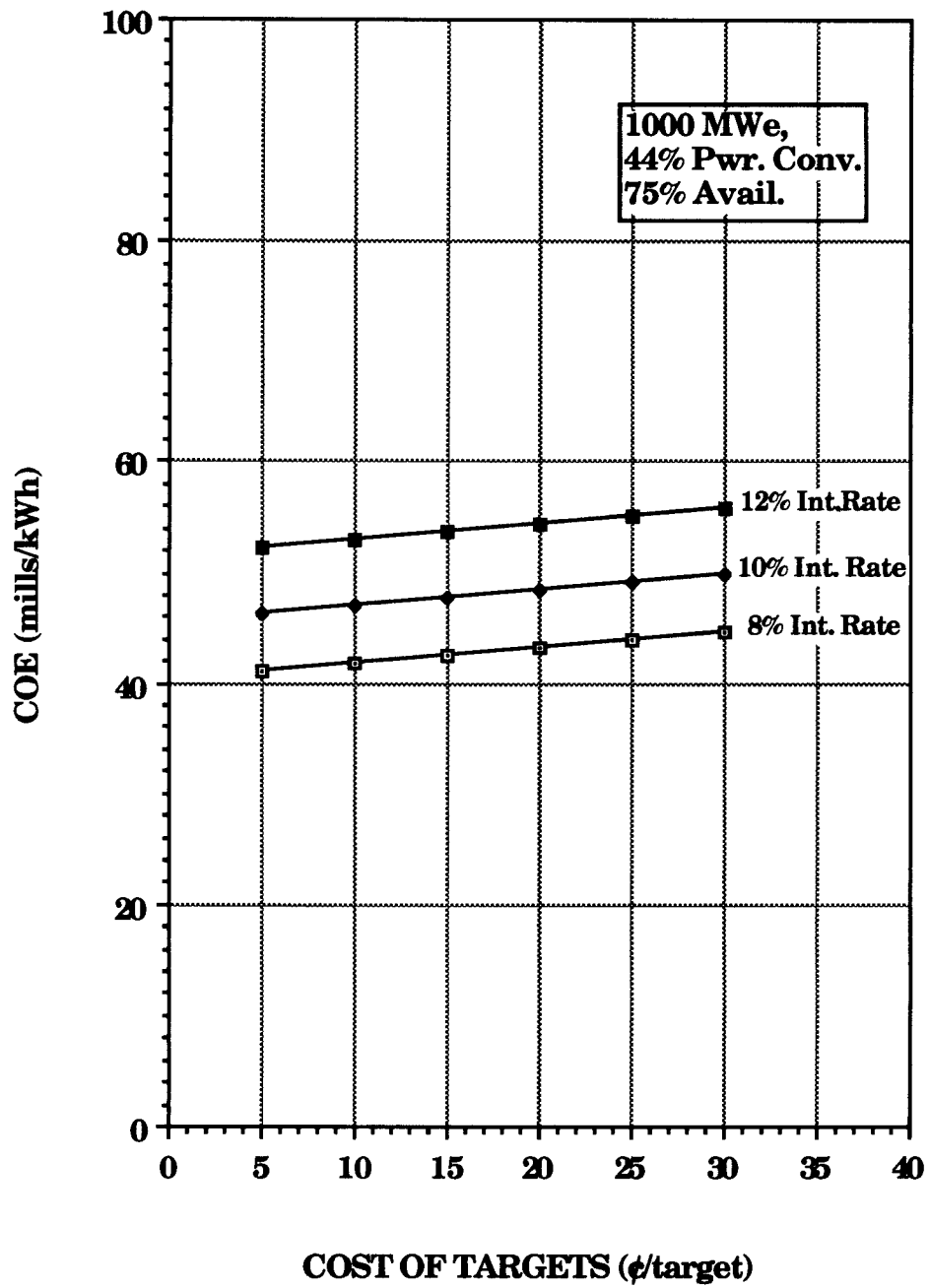


Figure 19.2. Cost of electricity as a function of interest rate and target costs.

20. Conclusions

The main conclusions from this phase of the work on the LIBRA-LiTE reactor are listed below.

1. The use of ballistically focused, 30 MeV Li ions will require a final focusing magnet close (within 1-2 meters) to the target.
2. The required microdivergence of the Li diodes must be ≈ 4 mrad or less in order to design a credible final focusing magnet.
3. The use of ballistic focusing rules out the use of Pb or PbLi alloys for a coolant/breeder combination. Lithium is a reasonable liquid metal to use for this transport concept.
4. It is possible to design magnets that use liquid Li as a current carrying element and as a coolant/breeder material. These magnets have a reasonable chance to operate in an extremely high radiation field.
5. The high damage rate in the final focusing magnet case will limit even a ferritic steel to ≈ 1 calendar year lifetime before replacement is recommended.
6. INPORT units made from woven HT-9 steel appear to be a feasible and attractive method to mitigate the effects of the blast wave, contain the Li coolant/breeder combination, and resist the high neutron wall loading for at least 3 FPY's.
7. The use of ballistic focusing requires that more attention be paid to maintenance procedures and this philosophy has played an important role in LIBRA-LiTE. The reactor is designed for rapid and frequent replacement of the inner magnets and the INPORT units.
8. The direct capital cost of the LIBRA-LiTE reactor is (in 1991\$) \$1669/kWe and the levelized cost of electricity is 43 mills/kWh. This makes the light ion beam approach very competitive with electricity costs from current tokamak projections of 70-80 mills per kWh.

21. Recommendations

The present work on LIBRA-LiTE has narrowed the design choices to a small, but critical set. In addition, the conceptual design is on a much firmer footing than it was in December 1990. However, there are a few areas which need more attention in the future. These areas are listed below.

1. A concerted effort on the theoretical and practical limits to the microdivergence of Li ion sources should be emphasized. This parameter has perhaps the largest leverage on the success or failure of the ballistic transport mode and on the performance of the reactor.
2. The concept of hot, liquid metal magnets needs to be investigated more thoroughly. Specifically, the performance of insulating layers in a high radiation field needs to be examined as well as the effect of periodic pressure pulses (≈ 4 Hz) on the microstructure of steel subjected to a high rate of He production and displacement damage.
3. An in-depth analysis of the design basis accident involving liquid Li should be performed. The desirability of Li has gone through many positive and negative cycles over the past years, especially in magnetic confinement schemes. Its use is highly favored in a ballistically focused inertial confinement device as is evidenced in this study. Therefore, a reassessment of the worst possible accidents can be very beneficial to the entire fusion community at this time.
4. Now that the major components are in place, a more detailed economics analysis can be performed. This would be especially beneficial now as there are several current tokamak studies being published and in the next year, there will be at least 2 new laser studies and 2 new heavy ion beam reactor designs released.

Appendix

Chronology of LIBRA-Related Reports and Videos, 1982–Present

1. "The INPORT Concept - An Improved Method to Protect ICF Reactor First Walls", G.L. Kulcinski, G.A. Moses, J. Sapp, M. Sawan, I.N. Sviatoslavsky, D.K. Sze, and W.F. Vogelsang, *J. Nucl. Matls.* 103 & 104, (1981) 103–108 [also UWFDM-426].
2. FPA-82-4. "Preliminary Considerations of Light Ion Beam Fusion and LIBRA Reactor Design," Presentation at KfK-Karlsruhe, FRG, 3-4 June 1982.
3. FPA-82-5. "Progress on Modelling of $Pb_{83}Li_{17}$ Recondensation on INPORT Units," L. Pong, D.K. Sze, R.R. Peterson, G.A. Moses, August 1982.
4. FPA-82-7. "Annual Report of Research Performed on the LIBRA Project Between 1 January and 31 December 1982 by Fusion Power Associates for the Kernforschungszentrum Karlsruhe GmbH, Karlsruhe, FRG," B. Badger, J. Billen, D. Bruggink, R. Engelstad, G.L. Kulcinski, E.G. Lovell, G.A. Moses, K. O'Brien, R.R. Peterson, L. Pong, I.N. Sviatoslavsky, D.K. Sze, W.F. Vogelsang, J. Watrous, 31 December 1982.
5. FPA-83-2. "An Effective Penetration Shield Design for ICF Reactors," M.E. Sawan, W.F. Vogelsang, and D.K. Sze, May 1983.
6. FPA-83-3. "Progress Report for the LIBRA Light Ion Beam Fusion Reactor Project for the Period January - June 1983," B. Badger, T. Bartel, J. Billen, M.L. Corradini, R.L. Engelstad, G.L. Kulcinski, E.G. Lovell, G.A. Moses, K.J. O'Brien, R.R. Peterson, L. Pong, M.E. Sawan, I.N. Sviatoslavsky, W.F. Vogelsang, J.J. Watrous, July 1983.
7. "Mechanical Analysis of First Wall Tubes for the LIBRA Conceptual Reactor," R. Engelstad and E. Lovell, Proceedings, 10th Symposium on Fusion Engineering, 5–9 December 1983, Philadelphia PA, IEEE Cat. No. 83CH1916-6NPS, C.C. Hopkins et al., editors, pp. 216–219 [also UWFDM-561].
8. FPA-83-8. "Annual Report for the LIBRA Light Ion Beam Fusion Reactor Project for the Period January - December 1983," B. Badger, T. Bartel, J. Billen, M.L. Corradini, R. Engelstad, D. Henderson, G.L. Kulcinski, G.A. Moses, K. O'Brien, R.R. Peterson, L. Pong, M.E. Sawan, I.N. Sviatoslavsky, D.K. Sze, W.F. Vogelsang, J.J. Watrous, December 1983.
9. FPA-84-1. "Progress Report for the LIBRA Light Ion Beam Fusion Reactor Project for the Period January-June 1984," B. Badger, T.J. Bartel, M.L. Corradini, R.L. Engelstad, D.L. Henderson, G.L. Kulcinski, E.G. Lovell, G.A. Moses, K.J. O'Brien, R.R. Peterson, L. Pong, M.E. Sawan, I.N. Sviatoslavsky, W.F. Vogelsang, and J.J. Watrous, July 1984.
10. FPA-84-2. "Basic Theory for Three-Dimensional Motion of LIBRA INPORT Tubes," R.L. Engelstad and E.G. Lovell, October 1984.
11. FPA-84-3. "Planar Vibrations of LIBRA INPORT Tubes Including Gravity Gradient Effects," R.L. Engelstad and E.G. Lovell, October 1984.
12. FPA-84-5. "ION - A Code to Compute Ion Trajectories in Z-Pinch Plasma Channels," G.A. Moses, November 1984.

13. FPA-84-8. "Annual Progress Report for the LIBRA Light Ion Beam Fusion Reactor Project for the Period January-December 1984," B. Badger, T.J. Bartel, M.L. Corradini, R.L. Engelstad, D.L. Henderson, G.L. Kulcinski, E.G. Lovell, G.A. Moses, K.J. O'Brien, R.R. Peterson, L. Pong, M.E. Sawan, I.N. Sviatoslavsky, W.F. Vogelsang, and J.J. Watrous, December 1984.
14. Vibration Analysis of LIBRA INPORTs; R.L. Engelstad and E.G. Lovell, *Fusion Technology*, 8 (July 1985) 1884-1889 [also UWFD-617 and FPA-85-2].
15. "Vapor Condensation in the Presence of a Noncondensable Gas," Lichung Pong and Gregory A. Moses, *Phys. Fluids* 29 (6) (June 1986) 1796-1804 [also UWFD-565].
16. FPA-88-1. "Progress Report on Work Performed on the LIBRA Design During the Period 1 February 1987 to 31 January 1988," B. Badger, G.L. Kulcinski, G. Moses, E. Lovell, R. Engelstad, J. MacFarlane, Z. Musicki, R. Peterson, M. Sawan, I. Sviatoslavsky, and L. Wittenberg, January 1988.
17. Chamber Design for the LIBRA Light Ion Beam Fusion Reactor, M.E. Sawan, I.N. Sviatoslavsky, L.J. Wittenberg, E.G. Lovell, R.L. Engelstad; *Fusion Technology* V.15, N.2, Part 2A (1989) 766-771 [also UWFD-778].
18. Overview of the LIBRA Light Ion Beam Fusion Conceptual Design, G.A. Moses, G.L. Kulcinski, D. Bruggink, R.L. Engelstad, E.G. Lovell, J.J. MacFarlane, Z. Musicki, R.R. Peterson, M.E. Sawan, I.N. Sviatoslavsky, L.J. Wittenberg, G. Kessler, U. von Möllendorff, E. Stein, D. Cook, R. Olson, I. Smith, P. Corcoran, H. Nishimoto, J. Fockler; *Fusion Technology* V.15, N.2, Part 2A (1989) 756-765 [also UWFD-781 and FPA-88-5].
19. Plasma Channels for the Propagation of Ion Beams in LIBRA, R.R. Peterson, G.A. Moses; *Beams'88, Conference Proceedings, 7th Intl. Conf. on High-Power Particle Beams*, W. Bauer and W. Schmidt, editors, 1988, Kernforschungszentrum Karlsruhe, pp. 625-630 [also UWFD-786 and FPA-88-4].
20. LIBRA-A Light Ion Beam Fusion Reactor Conceptual Design; G.A. Moses, G.L. Kulcinski, D. Bruggink, R. Engelstad, E. Lovell, J. MacFarlane, Z. Musicki, R. Peterson, M. Sawan, I. Sviatoslavsky, L. Wittenberg, G. Kessler, U. von Möllendorff, E. Stein, I. Smith, P. Corcoran, H. Nishimoto, J. Fockler, D. Cook, R. Olson; *Beams'88, Conference Proceedings, 7th Intl. Conf. on High-Power Particle Beams*, W. Bauer and W. Schmidt, editors, 1988, Kernforschungszentrum Karlsruhe, pp. 113-126 [also UWFD-787 and FPA-88-3].
21. UWFD-800. LIBRA - A Light Ion Beam Fusion Conceptual Reactor Design, B. Badger, G.A. Moses, R.L. Engelstad, G.L. Kulcinski, E. Lovell, J. MacFarlane, R.R. Peterson, M.E. Sawan, I.N. Sviatoslavsky, L.J. Wittenberg, I. Smith, R. Altes, P. Corcoran, R. Kuening, D. Pellow, D. Wake, J. Ehrhardt, G. Kessler, E. Stein, D.L. Cook, R.E. Olson, R.W. Stinnett; July 1989 (revised February 1990).
22. Activation Analysis for the LIBRA Light Ion Beam Fusion Conceptual Design, Mohamed E. Sawan; *Proceedings, 13th Symposium on Fusion Engineering*, 2-6 October 1989, Knoxville TN, IEEE Catalog No. 89CH2820-9 (1990) 1393-1396 [also UWFD-804].
23. Plasma Channels for the LIBRA Reactor Design; O. Yasar, G.A. Moses and R.R. Peterson, *Fusion Technology* V. 19, No. 3, Part 2A (1991) 669-772 [also UWFD-841].
24. FPA-90-3. "Annual Review of LIBRA-LiTE Project: Research Performed During Calendar Year 1990," D. Bruggink, R.L. Engelstad, G.L. Kulcinski, E.G. Lovell, J.J. MacFarlane, E.A. Mogahed, G.A. Moses, R.R. Peterson, M.E. Sawan, G. Sviatoslavsky, I.N. Sviatoslavsky, L.J. Wittenberg, December 1990.

25. FPA-91-2. "LIBRA-LiTE: A 1000 MWe Reactor," G.L. Kulcinski; June 1991 [presented at Fusion Power Associates Annual Meeting, Princeton NJ, 25-26 June 1991; to be published in J. Fusion Energy (also UWFD-857)].
26. FPA-91-3. "LIBRA-LiTE, A Light Ion Inertial Confinement Fusion Reactor With Ballistic Ion Propagation," R.R. Peterson, R.L. Engelstad, G.L. Kulcinski, E.G. Lovell, J.J. MacFarlane, E.A. Mogahed, G.A. Moses, S. Rutledge, M.E. Sawan, I.N. Sviatoslavsky, G. Sviatoslavsky, L.J. Wittenberg, September 1991 [Presented at the 14th IEEE/NPSS Symposium on Fusion Engineering, 30 September - 3 October 1991, San Diego CA (also UWFD-864)].
27. FPA-91-4. "LIBRA-LiTE: A Commercial Light Ion Fusion Power Plant - Final Report for Calendar Year 1991," B. Badger, B. Choi, R.L. Engelstad, G.L. Kulcinski, E.G. Lovell, J.J. MacFarlane, E.A. Mogahed, G.A. Moses, R.R. Peterson, S. Rutledge, M.E. Sawan, G. Sviatoslavsky, I.N. Sviatoslavsky, L.J. Wittenberg, December 1991 [also UWFD-880].

Videos

1. "LIBRA-LiTE, A Commercial Light Ion Fusion Power Plant," December 1990.
2. "LIBRA-LiTE (Mod 1), A Commercial Light Ion Fusion Power Plant," May 1991.
3. "LIBRA-LiTE (Mod 2), A Commercial Light Ion Fusion Power Plant," December 1991.